Modeling of condensed-matter systems by the tight-binding method : from nanostructures to complex liquids

2003

KŌGA, Junichiro

Contents

1 Introductory remarks 9
- 1.1 General overview 9
- 1.2 Purpose of the present thesis 12
- 1.3 Organization 14

2 The tight-binding method and the molecular dynamics method 17
- 2.1 Introduction for this chapter 17
- 2.2 The tight-binding method 18
  - 2.2.1 basic formulation 18
  - 2.2.2 approximations made in tight-binding 20
  - 2.2.3 solving the tight-binding problem 23
  - 2.2.4 calculation of optical properties 23
- 2.3 Brief introduction to molecular dynamics simulation 26
  - 2.3.1 basic formulation 26
  - 2.3.2 the "extended system" method 27
  - 2.3.3 properties calculated from molecular dynamics 28
- 2.4 Tight-binding molecular dynamics 32
  - 2.4.1 basic formulation 32
  - 2.4.2 formulation in the case of finite electron temperature 36
- 2.5 Conclusions for this chapter 38

3 Order-N tight-binding 39
- 3.1 Introduction for this chapter 39
- 3.2 Basic formulation of the Fermi-operator expansion method 41
  - 3.2.1 orthogonal tight-binding 41
  - 3.2.2 non-orthogonal tight-binding 43
- 3.3 Notes on the actual implementation 45
  - 3.3.1 electron temperature 45
  - 3.3.2 the expansion coefficients for the density matrix 46
  - 3.3.3 cutoff distances 48
- 3.4 Test molecular dynamics simulations 49
- 3.5 Conclusions for this chapter 50

4 Silicon nanostructure without point-group symmetry 53
- 4.1 Introduction for this chapter 53
- 4.2 Model and calculational scheme 56
- 4.3 Results 1 : the case of one dimension 60
  - 4.3.1 band structure 61

4.3.2 relation between band gap and size 62
4.3.3 relation between energy and the thermally-averaged radiative recombination time 63
4.3.4 calculation of ε_2 66
4.3.5 stokes shift 69
4.4 Results 2 : the case of zero and two dimension 70
4.4.1 band structures and band gaps 70
4.4.2 radiative recombination rate 72
4.5 Conclusions for this chapter 76

5 Silicon nanostructure with local disorders 79
5.1 Introduction for this chapter 79
5.2 Model and calculational method 81
5.3 Results and discussions 83
5.3.1 results for the ‘well-passivated’ model 83
5.3.2 results for the ‘poorly-passivated’ model 84
5.4 Conclusions for this chapter 90

6 Static and dynamical structure of liquid germanium at high density 93
6.1 Introduction for this chapter 93
6.2 Simulation method 95
6.2.1 non-orthogonal tight-binding scheme 95
6.2.2 simulational details 98
6.3 Results and discussions 101
6.3.1 static structure 101
6.3.2 dynamical structure 115
6.3.3 summary of results and discussions 120
6.4 Conclusions for this chapter 122

7 Amorphous germanium: glass transition and high-density structure 125
7.1 Introduction for this chapter 125
7.2 Conditions of the calculations 127
7.2.1 glass transition 127
7.2.2 low- and high-density amorphous Ge 128
7.3 Results 1 : glass transition 128
7.3.1 glass transition 128
7.3.2 static structure 130
7.3.3 dynamical structure 139
7.3.4 summary of results and discussions 141
7.4 Results 2 : high-density amorphous structure 143
7.4.1 static structure 143
7.4.2 dynamical structure 151
7.4.3 summary of results and discussions 156
7.5 Conclusions for this chapter 159

8 Concluding remarks 161
8.1 Summary of our work 161
8.2 Work left to be performed 164

Abstract

The present thesis focuses on the development and applications of the tight-binding (TB) and TB molecular dynamics (MD) methods. In particular, emphasis is put upon applications to real systems. We improve the transferability of tight-binding models, and further implement order-N tight-binding. We use these methods to analyze the properties of nanostructures, complex liquids, and associated amorphous solids.

In chapter 1, we give a general introduction for the present thesis. We study various methods and approximations used to simulate condensed-matter systems by computers, and describe the role of TB methods. Then, we give an overview of the entire thesis.

Chapters 2 and 3 are devoted to the description of TB methods and TBMD methods. In chapter 2, we discuss on the basic formulation of the TB methods, along with a brief review of MD simulations. Then, we describe the way in which we extend TB methods to MD simulations. In chapter 3, we focus on order-N tight-binding. When applied in a straightforward manner, calculational costs of TB methods scale as order-N^3. We show that, by introducing suitable approximations, it is possible to improve the scaling behavior to order-N. We investigate such order-N algorithms for TB methods. In particular, the case of non-orthogonal TB (NTB) and applications to MD simulations are taken into account. Several new techniques are introduced to improve the speed, memory requirement, and stability of the method. We perform realistic test MD simulations for germanium (Ge) by the obtained order-N method. The results obtained show, for the first time, that order-N NTB is in fact applicable to MD simulations.

In chapters 4 and 5, we focus on the study of photoluminescence properties of silicon (Si) nanostructures. Silicon nanostructures, unlike bulk Si, are known to show efficient photoluminescence at room temperature. We introduce new structural models for Si nanostructures, and study their electronic states and optical properties. In chapter 4, the first of our new model, "Si nanostructure devoid of point-group symmetry", is analyzed by the TB method. The results show that this model well accounts for the discrepancy found between theoretical calculations and experiments in the behavior of the radiative recombination time. In chapter 5, we introduce another new model, where structural relaxation of "poorly-passivated" Si nanostructures are taken into account. The effects of structural relaxation for "well-passivated" Si nanostructures have been studied in the past, while those for the "poorly-passivated" Si nanostructures are investigated for the first time in the present work. From our analyses based on the TB method, we find that the behavior of the so-called 'F'-band luminescence is well described by this model. In short, we successfully obtain a unified view on the mechanism of 'S' and 'F' band luminescence by introducing new structural models for Si nanostructures.

We further study the static and dynamical structures of liquid (ℓ-) and amorphous (a-) Ge in chapters 6 and 7. In particular, we thoroughly study properties at high density. In chapter 6, we construct a new, transferable NTBMD scheme for Ge, and apply the method to the study of ℓ-Ge. We perform TBMD simulations at low to high density, and calculate static and dynamical structures at each density. The obtained results are in excellent agreement with available experimental data. From our analyses, we clearly observe that, with density increase, random configurations characteristic of liquids increase compared to configurations originating from covalent bonds, while the remaining covalent bonds become close to those of the β-Tin structure. In chapter 7, TBMD simulations on a-Ge are performed. We use the order-N, NTBMD scheme constructed in the present work. Firstly, we perform glass-transition simulation of Ge. We start from a liquid well above melting point, and quench it to an amorphous solid. The static and dynamical structures of the liquid, super-cooled liquid, and amorphous Ge are extensively studied. We conclude that the large structural change which occurs during the glass transition is addressed to the increase of the covalent bonds. We further increase the density of a-Ge obtained in order to study the structural change of a-Ge with density increase. At each density simulated, we carefully analyze the static and dynamical structure of a-Ge. Our results show that the local structure of a-Ge transforms from tetrahedral at low-density to β-Tin-like at high density. We also find that, at intermediate density, both low-density and high-density amorphous structures coexist. From our work, a comprehensive knowledge concerning liquid and amorphous Ge at low to high density is obtained for the first time.

Finally, we conclude the present thesis in chapter 8. We summarize the achievements obtained in our work, and discuss their consequences. We also comment on work left to be performed in future studies.

Chapter 1

Introductory remarks

1.1 General overview

The development of theoretical and computational methods at the atomic scale has been an important part in the study of condensed-matter systems (CMS) for quite a long time. These methods allow us to predict new phenomena, and bring new insight into our knowledge of the world. Moreover, they provide us tools to be used in the industry area, for example, material design is nowadays aided by computational methods.

The elementary building blocks of CMS (the nuclei and the electrons) and the theory to which they obey (quantum mechanics) are all well known, so in principle, it is possible to calculate any property of any given system to the desired accuracy. Unfortunately, this is not possible in practice; as Dirac pointed out in 1929 [1], "The underlying physical laws necessary for the mathematical theory of a large part of physics and the whole of chemistry are thus completely known, and the difficulty is only that the exact application of these laws leads to equations much too complicated to be solved." This statement is true even in today's world, in which state-of-the-art computers allow us to perform vastly complicated calculations compared to Dirac's age.

The difficulty of the problem is in the complexity of the quantum-many-body problem. Any attempt to solve this problem in a straight-forward manner is doomed to fail. Consequently, inclusion of adequate approximations is essential in order to perform practical calculations.

The so-called Born-Oppenheimer approximation [2] is widely used in electronic-structure calculations. Since the nuclei are much heavier than electrons, the electrons respond instantaneously to the motion of the nuclei. For this reason, it is possible to treat the nuclei adiabatically, which leads to a separation of electronic and nuclear coordinates in the many-body wave function. This approximation allows us to reduce the problem to solving the equations for the electrons in some “frozen” configuration of the nuclei.

The Born-Oppenheimer approximation greatly simplifies the situation, but nonetheless, the problem still remains too complicated to be tackled as it is. Another difficulty is in the strong electron-electron interaction within the system. The exact treatment of the electron-electron interaction is possible, for example, by the quantum Monte-Carlo method, but practical applicability to CMS is still rather limited.

Another approximation widely used is the one-electron approximation, where a single electron moving in an effective potential is taken into account. Electron-electron interactions are included in the calculation in some effective way. By adopting this approximation, the problem finally becomes tractable. There are, however, still many approximations and assumptions made in practical applications. In Fig. 1.1, we show the table shown in ref. 3, in which various computational methods of treating CMS at the atomic level are compared. The overall tendency of Fig. 1.1 is that, the more close to exact the method is, the higher the computational burden.

The method frequently used by physicist is the method based on density-functional theory (DFT) [2, 4, 5]. This method is based on the principle that the total energy of a system is, in principle, exactly expressible in terms of the density for the electrons. Using this principle, it is possible to replace the many-electron problem by an equivalent set of self-consistent one-electron equations, or the so-called Kohn-Sham equations [5]. The method based on DFT is an *ab initio* method in the sense that no empirical parameters of any kind are not necessary for its execution.

Calculations based on DFT give excellent results for almost all materials of interest. However, the computational burden of the method is quite high, which severely limits the applicability of the method for large N, where N is the number of atoms within the system under consideration.

Another method used widely is the semi-empirical tight-binding (TB) method [6], which will be the main topic of the present thesis. In this method, the Hamiltonian matrix elements

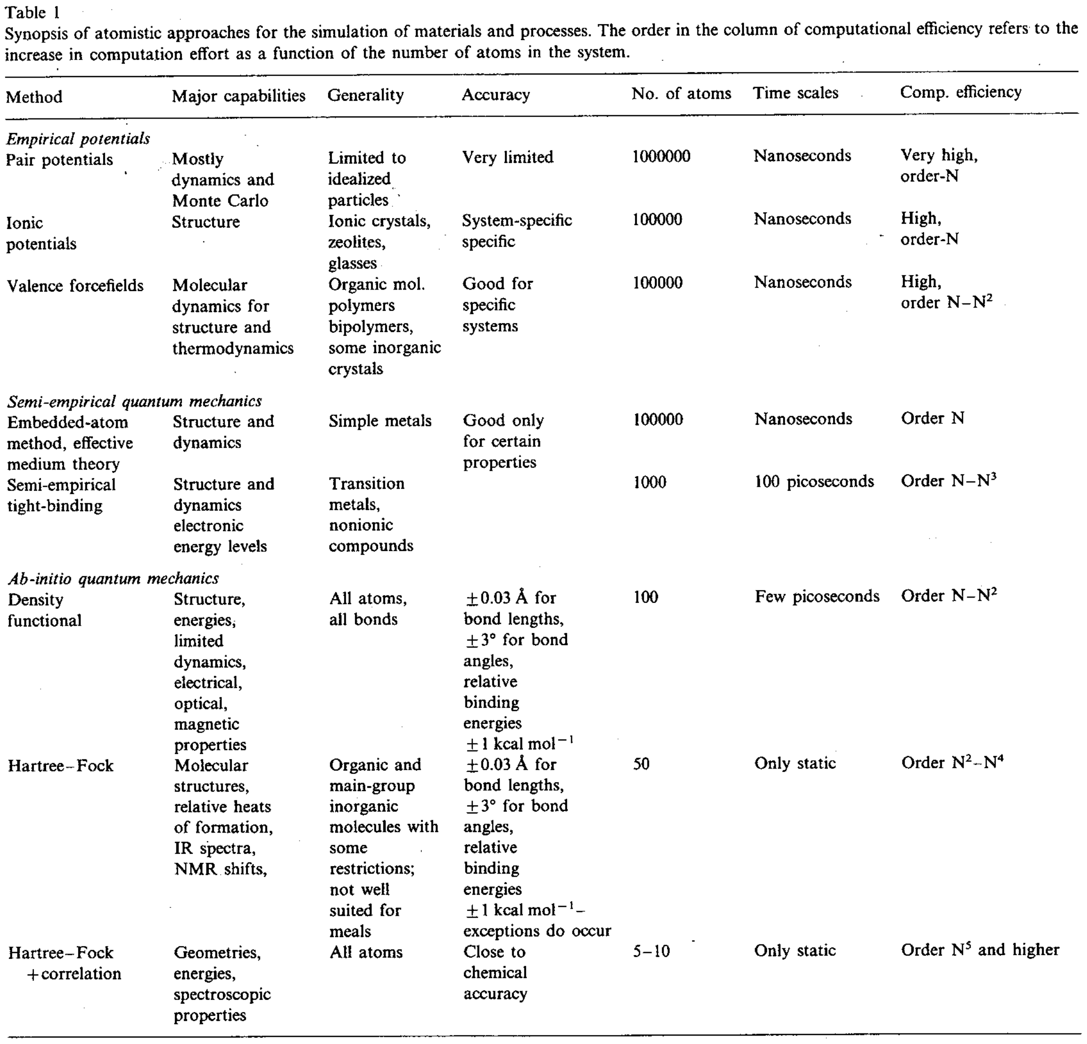

Table 1

Synopsis of atomistic approaches for the simulation of materials and processes. The order in the column of computational efficiency refers to the increase in computation effort as a function of the number of atoms in the system.

Method	Major capabilities	Generality	Accuracy	No. of atoms	Time scales	Comp. efficiency
Empirical potentials						
Pair potentials	Mostly dynamics and Monte Carlo	Limited to idealized particles	Very limited	1000000	Nanoseconds	Very high, order-N
Ionic potentials	Structure	Ionic crystals, zeolites, glasses	System-specific specific	100000	Nanoseconds	High, order-N
Valence forcefields	Molecular dynamics for structure and thermodynamics	Organic mol. polymers bipolymers, some inorganic crystals	Good for specific systems	100000	Nanoseconds	High, order N–N^2
Semi-empirical quantum mechanics						
Embedded-atom method, effective medium theory	Structure and dynamics	Simple metals	Good only for certain properties	100000	Nanoseconds	Order N
Semi-empirical tight-binding	Structure and dynamics electronic energy levels	Transition metals, nonionic compounds		1000	100 picoseconds	Order N–N^3
Ab-initio quantum mechanics						
Density functional	Structure, energies, limited dynamics, electrical, optical, magnetic properties	All atoms, all bonds	±0.03 Å for bond lengths, ±3° for bond angles, relative binding energies ±1 kcal mol^{-1}	100	Few picoseconds	Order N–N^2
Hartree–Fock	Molecular structures, relative heats of formation, IR spectra, NMR shifts,	Organic and main-group inorganic molecules with some restrictions; not well suited for meals	±0.03 Å for bond lengths, ±3° for bond angles, relative binding energies ±1 kcal mol^{-1}– exceptions do occur	50	Only static	Order N^2–N^4
Hartree–Fock +correlation	Geometries, energies, spectroscopic properties	All atoms	Close to chemical accuracy	5–10	Only static	Order N^5 and higher

Figure 1.1: Comparison of methods for calculations of materials in the atomic scale, reproduced from ref. 3.

for the electronic system is expressed in terms of the relative coordinates for the atoms. The calculations are considerably faster than DFT (typically by about an order of two to three), and yet give good results for a wide variety of systems. Further, the simplicity of its formulation allows us to obtain clear insights into the physical and chemical nature of the system.

Now let us argue the problem of dealing with CMS by computational methods from a different point of view. An alternative way for computing properties of CMS in the atomic scale is to assume some classical potential of the atoms, for instance the Lennard-Jones potential, and treat them as classical particles [7]. In this case, the basic theory underlying the dynamics of the system is classical statistical mechanics. From this perspective, there are two major methods in the market, namely, the Monte-Carlo method and the molecular dynamics (MD) method. The former method aims to calculate the partition function of the system by stochastic methods; this method will not be further mentioned in the present thesis. On the other hand, the MD method is a simulational method in which we calculate the trajectory of the atoms by integrating the classical equation of motion derived from the potential given.

A great innovation was made in 1985, when Car and Parinello reported on an algorithm which efficiently merges the DFT and the MD method [8]. The innovation in their algorithm was two-folds: (1) the DFT method was efficiently integrated into the MD method, and (2) by adopting iterative algorithms for the diagonalization of the Kohn-Sham equations, the DFT calculations are now performed much more efficiently than conventional methods. In the new algorithm, the number of operations necessary scales as $O\left(N_{\mathrm{b}} N_{\mathrm{PW}} \log N_{\mathrm{PW}}\right)$ when a plane-wave basis set is used, where N_{b} is the number of occupied bands and N_{PW} is the number of plane waves, compared to $O\left(N_{\mathrm{PW}}^{3}\right)$ in the conventional matrix diagonalization algorithm. This is a great improvement; however, for large N, the computational cost scales as $O\left(N^{3}\right)$, and consequently, the method becomes extremely difficult to apply as N grows.

In the TB method, on the other hand, it is possible to reduce the calculational cost to $O\left(N\right)$ [9–11], and further, integration into MD methods is performed with ease [12]. The $O\left(N\right)$ scaling is achieved by using the fact that in TB methods, the basis set is localized atomic orbitals, and that the density matrix decays exponentially in insulators and semiconductors, and also for finite-temperature metals [13, 14]. These properties of the TB method makes the method particularly suited for systems which require relatively large N, *e.g.*, nanostructures and non-crystalline systems.

1.2 Purpose of the present thesis

The TB method is a very efficient method for the quantitative calculation of the electronic structure in CMS. Moreover, it gives surprisingly good results in many cases. However, the applicability of the TB method to certain fields of physics and chemistry is not always clear. Further, applications of $O\left(N\right)$ TB have so far been limited. From these considerations, the following questions arise:

1. The TB methods give good description of valence bands, but in general, the conduction bands are not as well-described [15]. How good is the TB method for the study of optical processes, in which transitions from valence to conduction bands, or vice versa, must be taken into account?

2. Transferability of TB methods to various situations is not always obvious. Is it possible to apply the TB method to situations where the environment of the atoms greatly changes?

3. Order-N implementation for TB methods have so far been limited mostly to TB models with limitations, *i.e.*, TB models based on orthogonal basis sets, nearest-neighbor interactions, and large band gaps. How efficient is the $O(N)$ TB method for other, more complex TB models?

Keeping all of the above points in mind, it is the purpose of the present thesis to construct accurate, efficient TB methods and TBMD methods, and apply the scheme for the study of realistic systems. To this end, we carry out the following:

1. construct and/or implement various TB methods and TBMD methods.

2. implement $O(N)$ TB for the case of non-orthogonal and long-range TB model.

3. apply the obtained method to:

    (a) the study of optical properties in nanostructures, and

    (b) to the study of structural properties for covalently-bonded liquids and amorphous solids at various density.

Now let us closely examine the topics listed above. The TB and TBMD methods are constructed so that they are transferable and/or give good description of the band structure in the crystal phase. Moreover, we extend $O(N)$ TBMD for non-orthogonal and relatively long-range TB models. For the calculation of nanostructures, it is necessary to explicitly take into account all the atoms within the system. This leads to systems containing a maximum of some 1000-2000 atoms, which are not accessible by *ab initio* methods. Another point is in that since we work with optical properties, a good description of not only the valence but also the conduction band is of critical importance. For MD simulation of covalently bonded liquids and amorphous solids, quantum-mechanical treatment of the forces is indispensable. We also note that the bonding nature for these systems changes as density changes. In order to simulate such a situation, a transferable TB scheme is needed. In short, the topics we deal with not only have interests of their own, but also give answers to the aforementioned questions we addressed.

1.3 Organization

The present thesis will be organized as follows.

In chapters 2 and 3, formulations for the TB and TBMD methods are given. The TB methods have been widely used since the epoch-making paper by Slater and Koster in 1954 [16]. The essence of this paper is that the Hamiltonian matrix elements can be parameterized by the position vector of two atoms under consideration, provided that the so-called "two-center approximation" is adopted. The parameterized Hamiltonian are calculated from a small number of independent integrals and formula related to the relative position of the two atoms. This leads to significant simplifications for the electronic-structure calculations. The importance of this paper may perhaps be best described by the "anecdotal evidence" introduced in the review by Goringe, Bowler, and Hernández [6]: "in the shelves of the Radcliffe Science Library, Oxford, volume 94 of *Physical Review* stands out from its shelf for its broken spine, and falls open at table 1 on page 1503".

Chapter 2 is devoted to the description of the basic concepts for the TB and TBMD methods. We will not attempt to give the full account of all the work performed in this field, but will focus on the concepts and techniques used in the rest of the thesis. Then in chapter 3, we describe $O(N)$ TB. We concentrate on the method called the "Fermi-operator expansion method". In particular, we discuss the case of non-orthogonal TB, in which the non-orthogonality of the atomic orbitals is explicitly taken into account, and MD methods based on it. We comment on the techniques introduced in this work, and further perform test

MD simulations to show that the scheme really works.

We present in chapters 4 and 5 the study on the photoluminescence properties of silicon (Si) nanostructures. Since bulk Si has an indirect band structure with band gap of $\sim 1.1\,\mathrm{eV}$ in the infrared region, the luminescence efficiency of bulk Si is very low, and even if it showed luminescence, it will be invisible. However, in 1990, efficient, room temperature, and visible photoluminescence from porous [17] and nanocrystalline [18] Si was observed. This phenomenon is important from a technological point of view, in that it shows a passage to Si-based optoelectronic devices, and further from a fundamental point of view, in that the low dimension of the system is the crucial aspect of the luminescence. The impact of the phenomenon is best seen in the number of publications for porous Si, the most well-studied system for light-emitting Si, shown in Fig. 1.2 (the figure is from ref. 19). We observe from

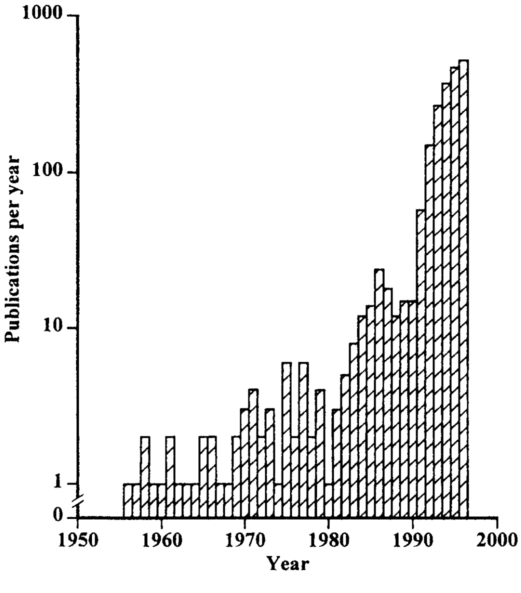

Figure 1.2: Publications per year for porous Si, plotted against year. Note that the vertical axis is logarithmic. Reproduced from ref. 19.

Fig. 1.2 that the number of publications has increased explosively after the discovery of the luminescence phenomena.

In chapter 4, we give results for the new model we introduce, which we refer to as "Si nanostructure without point-group symmetry". Our model shows different behavior from conventional model nanostructures. In chapter 5, we introduce another new model, in which the local symmetry of Si nanostructures, *e.g.*, bond length and bond angles, are not present.

From analyses of this model, we find that this model well accounts for the so-called 'F'-band luminescence from porous Si [20].

We further study the static and dynamical structures of liquid (ℓ-) germanium (Ge) and amorphous (a-) Ge at various density. The problem of the structural properties of covalently-bonded liquids and amorphous solids has been studied for quite a long time [21]. The behavior they show at different density, however, are not fully elucidated as of now. The difficulty of simulating such systems is in that the bonding nature of the system changes as the density is changed. We tackle this problem by the TBMD method.

We construct transferable, non-orthogonal TB scheme for Ge, and apply the scheme for the study of ℓ-Ge at different density in chapter 6. We thoroughly examine the static and dynamical structures of the system, and deduce the structural change of ℓ-Ge with density increase. We further study glass transition of Ge and high-density structure of a-Ge in chapter 7. Glass transition is simulated by rapid quenching of ℓ-Ge well above melting temperature. We then compress a-Ge thus obtained, and deduce the structural changes of a-Ge with density increase.

Finally, we conclude the present thesis in chapter 8. We give a summary of the achievements obtained in our work, and further comment on work left to be performed in future studies.

Chapter 2

The tight-binding method and the molecular dynamics method

2.1 Introduction for this chapter

In the present thesis, we use the tight-binding (TB) method and the TB molecular dynamics (MD) method to study various physical properties of nanostructures, liquids, and associated amorphous solids. The present chapter is devoted to a description of these methods.

Tight-binding methods have been used widely to study the electronic properties of condensed-matter systems, ever since the epoch-making work by Slater and Koster [16]. Tight-binding calculations are much faster than *ab initio* methods (typically by about two to three orders of magnitude), and yet possess sufficient accuracy to be practical in realistic quantum mechanical calculations. For this reason, the methods have been used extensively to study various systems, including covalently bonded systems, metallic systems, and even ionic systems in crystalline, liquid, and amorphous solid forms [6].

Tight-binding molecular dynamics simulation (MD) was first performed by Wang, Chan, and Ho [12]. In their work, a very simple total energy calculation scheme based on the TB method was presented. It was formulated in such a way that the calculations be performed more or less systematically. The stability of the crystal structure of silicon (the diamond structure) was investigated, which gave good results. Note that the diamond structure cannot be stabilized by classical potentials, unless an artificial three-body term is included so that atoms with tetrahedral bonding have the lowest energy. Since then, TBMD simulations have been performed extensively for a wide variety of materials [22].

The advantages of the TB method are rather obvious; to list some of them,

1. it is the fastest *quantitative* electronic structure calculation method. In particular, it is possible to reduce the calculational cost from $O\left(N^3\right)$ to $O\left(N\right)$ by adopting suitable approximations.

2. the simplicity of its formulation gives clear physical and chemical picture of the system, for example, the local density of states is clearly and easily calculated and interpreted.

3. it can be formulated in both real and reciprocal space, so that artificial periodic boundary conditions need not be introduced, for example, in the calculation of nanostructures.

The present and succeeding chapter is devoted to the description of the TB and the TBMD method. In the present chapter, general overview of the methods will be given, while in the succeeding chapter, we focus on order-N TB method, in which the problem is solved by order-N operations (whereas in standard methods, order-N^3 operations are needed). We will not discuss on the detailed account of the vast amount of work put forward in this field; rather, we will focus on the aspects which are of importance in the rest of the present thesis.

The rest of the chapter is organized as follows. In section 2.2, we formulate the TB method. We describe the basic formulation, and approximations made. We also discuss on the calculation of optical properties within the framework of the TB method. Section 2.3 is a brief review of MD methods. We focus only on the aspects used in the present study. Then, in section 2.4, we give descriptions on TBMD. Finally, we conclude this chapter in section 2.5.

2.2 The tight-binding method

2.2.1 basic formulation

We first describe the basic formulation of the TB method. The TB method is based on the assumption that, near an atom nuclei, the wave functions of valence electrons are expressible in terms of the wave functions of isolated atoms. In other words, the basis set for the electronic-structure calculation is the atomic orbitals.

Let us begin with the one-electron Hamiltonian of an isolated atom,

$$H_a = -\frac{\hbar^2}{2m}\Delta + v_a(\boldsymbol{r}) \tag{2.1}$$

where $\hbar$ is the Planck constant divided by 2π, m is the mass of an electron, and $v_a(\boldsymbol{r})$ is the potential for the electron at position $\boldsymbol{r}$. Consequently, the Shrödinger equation of the isolated atom is written as

$$H_a\psi_\nu(\boldsymbol{r}) = \varepsilon_\nu^{\text{isolated}}\psi_\nu(\boldsymbol{r}), \tag{2.2}$$

where $\psi_\nu(\boldsymbol{r})$ and $\varepsilon_\nu^{\text{isolated}}$ are the eigenfunction and eigenvalue of the isolated atoms, respectively, and ν denotes angular momentum. Note that in general, the functions $\psi_\nu(\boldsymbol{r})$'s are non-orthogonal, *i.e.*, $\int \psi_\nu^*(\boldsymbol{r}-\boldsymbol{r}_i)\,\psi_{\nu'}(\boldsymbol{r}-\boldsymbol{r}_{i'})\,d^3r \neq \delta_{\nu\nu'}\delta_{ii'}$.

We now take into account the case of crystals. Note that the method is equally applicable to other condensed-matter systems, such as liquids and amorphous solids. The Hamiltonian is written as

$$\begin{aligned} H_{\mathrm{c}} &= -\frac{\hbar^2}{2m}\Delta + v(\boldsymbol{r}), \text{ where} \\ v(\boldsymbol{r}) &= \sum_{i\boldsymbol{R}} v_a(\boldsymbol{r}-\boldsymbol{d}_i-\boldsymbol{R}). \end{aligned} \tag{2.3}$$

Here, $\boldsymbol{d}_i$ denotes position vector for atom i within the unit cell, and $\boldsymbol{R}$ represents the cellvectors of the unit cell. The eigenstates for eq. (2.3) are expressed in terms of the Bloch sum,

$$\Psi_{n\boldsymbol{k}}(\boldsymbol{r}) = \frac{1}{\sqrt{N}}\sum_{\boldsymbol{R},i}\sum_{\nu} a_{i\nu,n\boldsymbol{k}}\mathrm{e}^{\mathrm{i}\boldsymbol{k}\cdot(\boldsymbol{d}_i+\boldsymbol{R})}\psi_\nu(\boldsymbol{r}-\boldsymbol{d}_i-\boldsymbol{R}). \tag{2.4}$$

Note that the Bloch sum is not an essential aspect of the method; it is possible to formulate the problem completely in real space. This is particularly useful in nanostructures, in which reciprocal space cannot be defined unless an artificial periodic boundary condition is introduced. In this case, the Shrödinger equation for the crystal is expressed as

$$H_{\mathrm{c}}\Psi_{n\boldsymbol{k}}(\boldsymbol{r}) = \varepsilon_{n\boldsymbol{k}}\Psi_{n\boldsymbol{k}}(\boldsymbol{r}). \tag{2.5}$$

Now we multiply $\mathrm{e}^{-\mathrm{i}\boldsymbol{k}\cdot(\boldsymbol{d}_i+\boldsymbol{R})}\psi_\nu^*(\boldsymbol{r}-\boldsymbol{R}-\boldsymbol{d}_i)$ to eq. (2.5) from the left and integrate it, which results in the following generalized eigenvalue problem,

$$H^{\boldsymbol{k}}_{i\nu,i'\nu'}a_{i'\nu',n\boldsymbol{k}} = \varepsilon_{n\boldsymbol{k}}S^{\boldsymbol{k}}_{i\nu,i'\nu'}a_{i'\nu',n\boldsymbol{k}}. \tag{2.6}$$

Here, the matrices $H^{\boldsymbol{k}}_{i\nu,i'\nu'}$ and $S^{\boldsymbol{k}}_{i\nu,i'\nu'}$, hereafter referred to as the Hamiltonian matrix and the overlap matrix, respectively, are defined by the following equations,

$$H^{\boldsymbol{k}}_{i\nu,i'\nu'} = \sum_{\boldsymbol{R}'} \mathrm{e}^{\mathrm{i}\boldsymbol{k}\cdot(\boldsymbol{R}'+\boldsymbol{d}_{i'}-\boldsymbol{d}_i)} \int \psi^*_\nu\left(\boldsymbol{r}-\boldsymbol{d}_i\right) H_\mathrm{c}\psi_{\nu'}\left(\boldsymbol{r}-\boldsymbol{R}'-\boldsymbol{d}_{i'}\right) d^3r, \text{ and} \tag{2.7}$$

$$S^{\boldsymbol{k}}_{i\nu,i'\nu'} = \sum_{\boldsymbol{R}'} \mathrm{e}^{\mathrm{i}\boldsymbol{k}\cdot(\boldsymbol{R}'+\boldsymbol{d}_{i'}-\boldsymbol{d}_i)} \int \psi^*_\nu\left(\boldsymbol{r}-\boldsymbol{d}_i\right) \psi_{\nu'}\left(\boldsymbol{r}-\boldsymbol{R}'-\boldsymbol{d}_{i'}\right) d^3r, \tag{2.8}$$

where we have used the periodicity of the unit cell to truncate one summation for the cellvector. By diagonalizing eq. (2.6), we obtain the one-electron eigenvalues ε_n and the corresponding eigenfunctions (to be exact, the expansion coefficients of the eigenfunctions). The tight-binding and overlap matrices are empirically fitted so as to reproduce results obtained from *ab initio* calculations or experiments, for example, the band structure of some crystal structure.

In many cases, the overlap matrix is assumed as an unit matrix. Since all known atomic orbitals are non-orthogonal, this assumption is not always valid. The justification for this assumption is that it is always possible to create an orthogonal basis set from a non-orthogonal one, in such a way as to preserve the symmetry properties of the original set [23]. This transformation is referred to as the "Löwdin transformation", and is executed as follows,

$$\psi_{i\nu} = \sum_{i'\nu'} S^{-\frac{1}{2}}_{i\nu,i'\nu'}\phi_{i'\nu'}. \tag{2.9}$$

In this case, $\psi_{i\nu}$ is used to construct the Bloch sum of eq. (2.4), while the "real" atomic orbital is $\phi_{i'\nu'}$. However, this justification only applies for the system which is fitted. Once the system is changed to a different one, a new Löwdin transformation is needed. For this reason, it is preferable that we work in the non-orthogonal picture in the first place. In chapters 6 and 7, we construct transferable non-orthogonal TB schemes for germanium (Ge), and study low- and high-density forms of liquid and amorphous Ge.

2.2.2 approximations made in tight-binding

two-center approximation

The tight-binding integral, eq. (2.7), has three centers, namely, the position of the wave function on the left, the positions of the Hamiltonian itself, and the position of the wave function on the right. Therefore, eq. (2.7) is a three-center integral. By assuming that this integral is a two-center integral, the fitting procedure and applications to molecular dynamics simulations become drastically easier. In this case, eq. (2.7) is expressed as

$$H^{\boldsymbol{k}}_{i\nu,i'\nu'} = \sum_{\boldsymbol{R}'} \mathrm{e}^{\mathrm{i}\boldsymbol{k}\cdot(\boldsymbol{R}'+\boldsymbol{d}_{i'}-\boldsymbol{d}_i)} \int \psi^*_\nu\left(\boldsymbol{r}-\boldsymbol{d}_i\right) H'_{\mathrm{c}}\psi_{\nu'}\left(\boldsymbol{r}-\boldsymbol{R}'-\boldsymbol{d}_{i'}\right) d^3r, \tag{2.10}$$

where H'_{c} is a reduced Hamiltonian which only includes terms corresponding to either atoms placed at the center of the left wave function or at the center of the right wave function. The integral in eq. (2.10) is non-zero only when the two atomic wave functions have the same symmetry, which significantly reduces the number of independent integrals. For example, there are only ten independent tight-binding integrals for systems with s, p, and d orbitals, which are shown in Fig. 2.1.

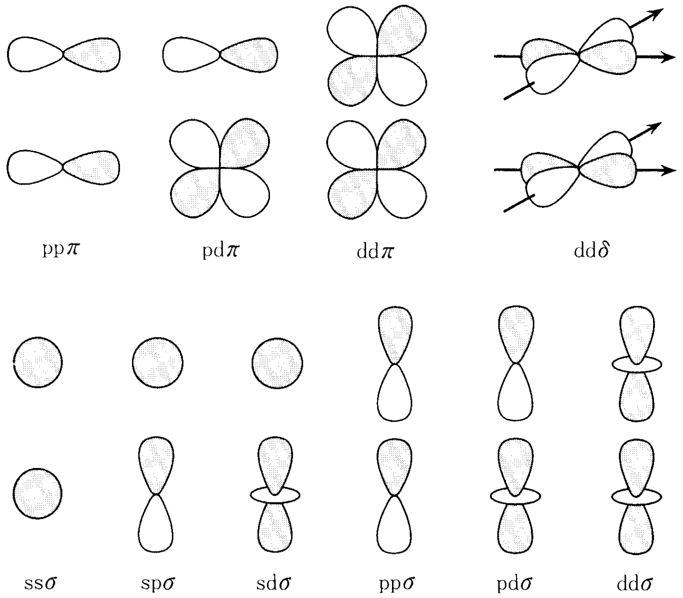

Figure 2.1: The ten independent integrals for s, p, and d orbitals. Reproduced from ref. 24.

Concerning the atomic orbitals, rather than using the spherical harmonic functions themselves, it is more convenient to use a real function constructed from a linear combination of spherical harmonic functions. For example, in the case of p orbitals, we use the functions

$$\begin{aligned} \phi_x(\boldsymbol{r}) &= f_1(r)\tfrac{1}{\sqrt{2}}\left[-Y_{1,1}\left(\hat{\boldsymbol{r}}\right)+Y_{1,-1}\left(\hat{\boldsymbol{r}}\right)\right] = \sqrt{\tfrac{3}{4\pi}}f_1(r)\tfrac{x}{r} \\ \phi_y(\boldsymbol{r}) &= f_1(r)\tfrac{\mathrm{i}}{\sqrt{2}}\left[Y_{1,1}\left(\hat{\boldsymbol{r}}\right)+Y_{1,-1}\left(\hat{\boldsymbol{r}}\right)\right] = \sqrt{\tfrac{3}{4\pi}}f_1(r)\tfrac{y}{r} \\ \phi_z(\boldsymbol{r}) &= f_1(r)Y_{1,0}\left(\hat{\boldsymbol{r}}\right) = \sqrt{\tfrac{3}{4\pi}}f_1(r)\tfrac{z}{r}. \end{aligned} \tag{2.11}$$

Now the interaction between orbitals centered at different atoms is calculated as shown in Fig. 2.2. All the formula necessary for the evaluation of the interaction between s, p, and d

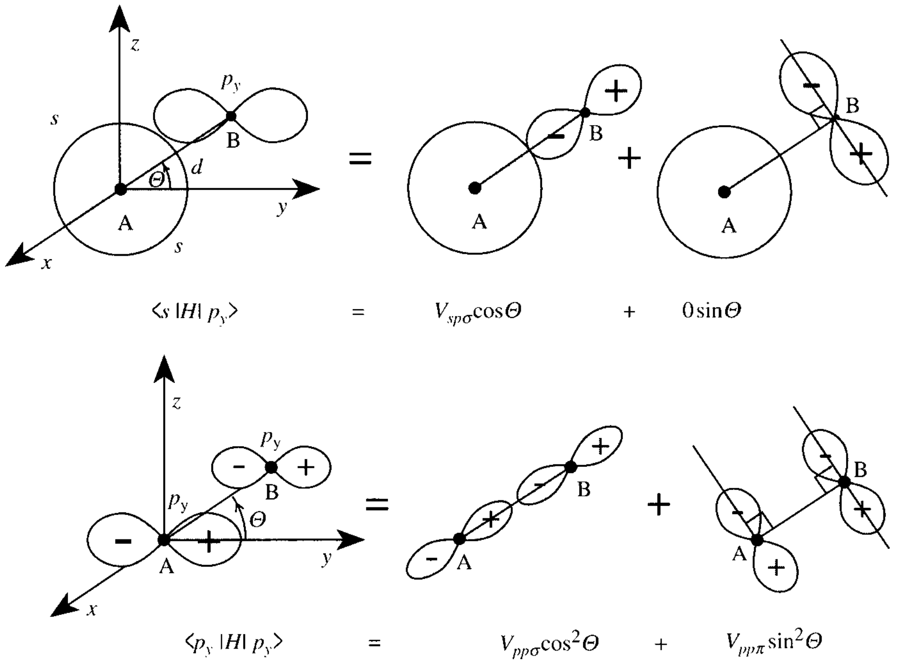

Figure 2.2: Calculation of the matrix elements between s and p orbitals. Reproduced from ref. 25

orbitals are given in table 1 of ref. 16.

The two-center approximation greatly simplifies calculations, and further gives surprisingly accurate results in many cases. However, inclusion of three-center terms gives better representation of the system, so it is preferable in certain cases that these terms are taken into account. In chapters 4 and 5, we use the orthogonal, sp^3, three-center tight-binding scheme constructed in ref. 26. This TB model reproduces the conduction band of bulk Si, and therefore, is suited for calculation of optical properties.

crystal-field terms

When the two orbitals in the integral of eq. (2.10) are located at the same atom, we obtain the following expression,

$$\begin{aligned} H^{\boldsymbol{k}}_{i\nu,i\nu'} &= \int \psi^*_\nu(\boldsymbol{r}) H_a \psi_{\nu'}(\boldsymbol{r})\, d^3r + \sum_{i'\boldsymbol{R}} \int \psi^*_\nu(\boldsymbol{r})\, v_a(\boldsymbol{r} - \boldsymbol{d}_{i'} - \boldsymbol{R}')\, \psi_{\nu'}(\boldsymbol{r})\, d^3r \\ &= \varepsilon_{\nu,\nu'}\delta_{\nu,\nu'} + \Delta\varepsilon_{\nu,\nu'}. \end{aligned} \tag{2.12}$$

The first term of eq. (2.12) is the usual one-electron energy for the isolated atom. The second term is the so-called "crystal-field term", and physically corresponds to contribution from atomic potential surrounding the atom under consideration. In short, the crystal-field term means that, strictly speaking, the on-site term is not diagonal. This term is not explicitly taken into account in most tight-binding calculations, since it gives little effects for systems which TB methods work well.

2.2.3 solving the tight-binding problem

Here, we briefly comment on the method of solving the TB problem. The evaluation of the eigenvalues and eigenstates for the TB problem is achieved by diagonalizing eq. (2.6). This is performed by standard methods in the case of orthogonal TB [27]; first, the Hamiltonian is transformed into tridiagonal form by the Householder transformation, and then the eigenvalues and eigenvectors of the tridiagonal matrix are obtained by iterative procedures. In the case of non-orthogonal TB, we deal with the overlap matrix by performing a Cholesky decomposition,

$$\boldsymbol{S} = \boldsymbol{L}\boldsymbol{L}^{T}. \tag{2.13}$$

We multiply $\boldsymbol{L}^{-1}$ to eq. (2.6) from the left, and redefine the wave function as $\Psi'_n = \boldsymbol{L}^{T}\Psi_n$ to obtain the following symmetric, standard eigenvalue problem,

$$\boldsymbol{L}^{-1}\boldsymbol{H}\left(\boldsymbol{L}^{T}\right)^{-1}\Psi'_n = \varepsilon_n\Psi'_n. \tag{2.14}$$

Finally, we obtain the wave function from a reverse transformation, $\Psi_n = \left(\boldsymbol{L}^{T}\right)^{-1}\Psi'_n$.

The procedures described here are standard ways of solving the TB problem. In both cases, diagonalization of a matrix is necessary, which means that calculational costs scale as $O\left(N^3\right)$, while memory requirements scale as $O\left(N^2\right)$. These facts lead to severe limitations when large systems are taken into account, even in TB methods which are two to three orders of magnitude faster than *ab initio* methods. It is, however, possible to reduce the scaling behavior for both the calculational costs and memory requirements to $O\left(N\right)$ by adopting suitable approximations. This topic of the $O\left(N\right)$ TB will be treated in the succeeding chapter.

2.2.4 calculation of optical properties

In chapters 4 and 5, we deal with the optical properties of Si nanostructures. Here, we describe the method of calculating such properties within the framework of the TB method.

We first calculate the inter-band oscillator strength, defined by the following equation [15]:

$$f_{\mathrm{c,v}} = \frac{2}{m(\varepsilon_{\mathrm{c}} - \varepsilon_{\mathrm{v}})} \left|\langle \Psi_{\mathrm{c}} \left| \mathbf{e}\cdot\boldsymbol{p} \right| \Psi_{\mathrm{v}} \rangle\right|^2 , \tag{2.15}$$

where Ψ_{c} and Ψ_{v} are the one-electron wave functions for conduction band c and valence band v, respectively, $\boldsymbol{p}$ is the momentum operator, $\mathbf{e}$ is the polarization vector of light, m is the mass of an electron, and ε_{c} and ε_{v} are the eigenvalues corresponding to conduction band c and valence band v, respectively. We have suppressed the index for the wave vector, as we only take into account the case of the Γ-point. The oscillator strength is averaged for the three directions of $\boldsymbol{p}$. By writing $|\Psi_b\rangle = \sum_{i\nu} a^b_{i\nu} |i\nu\rangle$, where i is the site index and ν is the angular momentum, the matrix element in eq. (2.15) is rewritten as

$$\langle \psi_{\mathrm{c}} | \mathbf{e}\cdot\boldsymbol{p} | \psi_{\mathrm{v}} \rangle = \sum_{i\nu,j\mu} a^{\mathrm{c}*}_{i\nu} a^{\mathrm{v}}_{j\mu} \langle i\nu | \mathbf{e}\cdot\boldsymbol{p} | j\mu \rangle \tag{2.16}$$

The oscillator strength is a dimensionless quantity, which expresses the strength of a transition between conduction band c and valence band v [15].

Once the oscillator strength is calculated, optical properties are derived from it. For example, the radiative recombination time of a transition from conduction band c to valence band v is calculated by the following equation [28]:

$$\tau_{\mathrm{c,v}} = \frac{m\hbar c^2}{2n_0 \alpha (\varepsilon_{\mathrm{c}} - \varepsilon_{\mathrm{v}})^2 f_{\mathrm{c,v}}}, \tag{2.17}$$

where n_0 is the refractive index. In chapters 4 and 5, we choose the value of $n_0 = 1.2$, the experimental value of porous Si [29]. Symbol α is the fine structure constant, c and $\hbar$ have their usual meanings, *i.e.*, the light velocity and the Planck constant divided by 2π, and all other symbols are the same as defined in the above. A similar quantity, the radiative recombination rate, is the inverse of $\tau_{\mathrm{c,v}}$, which will also be calculated.

Since the oscillator strength is scattered between bands, it is not informative to study $\tau_{\mathrm{c,v}}$ for each c, v pair. Instead, we calculate the thermal average of eq. (2.17) by the following equation:

$$\langle \tau \rangle = \frac{\sum \tau_{n,n'} \exp\left[-\frac{(\varepsilon_n - \varepsilon_{n'})}{k_\mathrm{B}T}\right]}{\sum \exp\left[-\frac{(\varepsilon_n - \varepsilon_{n'})}{k_\mathrm{B}T}\right]}. \tag{2.18}$$

Here, k_B is the Boltzmann constant, T is the temperature, n and n' represent conduction and valence bands, respectively, and the other symbols are the same as described in the above. Equation (2.18) is a good approximation if the carriers are in thermal equilibrium prior to recombination, which is the case for Si nanostructures [30].

The thermally-averaged radiative recombination time reflects the low-energy structure of the energy band, as evidently seen from eq. (2.18). This is appropriate for the study of luminescence, because in general, luminescence involves only transitions which are energetically near or at the band edge [31].

However, it is also important to understand the optical response for the full energy band. For this purpose, we calculate the imaginary part of the dielectric function by the following equation [15]:

$$\varepsilon_2(\hbar\omega) \propto \frac{1}{(\hbar\omega)} \sum_{\mathrm{c,v}} f_{\mathrm{c,v}} \delta\left[\varepsilon_\mathrm{c} - \varepsilon_\mathrm{v} - \hbar\omega\right], \tag{2.19}$$

where $\hbar\omega$ is the energy of the incident light, and all other symbols are the same as above. The imaginary part of the dielectric function ε_2 is calculated as a sum of the contribution from each band, and therefore is an appropriate function to study for the aforementioned purpose.

Now let us describe the method to calculate the matrix elements for the momentum operator, $\boldsymbol{p}$. This is not an easy task when working in the TB picture, since in TB, the actual form of the atomic wave functions is not known, but only the matrix elements of the Hamiltonian matrix are known. In order to calculate eq. (2.19) in such a situation, we use the scheme proposed in ref. 32. From eq. (2.16), the matrix element we calculate is expressed as $\langle i'\mu' \left|\boldsymbol{p}\right| i\mu\rangle$. By using the commutative relation of $\boldsymbol{p}$, namely,

$$\boldsymbol{p} = \frac{\mathrm{i}m}{\hbar}\left[\boldsymbol{r}, H\right], \tag{2.20}$$

and by inserting $\mathbf{1} = \sum_{l\lambda} |l\lambda\rangle\langle l\lambda|$, we obtain the following,

$$\sum_{l\lambda} \langle i'\mu'|\boldsymbol{r}|l\lambda\rangle\langle l\lambda|H|i\mu\rangle - \sum_{l\lambda} \langle i'\mu'|H|l\lambda\rangle\langle l\lambda|\boldsymbol{r}|i\mu\rangle. \tag{2.21}$$

The Hamiltonian matrix elements within eq. (2.21) are known. On the other hand, the matrix elements for the position operator, $\boldsymbol{r}$, is not easily derived. We first assume that matrix elements between different atoms are zero. Under this assumption, the matrix elements of $\boldsymbol{r}$ are written as

$$\langle i'\mu'|\boldsymbol{r}|i\mu\rangle = \left[\boldsymbol{d}_{\mu',\mu} + \boldsymbol{R}_{i',i}\delta_{\mu',\mu}\right]\delta_{i',i}. \tag{2.22}$$

The first term of the right-hand side of eq. (2.22) cannot be calculated unless we know the form of the atomic wave functions, and physically corresponds to contribution from isolated atoms. This term is known to be small in semiconductors [33], and will be ignored in the present work. The second term, on the other hand, arises only when there are interaction between atoms, and is simply the position vector of an atom. From all of the above, we finally obtain the following equation for the matrix elements of the momentum operator:

$$\langle i\mu|\boldsymbol{p}|j\nu\rangle = \frac{\mathrm{i}m}{\hbar}\langle i\mu|H|j\nu\rangle\boldsymbol{R}_{ij}, \tag{2.23}$$

where $\boldsymbol{R}_{ij}$ is $\boldsymbol{R}_i - \boldsymbol{R}_j$. We insert eq. (2.23) into eq. (2.16) in order to obtain the final quantity we wish to evaluate.

2.3 Brief introduction to molecular dynamics simulation

We now move on to the description of molecular dynamics (MD) simulation. We will not cover all the vast amount of work done in this field, nor shall we go into the technical details of the method; there are a number of good textbooks around, for example, ref. 7, suited for this purpose. Rather, we focus on the basics, and physical properties calculated in the present thesis.

2.3.1 basic formulation

In MD simulations, the atoms in the system are assumed to follow the rules of classical mechanics. We integrate the equation of motion for classical mechanics, and deduce properties of the system from the trajectory of the atoms thus obtained.

Let us start from the generalized coordinates, $\{\boldsymbol{q}_i\}$, and their conjugate momenta, $\{\boldsymbol{p}_i\}$. The Hamiltonian for the system (the reader is not to be confused with the quantum mechanical Hamiltonian of, for instance, eq. (2.3)) is expressed as

$$\mathcal{H}(\{\boldsymbol{p}_i\},\{\boldsymbol{q}_i\}) = \mathcal{K}(\{\boldsymbol{p}_i\}) + \mathcal{V}(\{\boldsymbol{q}_i\}), \tag{2.24}$$

where $\mathcal{K}(\boldsymbol{p}_i)$ is the kinetic energy of the system, defined as $\mathcal{K}(\{\boldsymbol{p}_i\}) = \sum_{i=1}^{N}\sum_{\alpha}\frac{p_{i\alpha}^2}{2m_i}$, the symbol α being the three Cartesian coordinates, and m_i being the mass of atom i. The term $\mathcal{V}(\{\boldsymbol{q}_i\})$ is the potential energy of the system. Hamilton's equations of motion are derived from eq. (2.24) by the standard way as [34]

$$\frac{d\boldsymbol{q}_i}{dt} = \frac{\partial\mathcal{H}(\{\boldsymbol{p}_i\},\{\boldsymbol{q}_i\})}{\partial\boldsymbol{p}_i} \rightarrow \frac{d\boldsymbol{q}_i}{dt} = \frac{\boldsymbol{p}_i}{m_i} \tag{2.25}$$

$$\frac{d\boldsymbol{p}_i}{dt} = -\frac{\partial\mathcal{H}(\{\boldsymbol{p}_i\},\{\boldsymbol{q}_i\})}{\partial\boldsymbol{q}_i} \rightarrow \frac{d\boldsymbol{p}_i}{dt} = -\frac{\partial\mathcal{V}(\{\boldsymbol{q}_i\})}{\partial\boldsymbol{q}_i} = \boldsymbol{f}_i, \tag{2.26}$$

where $\boldsymbol{f}_i$ is the force acting on atom i. Provided that the potential energy is known as a function of $\{\boldsymbol{q}_i\}$, it is possible to integrate eqs. (2.25) and (2.26). The integrations are performed by methods such as the Verlet method or the predictor-corrector method proposed by Gear. If the simulation is performed for long enough times, we obtain thermodynamically-meaningful results. Note that in this situation, the Hamiltonian, $\mathcal{H}(\{\boldsymbol{p}_i\},\{\boldsymbol{q}_i\})$, is a constant of the motion.

2.3.2 the "extended system" method

When MD simulations are applied as it is, the resultant trajectory of the atoms forms the so-called microcanonical ensemble in statistical mechanics, in which the number of atoms N, the volume of the system V, and Hamiltonian of the system are conserved. It is possible, however, to work in other ensembles. One way of generating different ensembles is to add "extended systems" to the original system [35]. As an example, we describe the constant-temperature method proposed by Nosé [35].

We first introduce "virtual" variables, which are scaled by factor s as

$$\begin{aligned} \boldsymbol{q}_i' &= \boldsymbol{q}_i \\ \boldsymbol{p}_i' &= \boldsymbol{p}_i/s \\ dt' &= dt/s, \end{aligned} \tag{2.27}$$

where we have denoted the "virtual" variables without a prime, and "real" variables with a prime. In this situation, we add an "extended system", corresponding to a "heat bath" attached to the system, to the Hamiltonian in the following manner,

$$\begin{aligned} \mathcal{H}_{\text{total}} &= \mathcal{H}\left(\{\boldsymbol{p}_i\},\{\boldsymbol{q}_i\}\right) + \mathcal{H}_{\text{Nosé}}\left(P_s, s\right), \text{ where} \\ \mathcal{H}\left(\{\boldsymbol{p}_i\},\{\boldsymbol{q}_i\}\right) &= \sum_i \frac{\boldsymbol{p}_i^2}{2m_i s^2} + \mathcal{V}\left(\{\boldsymbol{q}_i\}\right) \text{ and} \\ \mathcal{H}_{\text{Nosé}}\left(P_s, s\right) &= \frac{P_s^2}{2Q} + g k_{\text{B}} T \log s. \end{aligned} \tag{2.28}$$

Here, P_s is the conjugate momentum for s, Q is the "mass" of the heat bath, and g is the number of freedoms, which is $3N+1$ when we work with the virtual variables, while it is $3N$ when we work with real variables. Hamilton's equations of motion are derived from standard procedures from eq. (2.28). We obtain the following coupled differential equations,

$$\frac{d\boldsymbol{q}'_i}{dt'} = \frac{\boldsymbol{p}'_i}{m} \tag{2.29a}$$

$$\frac{d\boldsymbol{p}'_i}{dt'} = -\frac{\partial \mathcal{V}\left(\{\boldsymbol{q}_i\}\right)}{\partial \boldsymbol{q}'_i} - \frac{1}{s}\frac{ds}{dt'}\boldsymbol{p}'_i \tag{2.29b}$$

$$\frac{ds}{dt'} = \frac{P_s}{Q} s \tag{2.29c}$$

$$\frac{dP_s}{dt'} = \sum_i^N \sum_{\alpha=1}^3 \frac{\boldsymbol{p}'_i}{m_i} - 3Nk_{\text{B}}T. \tag{2.29d}$$

Note that eqs. (2.29a)-(2.29d) are expressed in terms of the "real" variables instead of the "virtual variables". It is possible to prove that the trajectory of the atoms derived from the above equations of motion form the so-called canonical ensemble, in which the number of atoms N, the volume of the system V, and the temperature T is conserved [36]. In the same manner, it is possible to obtain, for example, the isobaric-isoenthalpic ensemble, by adding an extra degree of freedom corresponding to a piston attached to the system [37].

2.3.3 properties calculated from molecular dynamics

In MD simulations, physical properties are evaluated as time averages. We present here the quantities calculated in the present thesis. Note that, since we only work with the atomic coordinates of the system, the generalized coordinate $\boldsymbol{q}_i$ will be hereafter referred to as simply $\boldsymbol{r}_i$.

thermodynamic quantities

1. temperature of the system, T

   The temperature T of the system is related to the kinetic energy $\mathcal{K}$ of the system, and is calculated by the following equation,

$$T = \frac{2}{3k_{\mathrm{B}}} \langle \mathcal{K} \rangle . \tag{2.30}$$

2. pressure of the system, P

   The pressure of the system is obtained from the virial theorem, and in practice, is evaluated as

$$P = \frac{Nk_{\mathrm{B}}T}{V} \left(1 - \frac{1}{3Nk_{\mathrm{B}}T} \left\langle \sum_{i=1}^{N} \sum_{j>i}^{N} r_{ij} \frac{d\mathcal{V}(r_{ij})}{dr_{ij}} \right\rangle \right), \tag{2.31}$$

   where $r_{ij} = |\boldsymbol{r}_i - \boldsymbol{r}_j|$.

static structure

1. two-body distribution function, $g(r)$

   The two-body distribution function is related to the two-body correlation function, $n^{(2)}(\boldsymbol{r}_1, \boldsymbol{r}_2)$. The two-body correlation function has the following property: the probability of finding two particles within a volume fraction d^3r and d^3r' is proportional to $n^{(2)}(\boldsymbol{r}_1, \boldsymbol{r}_2)\, d^3r d^3r'$. Provided that $n^{(2)}(\boldsymbol{r}_1, \boldsymbol{r}_2)$ is normalized as $\iint n^{(2)}(\boldsymbol{r}, \boldsymbol{r}')\, d^3r d^3r' = \frac{N!}{(N-2)!}$ (in which case $n^{(2)}(\boldsymbol{r}, \boldsymbol{r}')$ is formally expressed as $\sum_{\substack{i,i' \\ i \neq i'}} \delta(\boldsymbol{r} - \boldsymbol{r}_i)\, \delta(\boldsymbol{r}' - \boldsymbol{r}_{i'})$), $g(\boldsymbol{r}, \boldsymbol{r}')$ is defined as

$$g(\boldsymbol{r}, \boldsymbol{r}') = \frac{n^{(2)}(\boldsymbol{r}, \boldsymbol{r}')}{\rho^2}, \tag{2.32}$$

   where ρ is the average density of the system. In homogeneous and isotropic systems, *e.g.*, liquids, eq. (2.32) depends only on the distance between two atoms, $r = |\boldsymbol{r} - \boldsymbol{r}'|$, and $g(\boldsymbol{r}, \boldsymbol{r}')$ is simply written as $g(r)$. The two-body distribution function describes the probability of finding an atom with distance r apart from a reference atom, normalized by the average density. Since for infinite r, the probability is equal to the average density, $g(r)$ approaches 1 for large values of r. From $g(r)$, it is possible to calculate the number of atoms present within a distance r_c of some reference atom, or in other words, the coordination number N_c. This is performed by the following equation [21],

$$N_\mathrm{c} = \int_0^{r_\mathrm{c}} 4\pi r^2 \rho g\left(r\right) dr. \tag{2.33}$$

Note, however, that N_c is well-defined only for crystalline systems. In liquids and amorphous solids, the best we can do is to evaluate the average of N_c. Further, the usual procedure is to take r_c up to the first minimum of $g(r)$, but in some cases, this is not appropriate. The definition of N_c is not unique in non-crystalline systems; in the evaluation of N_c, an important point is to stay consistent throughout the discussion.

2. static structure factor, $S(Q)$

The static structure factor expresses the correlation of the density in reciprocal space. It is possible to calculate $S(Q)$ from either its definition, or by Fourier transforming $g(r)$. Concerning the former method, the definition of $S(Q)$ is given by

$$\begin{aligned} S(Q) &= \frac{1}{N}\langle \rho(Q)\rho(-Q)\rangle \\ \rho(Q) &= \sum_{j=1}^{N} \mathrm{e}^{-\mathrm{i}\boldsymbol{Q}\cdot\boldsymbol{r}_j}, \end{aligned} \tag{2.34}$$

where $\boldsymbol{r}_j$ is the position of the jth atom and N is the number of atoms. We note that, in calculating eq. (2.34), we average over all $\boldsymbol{Q}$ vectors of equal magnitude, and that, because of the finite size of the simulation cell, the $\boldsymbol{Q}$ vectors are restricted to $2\pi\left(\frac{n_x}{L_x}, \frac{n_y}{L_y}, \frac{n_z}{L_z}\right)$, where n_x, n_y, and n_z are integers and L_x, L_y, and L_z are the lengths of the simulation cell in the x, y, and z direction, respectively. On the other hand, concerning the latter method, it is possible to calculate $S(Q)$ from the Fourier transform of $g(r)$ in the following manner,

$$S\left(Q\right) = 1 + \int_0^{\infty} 4\pi r^2 \rho_0 \left[g(r) - 1\right] \frac{\sin\left(Qr\right)}{Qr} dr. \tag{2.35}$$

For simulation cell of infinite size, the two methods give identical results. However, since we must work in a finite-size cell, we adopt the former method in order to obtain $S(Q)$ accurately.

3. bond-angle distribution function, $g^{(3)}\left(r_{\mathrm{c}}, \theta\right)$

   The bond-angle distribution function gives the distribution of the angles formed by pairs of vectors drawn towards two neighboring atoms within a cutoff distance r_{c} from some reference atom. This property is related to the three-body correlation function, $n^{(3)}\left(\boldsymbol{r}_1, \boldsymbol{r}_2, \boldsymbol{r}_3\right)$, which has obvious correspondence with the two-body correlation function, $n^{(2)}\left(\boldsymbol{r}, \boldsymbol{r}'\right)$. We note that in many cases, it is convenient to normalize this function by $(\sin\theta)^{-1}$, since for a perfectly random bond-angle distribution, $g^{(3)}\left(r_{\mathrm{c}}, \theta\right)$ is proportional to $\sin\theta$.

dynamical structure

One of the great advantages of the MD method is that it allows us to study the dynamical structure of the system quantitatively. Here, we present the quantities we calculate in the present thesis for the dynamical structure.

1. mean-square displacement, $\left\langle R\left(t\right)^2\right\rangle$

   The mean-square displacement is defined by the equation,

$$\left\langle R\left(t\right)^2\right\rangle = \left\langle \left|\boldsymbol{r}\left(t+t_0\right) - \boldsymbol{r}\left(t_0\right)\right|^2\right\rangle . \tag{2.36}$$

   By studying this function, we are able to determine whether the system is diffusive or not. For diffusive systems, eq. (2.36) evolves linearly against time, while for non-diffusive systems, the function saturates at very short times, and does not increase from that time on.

2. velocity autocorrelation function, $\psi\left(t\right)$

   It is possible to calculate the autocorrelation of the velocity by the following equation,

$$\psi\left(t\right) = \frac{\left\langle \boldsymbol{v}\left(t+t_0\right) \cdot \boldsymbol{v}\left(t_0\right)\right\rangle}{\left\langle \boldsymbol{v}\left(t_0\right) \cdot \boldsymbol{v}\left(t_0\right)\right\rangle}. \tag{2.37}$$

   For short times, the velocities at different times are strongly correlated, and therefore, $\psi\left(t\right) \sim 1$. On the other hand, for sufficiently long times, the velocities lose their correlation with respect to the original velocities, meaning that $\left\langle \boldsymbol{v}\left(t+t_0\right) \cdot \boldsymbol{v}\left(t_0\right)\right\rangle \approx$

$\langle \boldsymbol{v}(t+t_0)\rangle \langle \boldsymbol{v}(t_0)\rangle \approx 0$. Note that the average of the velocity is always zero (corresponding to zero velocity for the center of gravity), since we determine the initial velocity so as to give zero for the average velocity, and further total velocity is a constant of motion.

3. diffusion coefficient, D

   The diffusion coefficient D is calculated either from $\left\langle R(t)^2 \right\rangle$ or $\psi(t)$.

   (a) From MSD, D is calculated by using the Einstein relation as

   $$D = \lim_{t\to\infty} \frac{1}{6(t-t_0)} \left\langle [\boldsymbol{r}(t) - \boldsymbol{r}(t_0)]^2 \right\rangle . \tag{2.38}$$

   (b) From VAF, D is calculated from the following equation,

   $$D = \frac{k_{\mathrm{B}}T}{m} \int_0^\infty \psi(t)\, dt \tag{2.39}$$

4. spectrum density, $\psi(\omega)$

   The spectrum density is a Fourier transform of the VAF, and is expressed as

   $$\psi(\omega) \propto \int_0^\infty \cos(\omega t)\, \psi(t)\, dt. \tag{2.40}$$

   The significance of $\psi(\omega)$ lies in that it reflects the vibrational modes in the system. By investigating this function, it is possible to deduce the magnitude of a certain vibrational mode in the system. Note that the mode at $\omega = 0$ corresponds to the diffusive mode, as is evidently shown from eq. (2.39).

2.4 Tight-binding molecular dynamics

2.4.1 basic formulation

In the present thesis, we perform MD simulations based on TB electronic state calculations. From the arguments of the preceding section, we need to evaluate the total Hamiltonian of the system, and forces consistent with it, from atomic positions in order to perform this task. Here, we describe on how to calculate such properties within the framework of the TB method.

The total Hamiltonian $\mathcal{H}$ of a system is written as [12,22]

$$\mathcal{H} = \mathcal{K} + E_{\text{binding}},$$
$$E_{\text{binding}}\left(\boldsymbol{r}_1, \cdots, \boldsymbol{r}_N\right) = E_{\text{BS}}\left(\boldsymbol{r}_1, \cdots, \boldsymbol{r}_N\right) + U_{\text{rep}}\left(\boldsymbol{r}_1, \cdots, \boldsymbol{r}_N\right). \tag{2.41}$$

Here, E_{binding} is the binding energy of the system, and E_{BS} is the so-called band-structure energy, defined as

$$E_{\text{BS}} = 2 \sum_{n}^{N_{\text{occ}}} \varepsilon_n, \tag{2.42}$$

where ε_n is the one-electron energy and N_{occ} is the number of occupied levels. The second term, U_{rep}, represents the sum of the ion-ion repulsion and corrections to the double counting of the electron-electron interaction in E_{BS}.

There are various methods proposed in order to calculate eq. (2.41) within the framework of the TB method [22]. Here, we describe a simple scheme, based on the method described by Wang, Chan, and Ho in ref. 12. This method will be used in chapters 4 and 5 to evaluate structural relaxation of Si nanostructures.

In the scheme of Wang, Chan, and Ho, the band structure energy is determined by the eigenvalue of the TB Hamiltonian, and the bond-length dependence of the TB parameters are determined according to Harrison's universal d^{-2} law, d being the distance between two atoms under consideration [15]. The term U_{rep} is determined by

$$U_{\text{rep}}(r) = E_{\text{binding}}(r) - E_{\text{BS}}(r), \tag{2.43}$$

where r is the nearest-neighbor distance for the diamond structure. The r-dependence of E_{binding} is taken from first-principles calculations. By assuming that $U(r)$ can be written as a sum of two-body potentials as

$$U_{\text{rep}}(r) = \frac{1}{2N} \sum_{\substack{i,j=1 \\ i \neq j}}^{N} \phi(r_{ij}), \tag{2.44}$$

and that the two-body potential contains only nearest-neighbor interactions, and finally that each nearest neighbor contributes equally to the total two-body potential energy, the pair potential is written as

$$\phi(r_{ij}) = \frac{1}{2}\left[E_{\text{binding}}(r_{ij}) - E_{\text{BS}}(r_{ij})\right]. \tag{2.45}$$

Although the scheme by Wang, Chan, and Ho [12] is simple and useful, the main drawback of this scheme is the TB model used. In particular, the description of the conduction band is very poor in their scheme. Since in chapters 4 and 5 we want to deal with optical properties, a good description of the conduction band is indispensable. In addition, it has been pointed out that, in order to perform calculations for nanostructures by a semi-empirical method such as the TB method, it is necessary that the band structure for the bulk is described accurately [38]. With these situations in mind, we change the TB part of Wang, Chan, and Ho's scheme. The TB model we choose is the nearest-neighbor, two-center, $sp^3s^*d^5$ scheme reported by Jancu *et al.* [39]. In this scheme, an extra s orbital and five d orbitals are added to the minimal basis sp^3 scheme. This TB model gives a very good description of the bulk band structure, and can further stabilize the diamond structure for bulk silicon. In their work, Jancu *et al.* [39] determined the distance dependence of the TB parameters according to the extended Harrison's scheme:

$$H_\alpha = H_\alpha^0 \left(d_0/d\right)^{\nu_\alpha}, \tag{2.46}$$

where d denotes the distance between two atoms, d_0 denotes the bulk nearest-neighbor distance, H_α denotes the Slater-Koster two-center integrals such as $H_{ss\sigma}$, $H_{sp\sigma}$, etc. with respect to d and H_α^0 denotes the same integral with respect to d_0. The ν_α's were determined by fitting to the values of the deformation potentials, obtained from pseudopotential calculations and experiments. Details are found in ref. 39. We show in Figs. 2.3 (a) and (b) the variation of the total energy and E_{BS} with volume change, plotted against the nearest-neighbor distance for Si.

We use the above-described scheme for the evaluation of the band structure energy, and calculate some $T = 0$ K properties of bulk silicon. We use a 64 atom super cell, and the band structure energy is evaluated at the Γ-point. We show our results along with the values obtained by Wang, Chan, and Ho and experiments [12] in table 2.1. We find that the agreement for the phonon frequency is generally not bad.

In order to execute MD simulations, the expression of the force is also needed. The contribution from U_{rep} is trivially calculated by differentiating eq. (2.44). The contribution from E_{BS}, on the other hand, is calculated from the Hellmann-Feynman theorem [2]. The

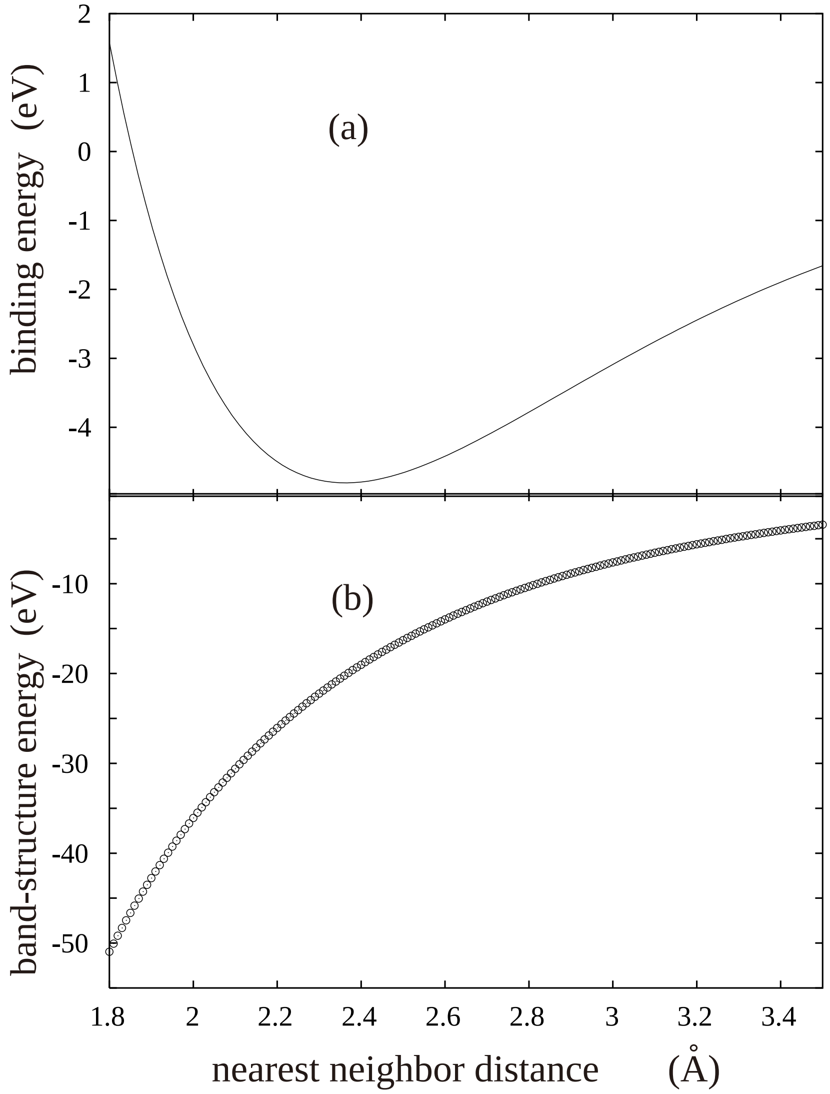

Figure 2.3: Variation of energy with volume change, (a): for the total energy, and (b): for the band-structure energy.

Hellmann-Feynman force acting on atom i, $\boldsymbol{f}_i^{\mathrm{HF}}$, is expressed as

$$\begin{aligned}
\boldsymbol{f}_i^{\mathrm{HF}} &= -2\sum_{n=1}^{N_{\mathrm{occ}}} \frac{\partial \varepsilon_n}{\partial \boldsymbol{r}_i} \\
&= -2\sum_{n=1}^{N_{\mathrm{occ}}} \left\langle \Psi_n \left| \frac{\partial H}{\partial \boldsymbol{r}_i} \right| \Psi_n \right\rangle \\
&= -2\sum_{n=1}^{N_{\mathrm{occ}}} \sum_{i'\nu',i\nu} a^*_{i'\nu',n} a_{i\nu,n} \frac{\partial H_{i'\nu',i\nu}}{\partial \boldsymbol{r}_i},
\end{aligned} \tag{2.47}$$

where x_i denotes Cartesian coordinate of atom i. In the case of non-orthogonal TB, H is

Table 2.1: Some $T = 0$ K properties of bulk Si calculated from our scheme, along with those obtained from the scheme by Wang, Chan, and Ho, and experiments.

	Our model	Wang *et al.*	Experiments
LTO(Γ) THz	14.19	16.95	15.53
TA(X) THz	4.90	4.96	4.49
TO(X) THz	12.08	14.71	13.90
LOA(X) THz	9.49	12.37	12.32

replaced by $H - \varepsilon_n S$, which gives

$$\begin{aligned} \boldsymbol{f}_i^{\mathrm{HF}} &= -2\sum_{n=1}^{N_{\mathrm{occ}}} \left\langle \Psi_n \left| \frac{\partial \left(H - \varepsilon_n S\right)}{\partial \boldsymbol{r}_i} \right| \Psi_n \right\rangle \\ &= -2\sum_{n=1}^{N_{\mathrm{occ}}} \sum_{i'\nu', i\nu} a^*_{i'\nu',n} a_{i\nu,n} \left(\frac{\partial H_{i'\nu',i\nu}}{\partial \boldsymbol{r}_i} - \varepsilon_n \frac{\partial S_{i'\nu',i\nu}}{\partial \boldsymbol{r}_i} \right). \end{aligned} \tag{2.48}$$

Note that, since we are working with the matrix elements of the Hamiltonian instead of the Hamiltonian operator itself, we are calculating the exact derivative of E_{BS}, hence corrections to the so-called "Pulay force" [40] need not be taken into account.

We finally note on the validity of eq. (2.41), in which the binding energy of a system is written as a sum of eigenvalues of a Hamiltonian matrix plus a sum of pair terms. The origin of this expression is not at all clear at first sight. However, in ref. 41, it was shown that the TB expression of the binding energy is very close to the Harris-Foulkes formulation of density functional theory, thereby showing that TB methods have grounds based on *ab initio* methods.

2.4.2 formulation in the case of finite electron temperature

In eq. (2.42), the band-structure energy is evaluated by adding up the one-electron eigenvalue for all occupied states. This policy corresponds to zero electron temperature. It is also possible to work with finite electron temperature. This is particularly of importance in the case of $O(N)$ tight-binding, discussed in the next chapter.

In the case of finite electron temperature, the band-structure energy, E_{BS}, is expressed as

$$E_{\mathrm{BS}} = 2\sum_{i=1}^{N_{\mathrm{level}}} f\left(\varepsilon_n - \mu\right)\varepsilon_n, \tag{2.49}$$

where N_{level} is the number of energy levels, while its derivative is modified as

$$\frac{dE_{\text{BS}}}{d^3r} = 2\sum_{n}^{N_{\text{level}}} \left[f\left(\varepsilon_n - \mu\right) \frac{\partial \varepsilon_n}{\partial \boldsymbol{r}} + \frac{df\left(\varepsilon_n - \mu\right)}{d\left(\varepsilon_n - \mu\right)} \frac{\partial \left(\varepsilon_n - \mu\right)}{\partial \boldsymbol{r}} \varepsilon_n \right]. \tag{2.50}$$

Here, $f\left(\varepsilon_n - \mu\right)$ is the Fermi distribution function,

$$f\left(\varepsilon_n - \mu\right) = \frac{1}{\exp\left[\beta\left(\varepsilon_n - \mu\right)\right] + 1}, \tag{2.51}$$

where μ is the chemical potential of the electronic system, and β is defined as $k_{\text{B}}T_{\text{el}}$, where T_{el} is the electron temperature. Note that the summation of ε_n is now taken for all the energy levels, not only for the occupied levels. The chemical potential of the electron system is determined so as to conserve the number of electrons, calculated as

$$N_{\text{el}} = 2\sum_{n}^{N_{\text{level}}} f\left(\varepsilon_n - \mu\right). \tag{2.52}$$

This procedure is performed easily by using, for example, the Newton-Rapson algorithm.

For a system with a finite electron temperature and a constant number of electrons, it is not appropriate to take the total Hamiltonian, $\mathcal{H}$, as the constant of motion. Rather, it is more appropriate to take the Mermin free energy, defined as

$$\Omega = \mathcal{H} - T_{\text{el}}S_{\text{el}}, \tag{2.53}$$

where S_{el} is the electron entropy,

$$S_{\text{el}} = -2k_{\text{B}}\sum_{n}^{N_{\text{level}}} \left\{ f\left(\varepsilon_n - \mu\right)\log\left[f\left(\varepsilon_n - \mu\right)\right] + \left[1 - f\left(\varepsilon_n - \mu\right)\right]\log\left[1 - f\left(\varepsilon_n - \mu\right)\right] \right\}, \tag{2.54}$$

as the constant of motion [42–44]. In this case, the second term within the summation of the right-hand side of eq. (2.50) is canceled from the contribution from the entropy term, and therefore the forces acting on the atoms are calculated simply as

$$\boldsymbol{f}_i = -2\sum_{n=1}^{N_{\text{level}}} f\left(\varepsilon_n - \mu\right) \frac{\partial \varepsilon_n}{\partial \boldsymbol{r}_i}. \tag{2.55}$$

Note that, in the present formulation, we are effectively taking into account the contribution from the change of μ with respect to atomic displacement, since we are determining μ for each atomic configuration so as to fulfill the conservation of charge.

2.5 Conclusions for this chapter

In this chapter, we give an overview on the TB methods and TBMD methods. We describe the basic formulation of the TB method, along with a brief description on the method of solving the TB problems and on the method of calculating optical properties within the framework of the TB method. We also give a brief review on MD simulations. The basic concept of the method and physical properties calculated by MD simulations are explored. We further give a method of extending the TB method to MD simulations. A simple example for Si are also explained. Finally, we give a description on the method for performing TBMD simulations at finite electron temperature.

Chapter 3

Order-N tight-binding

3.1 Introduction for this chapter

Although the calculations by tight-binding (TB) methods are faster than those by *ab initio* methods, the calculational cost still scales with the third power of the number N of atoms in the system when TB methods are applied in a straight-forward manner, since they require direct diagonalization of the Hamiltonian matrix. In other words, they are essentially $O\left(N^3\right)$ methods. Because of this bottleneck, the calculation time of the TB methods becomes increasingly long as the size of the system increases.

In order to overcome this difficulty, new algorithms have been proposed which deal with the TB problem without carrying out direct diagonalization of the Hamiltonian matrix [11]. Such algorithms commonly use the concept of locality in quantum mechanics, where the locality indicates that the dominating physical properties of a given atom depend only on the behaviors of atoms located within a certain distance from that atom [11]. By using this concept, it is possible to split the large matrix-diagonalization problem into subsets of smaller problems. If the scaling behavior of the smaller problem is better than $O\left(N^2\right)$, we obtain better scaling behavior than $O\left(N^3\right)$ for the whole problem. In particular, if the computational cost of the small problem is constant being independent of N, we have an $O\left(N\right)$ algorithm. Note that the conventional direct diagonalization method (DDM) cannot take advantage of the locality in the way as described here.

One way of using the locality of a system and improving the scaling behavior is to formulate the problem by means of the density matrix. The density matrix is localized in space for semiconductors and insulators, and also for finite-temperature metals [13, 14]. It is noted that almost all physical properties of interest are calculated from the density matrix. There have been several methods proposed on this line, which include the Fermi operator expansion method (FOEM) [10] and the density matrix minimization method [45]. Both methods are $O(N)$ methods under suitable approximations. In the present thesis, in which we study liquid metals, we are concerned only with the former method (FOEM) because the latter method of the density matrix minimization is best suitable for insulators.

In the FOEM, the density matrix is constructed directly from the Hamiltonian matrix by Chebyshev polynomials [27]. This method has been widely used with empirical TB schemes, because (1) the implementation of the method is relatively easy in general and, in particular, the method is easily incorporated in molecular dynamics (MD) simulations, (2) parallel implementation of the method is made very efficiently, and (3) the method deals, by introducing a finite electron temperature, even with metallic systems which are difficult to be treated by other $O(N)$ schemes [11].

In spite of the advantageous features concerning the FOEM as described in the above, successful implementation of the FOEM has so far been limited mostly to orthogonal TB models [10,43,46,47], while extensions to non-orthogonal TB models have rarely been studied. An exceptional example is the work by Stephan and Drabold [48] in which the FOEM was extended to non-orthogonal TB schemes, but tests and actual operations of realistic MD simulations were not performed in their work.

On the other hand, non-orthogonal TB schemes are important in the following respects. First, transferability of TB schemes is greatly improved by explicitly incorporating the non-orthogonality of atomic wave functions. This was seen in our recent work [49] and also in ref. 50. Second, *ab initio* methods based on localized orbitals, to which the FOEM is directly applicable, also require non-orthogonal basis sets. Further, non-orthogonal basis sets are generally more localized than orthogonal basis sets [51].

Judging from all of the above, we find it necessary to further pursue the work done in ref. 48 on $O(N)$ implementation for non-orthogonal TB methods. Of particular importance is to carry out tests and applications of MD simulations to show that the FOEM is really applicable to MD simulations based on non-orthogonal TB methods. This is exactly what we do in the present work. Keeping this in mind, it is the purpose of the present chapter to describe the FOEM, in particular for the case of non-orthogonal TB, and extend it to applications in MD simulations. We further perform test MD simulations.

The rest of the chapter is organized as follows. In section 3.2, we describe the basic formulation of the FOEM. In particular, we discuss the cases of both orthogonal and non-orthogonal TB, and extensions to MD simulations. In section 3.3, we comment on several notes concerning the actual implementation of the method. Finally, in section 3.4, we perform test MD simulations for ℓ-Ge, and show that $O(N)$ TBMD is applicable to the case of non-orthogonal TB models.

3.2 Basic formulation of the Fermi-operator expansion method

Here, we present the way in which the FOEM is formulated and solved both in orthogonal and non-orthogonal TB schemes. Note that, whenever an actual example appears in this chapter, the TB model used is the non-orthogonal TB model described in chapter 6.

In the FOEM, the one-electron density matrix $\boldsymbol{F}$, defined as

$$\boldsymbol{F} = \sum_n f_n \left|\Psi_n\right\rangle \left\langle\Psi_n\right|, \tag{3.1}$$

where f_n is the Fermi distribution function (eq. (2.51)), is used to calculate physical properties. Note that f_n is the eigenvalue of the operator $\boldsymbol{F}$ as is evidently shown in eq. (3.1). The density matrix $\boldsymbol{F}$ allows us to calculate all quantities of interest such as the band-structure energy E_{BS} and the force originating from it. The great advantage of the density matrix is that it is localized in space for insulators and semiconductors, and also for metals with finite electron temperatures [13, 14].

3.2.1 orthogonal tight-binding

We first study, for the sake of comparison, the case in which the atomic orbitals are orthogonal. In this case, the overlap matrix becomes the unit matrix, and therefore the band-structure energy E_{BS} is written, using the density matrix, as

$$E_{\mathrm{BS}} = 2\mathrm{Tr}\left[\boldsymbol{F}\boldsymbol{H}\right], \tag{3.2}$$

while the number of electrons is expressed as

$$N_{\mathrm{el}} = 2\mathrm{Tr}\left[\boldsymbol{F}\right]. \tag{3.3}$$

In this manner, the problem is reduced to the issue of calculating $\boldsymbol{F}$ in an $O\left(N\right)$ fashion.

In the FOEM, the density matrix is directly fitted by means of the Chebyshev polynomials as a matrix functional. Using the j th-order Chebyshev polynomial $\boldsymbol{T}_j\left(\boldsymbol{H}\right)$, the density matrix is expressed as [10, 27]

$$\boldsymbol{F}(\boldsymbol{H}) = \frac{c_0}{2}\boldsymbol{I} + \sum_{j=1}^{N_{\mathrm{pl}}} c_j \boldsymbol{T}_j\left(\boldsymbol{H}\right), \tag{3.4}$$

where c_j's are expansion coefficients, $\boldsymbol{I}$ is the unit matrix, and N_{pl} is the number of the Chebyshev polynomials taken into account, which we set as 70 in this work.

The Chebyshev polynomials are calculated without reference to the function to be fitted by using the following recursive relation of the Chebyshev polynomials [27],

$$\begin{aligned} \boldsymbol{T}_0\left(\boldsymbol{H}\right) &= \boldsymbol{I} \\ \boldsymbol{T}_1\left(\boldsymbol{H}\right) &= \boldsymbol{H} \\ \boldsymbol{T}_j\left(\boldsymbol{H}\right) &= 2\boldsymbol{T}_{j-1}\left(\boldsymbol{H}\right)\boldsymbol{H} - \boldsymbol{T}_{j-2}\left(\boldsymbol{H}\right). \end{aligned} \tag{3.5}$$

Equation (3.5) is calculated in an $O\left(N\right)$ fashion when the range of the matrices $\boldsymbol{H}$ and $\boldsymbol{F}$ are finite. We hereafter refer to the range of $\boldsymbol{H}$ and $\boldsymbol{F}$ as r_H and r_F, respectively. In practice, the $O\left(N\right)$ scaling is achieved by the following manner. Firstly, when no decay properties are taken into account at all, we have $O\left(N^3\right)$ scaling, since we have a matrix-matrix multiplication in line 3 of eq. (3.5), which requires N^2-times column-vector operations. Next, when the sparseness of the Hamiltonian matrix is taken into account, the scaling behavior reduces to $O\left(N^2\right)$, since the number of non-zero matrix elements for a given vector of $\boldsymbol{H}$ in the column-vector operation is independent of N. Finally, we obtain $O\left(N\right)$ scaling by performing column-vector operations for $\boldsymbol{T}_j$ and $\boldsymbol{H}$ only when they correspond to atoms within r_F. Note that, not only the calculational cost, but also memory requirements scale as $O\left(N\right)$ in the present scheme.

On the other hand, the expansion coefficients c_j's are calculated solely from the function to be estimated in the following manner [27]

$$c_j = \frac{2}{N_{\mathrm{pl}}} \sum_{k=1}^{N_{\mathrm{pl}}} \mathcal{F} \left[\cos \left(\frac{\pi \left(k - \frac{1}{2} \right)}{N_{\mathrm{pl}}} \right) \right] \cos \left(\frac{\pi \left(j - 1 \right) \left(k - \frac{1}{2} \right)}{N_{\mathrm{pl}}} \right), \tag{3.6}$$

where the function $\mathcal{F}$ denotes the function to be fitted. In the present case of evaluating eq. (3.4), we have $\mathcal{F} = f_n$.

3.2.2 non-orthogonal tight-binding

In the second place, we study the case in which the atomic orbitals are non-orthogonal. In this case, the overlap matrix is no longer an unit matrix, but all of the above arguments hold if we use the matrix $\overline{\boldsymbol{H}} = \boldsymbol{S}^{-1}\boldsymbol{H}$ instead of the Hamiltonian matrix $\boldsymbol{H}$ itself [48]. By using $\overline{\boldsymbol{H}}$, eq. (2.6) becomes formally equivalent to the case of an orthogonal TB model for which we have

$$\overline{\boldsymbol{H}} C_n = \varepsilon_n \boldsymbol{I} C_n. \tag{3.7}$$

We note, however, that the matrix $\overline{\boldsymbol{H}}$ is not Hermite in general. Using $\overline{\boldsymbol{H}}$, E_{BS} is calculated as:

$$E_{\mathrm{BS}} = 2\mathrm{Tr} \left[\boldsymbol{F} \left(\overline{\boldsymbol{H}} \right) \overline{\boldsymbol{H}} \right], \tag{3.8}$$

and therefore it becomes possible to apply the FOEM as explained in the above without any substantial changes. The problem is now reduced to the question of finding a way to calculate either $\boldsymbol{S}^{-1}$ or $\overline{\boldsymbol{H}}$ efficiently.

In general, the calculation of an inverse matrix such as $\boldsymbol{S}^{-1}$ requires $O\left(N^3\right)$ operations. To overcome this difficulty, several ideas have been proposed [52]. In the present article, we employ the algorithm proposed in ref. 53 and used in ref. 48. The algorithm is based on the idea of dividing one large matrix-inversion problem into many small problems. In this algorithm, the inverse matrix is never calculated, but instead, the following linear equation,

$$\boldsymbol{S}\overline{\boldsymbol{H}} = \boldsymbol{H}, \tag{3.9}$$

is solved to obtain $\overline{\boldsymbol{H}}$. When localization of the matrices is not taken into account, the matrix equation (3.9) corresponds to N_{level} simultaneous linear equations with matrix size

$(N_{\text{level}} \times N_{\text{level}})$; hence a straight-forward approach to eq. (3.9) will end up in $O\left(N^3\right)$ operations. However, these equations couple only within the range of $\boldsymbol{S}$, $\boldsymbol{H}$, and $\overline{\boldsymbol{H}}$, and therefore it is possible for us to divide the equations into many small problems. Since the computational cost for solving each small problem is independent of the system size, we are able to calculate this equation in a strictly $O\left(N\right)$ fashion. We hereafter refer to the range of $\overline{\boldsymbol{H}}$ as $r_{\bar{H}}$.

Now let us move on to the calculation of the force in the present scheme. Here, we only describe the contribution from E_{BS}. By differentiating eq. (3.8) with respect to the position x of a certain atom, we obtain

$$\frac{dE_{\text{BS}}}{dx} = 2\text{Tr}\left[\boldsymbol{F}\frac{\partial\overline{\boldsymbol{H}}}{\partial x} + \frac{d\boldsymbol{F}\left(\overline{\boldsymbol{H}} - \mu\boldsymbol{I}\right)}{d\left(\overline{\boldsymbol{H}} - \mu\boldsymbol{I}\right)}\frac{\partial\left(\overline{\boldsymbol{H}} - \mu\boldsymbol{I}\right)}{\partial x}\overline{\boldsymbol{H}}\right]. \tag{3.10}$$

As described in chapter 2, the constant of motion for a system with finite electron temperature is the Mermin free energy, Ω. In this case, the second term of eq. (3.10) exactly cancels out the contribution from the electron entropy, and consequently, all we have to calculate for the force from E_{BS} is the first term of eq. (3.10). By noting that $\frac{\partial \boldsymbol{S}^{-1}}{\partial x} = -\boldsymbol{S}^{-1}\frac{\partial \boldsymbol{S}}{\partial x}\boldsymbol{S}^{-1}$, the first term of eq. (3.10) is calculated as

$$\begin{aligned}\boldsymbol{F}\frac{\partial\overline{\boldsymbol{H}}}{\partial x} &= \boldsymbol{F}\left[\boldsymbol{S}^{-1}\frac{\partial\boldsymbol{H}}{\partial x} - \boldsymbol{S}^{-1}\frac{\partial\boldsymbol{S}}{\partial x}\overline{\boldsymbol{H}}\right] \\ &= \overline{\boldsymbol{F}}\left[\frac{\partial\boldsymbol{H}}{\partial x} - \frac{\partial\boldsymbol{S}}{\partial x}\overline{\boldsymbol{H}}\right],\end{aligned} \tag{3.11}$$

where $\overline{\boldsymbol{F}} = \boldsymbol{F}\boldsymbol{S}^{-1}$. The range of $\overline{\boldsymbol{F}}$ is also finite, and we denote this range as $r_{\bar{F}}$. The matrix $\overline{\boldsymbol{F}}$ is calculated in an $O\left(N\right)$ fashion by the same algorithm as used to calculate $\overline{\boldsymbol{H}}$. We note that the matrices $\overline{\boldsymbol{H}}$ and $\overline{\boldsymbol{F}}$ are not in general Hermite, meaning that the ordering of eq. (3.11) is important.

We find that in practice, the computational costs for the calculations of the matrices $\overline{\boldsymbol{H}}$ and $\overline{\boldsymbol{F}}$ are much smaller than those for the calculations of the recursive fit, eq. (3.5) (refer to the next section). Therefore, non-orthogonal TB methods are calculated almost as efficiently as in the case of orthogonal TB methods by the FOEM.

3.3 Notes on the actual implementation

3.3.1 electron temperature

In our $O(N)$ non-orthogonal TBMD method, we introduce finite electron temperature T_{el}. The purpose of introducing finite electron temperature is twofold; *i.e.*, (1) to make the FOEM applicable to metallic systems, and (2) to save the computational cost. In the first place, the introduction of finite electron temperature is especially of importance for metallic systems, because for metallic systems, the density matrix is localized only when the electrons have a finite temperature [13, 14]. Concerning the second point, calculational costs are lower for higher electron temperature. This is because for high electron temperature, (1) the Fermi distribution function becomes smoother near the Fermi energy, which allows us to perform the fitting procedure with fewer Chebyshev polynomials, and (2) the localization of the density matrix becomes stronger [11]. On the other hand, it is not allowed to set the temperature too high to be physically meaningful.

It is possible to estimate the effects of electron temperature on calculational cost from the following arguments. Firstly, as discussed in ref. 11, the adequate choice for the degree of the Chebyshev polynomials roughly scales as the inverse of the electron temperature, *i.e.*, $N_{\mathrm{PL}} \propto (k_{\mathrm{B}}T_{\mathrm{el}})^{-1}$. Next, the scaling behavior of r_F with respect to the electron temperature is estimated as $r_F \propto (k_{\mathrm{B}}T_{\mathrm{el}})^{-1}$. This is derived from the following decay property of the density matrix for a finite-temperature metal,

$$F(|\boldsymbol{r}-\boldsymbol{r}'|) \propto k_F \frac{\cos(k_F|\boldsymbol{r}-\boldsymbol{r}'|)}{|\boldsymbol{r}-\boldsymbol{r}'|^2} \exp\left(-c\frac{k_{\mathrm{B}}T_{\mathrm{el}}}{k_F}|\boldsymbol{r}-\boldsymbol{r}'|\right), \tag{3.12}$$

where $\boldsymbol{r}$ and $\boldsymbol{r}'$ are the position vectors of two atoms under consideration, k_F is the Fermi wavelength, and c is some constant of order 1. Since the calculational cost scales as the number of atoms within r_F, the increase of the calculational cost from the increase of r_F is estimated as $r_F^3 \propto (k_{\mathrm{B}}T_{\mathrm{el}})^{-3}$. From the above arguments, the increase of the calculational cost with the decrease of electron temperature is estimated as $\sim (k_{\mathrm{B}}T_{\mathrm{el}})^{-4}$. This is, unfortunately, a significant increase, so from the view point of calculational cost, it is preferable that we take the electron temperature as high as possible.

In order to choose an optimum value for T_{el}, we have tested the effects of T_{el} in a preliminary

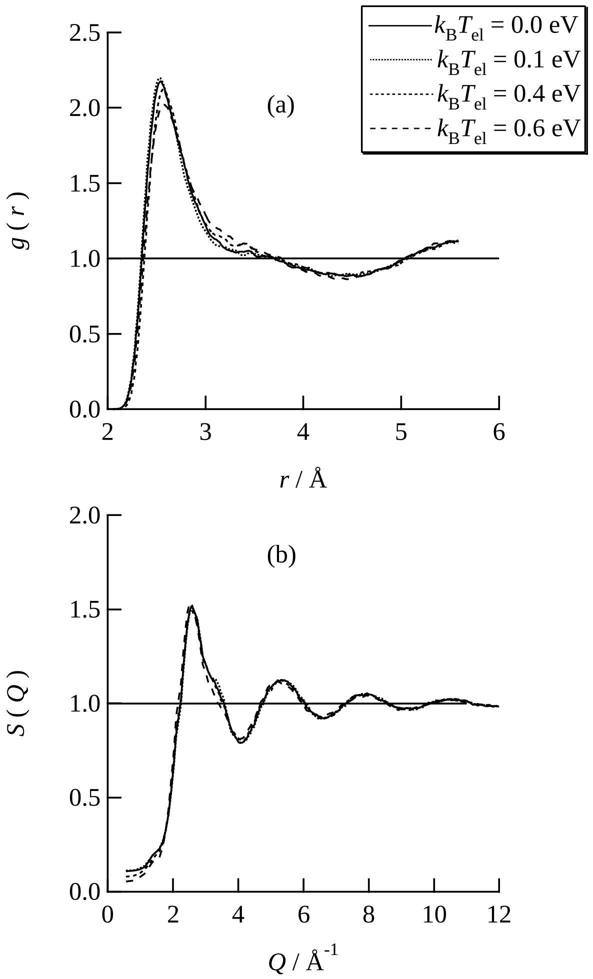

Figure 3.1: Distribution function calculated for ℓ-Ge at several electron temperatures, (a) : two-body distribution function $g(r)$, and (b) : static structure factor $S(Q)$.

MD simulation for ℓ-Ge. We show $g(r)$ and $S(Q)$ calculated for $k_\mathrm{B}T_\mathrm{el} = 0.0, 0.1, 0.4,$ and 0.6 eV in Fig. 3.1. We find that up to $k_\mathrm{B}T_\mathrm{el} = 0.4$ eV, structural properties are almost identical, but for $k_\mathrm{B}T_\mathrm{el} = 0.6$ eV, we find slight deviations from liquid structures obtained at a lower electron temperature. Therefore we adopt $k_\mathrm{B}T_\mathrm{el} = 0.4$ eV as an optimum value for the electron temperature throughout this work.

3.3.2 the expansion coefficients for the density matrix

Now we give several notes concerning eq. (3.6).

First, it is possible to make the conservation of charge fulfilled by modifying the chemical potential μ in the Fermi distribution function included in eq. (3.6), so that eq. (3.3) is satisfied to a certain precision. This is performed at virtually no extra computational cost, since the most time-consuming part of the calculation is the recursive fit of eq. (3.5). If this procedure is omitted, the method will conserve the chemical potential for the electronic system instead of the number of electrons, $N_{\rm el}$.

Secondly, we note that, in general, eq. (3.6) decreases exponentially as j increases [27]. We show c_j, plotted against j, in Fig. 3.2. We utilize this property of c_j to speed up calculations.

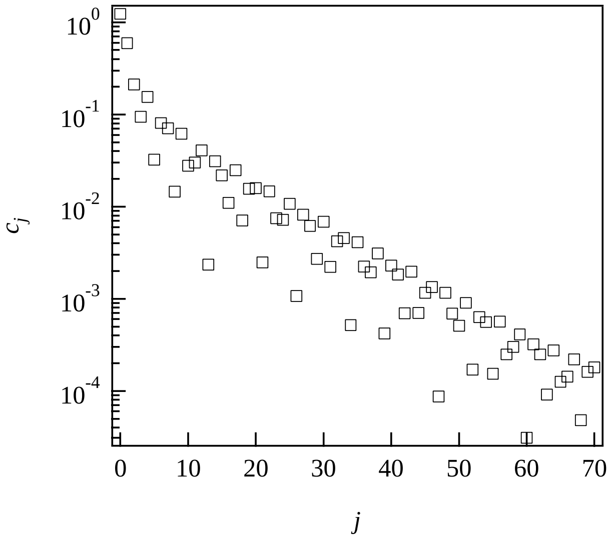

Figure 3.2: The expansion coefficients for the density matrix, c_j, plotted against j.

Since c_j for large j are relatively unimportant, $\boldsymbol{T}_j(\boldsymbol{H})$ for larger j is substituted by that calculated with a shorter cutoff distance. By this scheme, we accomplish a speed-up by about a factor of two. In addition, we obtain an increase in the degree of the stability for the calculations.

Finally, we introduce a new technique concerning the calculation of c_j, which significantly reduces the memory requirements for our calculations. In the above arguments, it is necessary to store all non-zero matrix elements of $\boldsymbol{T}_j$ at one time in order to conserve the total charge of the system. This constraint leads to large memory requirements when the density of atoms in the system is high. In particular, our NTB model is not a simple nearest-neighbor model, which significantly increases memory requirements. When performing MD simulations, it is possible to improve this point by changing the way we calculate the expansion coefficients c_j's, in which all the information regarding charge conservation is included. Instead of using the expansion coefficients calculated at the time step under consideration, we use expansion coefficients calculated one step before. This procedure allows us to store only the diagonal elements of $\boldsymbol{T}_j$, which results in a reduction of memory requirements by about a factor of 20. The drawback of this technique is that the exact conservation of charge is no longer fulfilled. However, the effects of this drawback are ignorable. We show this situation in Fig. 3.3. In this figure, the number of electrons per atom is plotted against simulation time. We find from this figure that the fluctuation of the number of electrons is less than 0.05%, which will give virtually no effects on the essential results of our simulations.

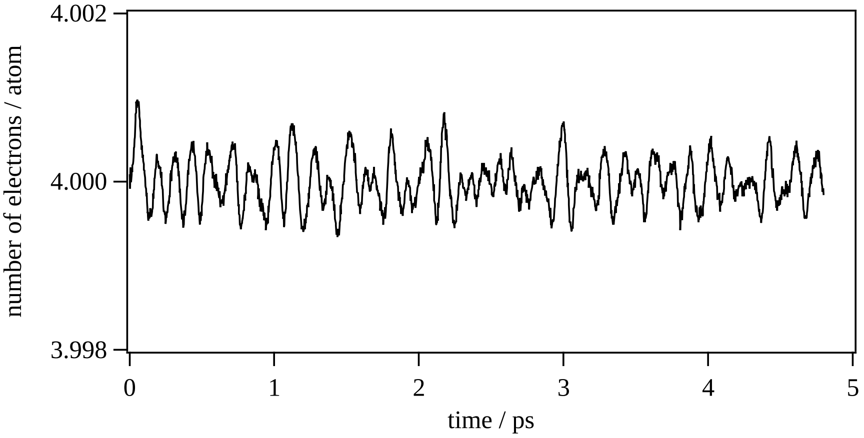

Figure 3.3: The number of electrons, plotted against simulation time. Note that the exact value is four.

3.3.3 cutoff distances

We have four cutoff distances in our $O(N)$ non-orthogonal TBMD method, namely, r_H, r_F, $r_{\bar{H}}$, and $r_{\bar{F}}$. Here, we discuss the adequate choice for these distances.

Firstly, r_H depends on the original TB scheme. This value is to be chosen so that the matrix elements are sufficiently small at this distance. We find that the value of $r_H = 5.63$ Å, which was adopted in ref. 49, is sufficient. The value of $r_{\bar{H}}$ is necessary in order to calculate eq. (3.9). In general, the inverse matrix of a sparse matrix is not sparse, meaning that $\overline{\boldsymbol{H}}$ is not necessarily a sparse matrix. However, as discussed in ref. 53, in many cases the matrix elements of $\overline{\boldsymbol{H}}$ decay faster than those of $\boldsymbol{H}$. This property of $\overline{\boldsymbol{H}}$ allows us to disregard matrix elements of $\overline{\boldsymbol{H}}$ corresponding to two atoms separated by distance longer than r_H, *i.e.*, to set $r_{\bar{H}} = r_H$. We find this choice to be sufficient for our calculations.

Next, we take into account the range of the density matrix, r_F. The range of the density matrix is in general longer than $r_{\bar{H}}$. The value of r_F gives effects to all pairs of atoms (not only for pairs of atoms with distance r_F apart) through the recursive fit of eq. (3.5), which makes it difficult for us to obtain good enough energy conservation in MD simulations without taking a large value for r_F. In particular, simulations of liquids require a very large value for r_F. This is because in MD simulations, the largest error occurs when atoms enter or leave the region within r_F, which frequently occurs for liquids. On the other hand, it is possible to use smaller values of r_F for crystalline systems. From trial and error, we adopt the value of $r_F = 9.85$ Å for liquids, and $r_F = 6.47$ Å for crystals.

Lastly, we choose the value of $r_{\bar{F}}$. The situation is similar to the case of $r_{\bar{H}}$, but a large difference is in that the matrix $\overline{\boldsymbol{F}}$ acts only on very localized matrices, namely, $\frac{\partial \boldsymbol{H}}{\partial x}$ and $\frac{\partial \boldsymbol{S}}{\partial x}\overline{\boldsymbol{H}}$ (eq. (3.11)). Therefore, we find it sufficient to take $r_{\bar{F}}$ equal to r_H or $r_{\bar{H}}$. This is a huge advantage compared to the case of $r_{\bar{F}} = r_F$, because eq. (3.9) requires $O\left(N_{\bar{F}}^2\right)$ operations, where $N_{\bar{F}}$ is the number of atoms within $r_{\bar{F}}$, which means that the total computational cost for calculating eq. (3.9) is $O\left(r_{\bar{F}}^6\right)$. We find that in our implementation, by choosing $r_{\bar{H}} = r_{\bar{F}} = r_H$, computational costs necessary to calculate $\overline{\boldsymbol{H}}$ and $\overline{\boldsymbol{F}}$ are much smaller than those required by the recursive fit (about 10 %), meaning that non-orthogonal TB models are calculated almost as efficiently as orthogonal TB models by the FOEM.

3.4 Test molecular dynamics simulations

Keeping all of the above points in mind, we perform test MD runs for crystalline and liquid Ge. Simulations are performed for $N = 512$, in the $NV\Omega$ ensemble (note that Ω is defined by eq. (2.53), the Mermin free energy). Specific conditions of the calculations are described in the preceding sections.

In Fig. 3.4, the conservation of the Mermin free energy is shown, along with the fluctuation of the potential and kinetic energies. We find from this figure that energy conservation is satisfactory in both cases. In MD simulations, small fluctuations, if any, in the constant of motion are tolerable, since they give virtually no effects to the statistical averages we want to evaluate.

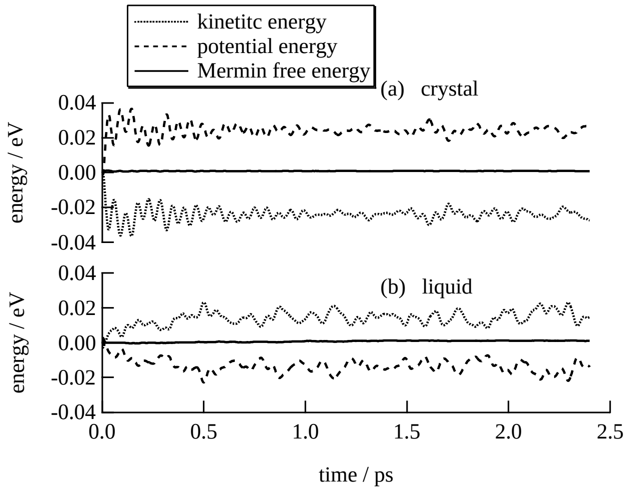

Figure 3.4: The behavior of the kinetic, potential, and Mermin free energies, plotted against simulation time, (a) : for crytalline system, (b) for liquid system.

We perform another test with $N = 64$, in order to compare the structures generated by DDM and FOEM. The calculations are performed in the liquid phase, with exactly the same initial condition in the $NV\Omega$ ensemble. The calculated pair correlation function $g(r)$ and static structure factor $S(Q)$ from DDM and FOEM are shown in Fig. 3.5. We find from these figures that, within the scatter of our data, the two methods give virtually identical structures.

We further show in Fig. 3.6 the cpu time necessary to perform one MD step in the present scheme and in DDM, plotted against the number of atoms in the system. We find from this figure that the scaling of the computational cost is in fact $O(N)$ in FOEM, and at $N = 512$, FOEM is considerably faster than DDM. We also find that the computational costs for crystalline systems are smaller than liquid systems by about a factor of four to five, since we use a shorter $r_{\bar{F}}$ for crystalline systems. We finally note that, although the results of the test simulations in the $NV\Omega$ ensemble are demonstrated in the present subsection, the essential conclusions drawn from these tests hold for test simulations in the NVT ensemble as well.

3.5 Conclusions for this chapter

In the present chapter, $O(N)$ TB methods are taken into account. In particular, TB methods based on non-orthogonal basis sets are successfully calculated in $O(N)$ fashion. We further

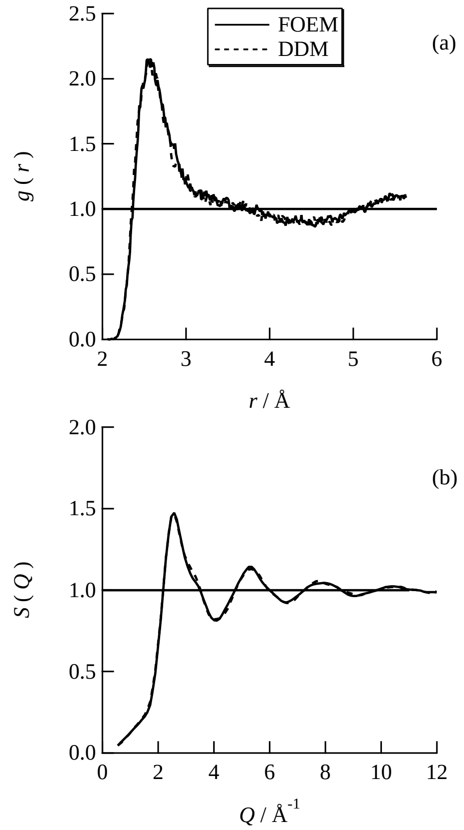

Figure 3.5: Comparison between the structural properties obtained from the Fermi-operator expansion method and the direct-diagonalization method, (a) : two-body distribution function $g(r)$, and (b) : static structure factor $S(Q)$.

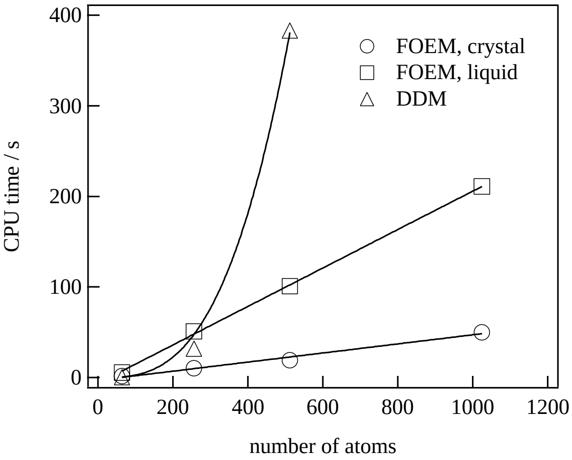

Figure 3.6: Computational time necessary to perform one MD step, plotted against the number of atoms in the system N.

integrate the $O(N)$ non-orthogonal TB methods into molecular dynamics calculations. In performing these calculations, we introduce several new techniques concerning the calculation of the expansion coefficients for the density matrix. Test MD simulations are performed, which show that the FOEM is applicable to realistic MD simulations even in the case of non-orthogonal TB method. Moreover, we find that the application of the FOEM for non-orthogonal TB is almost as efficient as that for orthogonal TB. To our knowledge, this is the first report on the successful application of $O(N)$ non-orthogonal TBMD based on the FOEM.

Chapter 4

Silicon nanostructure without point-group symmetry

4.1 Introduction for this chapter

Since the innovative discovery of efficient, visible, and room temperature photoluminescence (PL) from porous (π-) [17] and nanocrystalline (n-) [18] silicon (Si), the phenomenon has been extensively studied throughout the world. Much work has been performed on the topic, but a detailed understanding of the exact origin and mechanism of this phenomenon has not been reached [54].

Silicon is a dominant material in the present-day microelectronics technology. However, because of its indirect band structure and band gap of 1.1 eV in the infrared region, it has not been possible to use Si as light-emitting devices. For this reason, the discovery of the efficient, visible PL from low-dimensional Si is remarkable from a technological point of view, because it opens the possibility to the use of Si as light-emitting devices compatible with Si-based optoelectronic integrated circuits [54].

In addition, this phenomenon is interesting from a physical point of view, since the essential mechanism has not yet been clarified for the appearance of the efficient light emission as a result of a drastic reduction of size and dimensionality of Si all the way down to the order of nanometers [54]. Canham proposed that the origin of the efficient, visible light emission is free-standing Si wires, whose band gap is broadened by the quantum confinement (QC) effect [17]. Since the original proposal, much work has been done in order to confirm this statement.

For the visible PL, possibilities other than QC effect were sought for by many workers. Based on their experimental findings, several proposals have been made as candidates for the origin of the efficient luminescence which include hydrogenated amorphous Si formed on the surface of Si nanostructures [55], surface hydrides [56], particular molecules (such as siloxene) [57], and surface states [58]. All of these proposals are expected to be possible explanations for the phenomenon.

And yet, we argue that, in spite of all these proposals from experiments, the source of the efficient PL in Si nanostructures must be searched in quantum-confined Si itself. The grounds for our assertion are the facts (1) that PL has been observed from Si prepared in a wide variety of conditions [59], and (2) that the phonon-related steps appear in the PL spectra obtained from resonant excitations [60–63].

For this reason, it is the purpose of our study in the present and succeeding chapter to understand the essential aspects of the electronic and optical properties of quantum-confined Si itself without going into the details of individual samples. In particular, we lay our focus on the theoretical elucidation of the unsolved problem concerning the mechanism related to the so-called ‘S’ (slow) and ‘F’ (fast) band in the radiative recombination time for PL [20].

In order to clarify our standpoint, it is worth giving a brief review of the theoretical situation about the study of light-emitting Si [29, 30, 64–71]. So far, quite a few theoretical calculations have been carried out on the electronic states and the radiative recombination time. These calculations have revealed that

1. the band gap increases according to the decrease of the system size,
2. one- and two-dimensional nanostructures have direct band structures,
3. the direct transitions between states near or at the band edges give a finite oscillator strength,
4. oscillator strength increases as the system size is reduced.

These results are generally in good agreement with experiments, and lend support to the QC hypothesis.

On the other hand, no theoretical attempts published so far have succeeded in achieving quantitatively correct values for the radiative recombination time τ [29,30]. As for the 'S' band, the theoretical value of τ derived from the oscillator strength is larger than the experimental value almost by two orders of magnitude. As for the 'F' band, there is no theoretical study performed by now.

Before presenting our model, it is appropriate to mention the characteristics of the 'S' and 'F' band [20].

For the 'S' band, we have that [20]

1. the emission extends over the energy region approximately between 1.4 eV and 2.2 eV,
2. the values for τ range from several micro seconds to several tens of micro seconds,
3. τ increases as the emission energy E_{PL} decreases,

while for the 'F' band, we have [20]

1. the emission extends over the energy region approximately between 1.8 eV and 3.2 eV,
2. the values for τ range from several nano seconds to several tens of nano seconds,
3. τ is independent of the emission energy.

Occasionally, the 'S' band is taken in the broad sense by including those that would fulfill only the third characteristic (3), i.e., τ increases as E_{PL} decreases.

It is important to find the origins for these behavior of τ since the emission intensity is evaluated by the inverse of τ, the radiative recombination rate. Our assertion is that these problems are solved by introducing realistic model atomic structures for nanostructures, which is realized by lifting the symmetry of systems and/or reducing the quantitative order in bond length and angles. The models previously studied are limited to nanocrystalline structures with high symmetry of the point-group. The advantage of dealing with symmetric models is that the high symmetry makes calculations much easier to perform by applying group theory. The disadvantage, on the other hand, is that the models do not manifest real nanostructures and therefore bring about incorrect results for physical properties.

In the present chapter, we study the effects due to the removal of the point-group symmetry from model atomic structures, and show that the low-symmetry structures account for the features of the 'S' band. In the succeeding chapter, we present that, when the quantitative order in structures is reduced, the features of the 'F' band is derived.

The rest of the chapter is organized as follows. In section 4.2, our model nanostructure is introduced, along with a brief description of our calculation scheme. In section 4.3, our results for one-dimensional system are described. One-dimensional Si nanostructures are important in that they have been regarded as model of π-Si [17], the most widely-used material for light-emitting Si. Further, we discuss our results for zero-dimensional and two-dimensional systems in section 4.4. Finally, we will conclude the present chapter in section 4.5.

4.2 Model and calculational scheme

There exist various techniques to prepare Si nanostructures, which include deposition, etching and chemical treatments at high temperatures. The prepared samples are 2D thin films, 1D wires and 0D dots (small spheres). Porous Si is regarded as either 1D or 0D, depending on the situation.

The size of a nanostructure is measured by the '*thickness*' of a thin film, by the '*width*' of a wire, or by the '*diameter*' of a dot (a sphere). These sizes are order of nanometer, which is the grounds for the name of '*nanostructure*'. When the thickness, the width or the diameter is as small as nanometer scale, the quantum mechanical effects for electrons show up on macroscopic physical properties. In the case of a thin film, for example, the potential which an electron feels is finite within the film, while it is infinite outside of the film, thus exhibiting an image of an electron being confined in a well when viewed along the axis perpendicular to the film surface. In this context, a thin film with a thickness of nanometer scale is called a '*quantum well*'. Similar consideration is the basis for the naming of a '*quantum wire*' for a wire with the width of a nanometer scale and a '*quantum dot*' for a dot with the diameter of a nanometer scale. In many occasions, the prepared samples of Si nanostructures have the same topological connectivity of chemical bonds as bulk crystalline (c-) Si despite the smallness of sizes [72].

One of the most troublesome surface effect is that it causes the appearance of dangling bonds on the surface, each of which gives rise to an energy level within the band gap, undesirable from the view point of light-emitting devices, since the levels in the gap degrade the emission efficiency via non-radiative recombination processes. In many nanostructures used in experiments, these obstructive dangling bonds are terminated by hydrogen, oxygen or nitrogen atoms. The stability and the optical properties of nanostructures are also influenced by the kinds of these terminator atoms.

In the construction of our theoretical structure models, with these situations in mind, our policy is, for the fruitful discussion of Si nanostructures, to extract the essential features of nanostructures, without being bothered by trifles and details. Along this policy, we construct our structure models of Si nanosystems in the way as demonstrated in the following.

In Fig. 4.1, we show our model nanostructures. Every model in Fig. 4.1 is constructed by cutting each appropriate shape out of bulk Si of diamond crystalline structure. Note that any dangling bonds which arise in our models are passivated by hydrogen atoms. Figs. 4.1 (a) and (b) correspond to 0D models, Figs. 4.1 (c) and (d) to 1D models, and Figs. 4.1 (e) and (f) to 2D models.

(1) 0D quantum dots (QDs)

Symmetric shapes such as spheres as shown in Fig. 4.1 (a) are cut out, and accordingly, the obtained shapes have high symmetry in atomic configurations. Ellipsoids cut out of bulk *c*-Si also belong to this category, where some aspects of symmetry are still maintained. Models in Fig. 4.1 (b) are constructed by cutting out non-symmetric shapes composed of atoms whose numbers are almost as many as in the case of Fig. 4.1 (a). There exists no symmetry in the atomic configurations of this type.

(2) 1D quantum wires

Models in Fig. 1 (c) represent thin wires (or square pillars to be precise), which are cut out along the [001] axis in such a way that the symmetry is high. In this figure, the distribution of atoms belonging to the four layers in the unit cell of a thin wire is depicted as a projection onto a (001) plane, where all the atoms are expressed by gray spheres of the same size, thus leaving out, for simplicity, the description for the relative positions along the direction parallel to the [001] axis. The situation is clearly explained

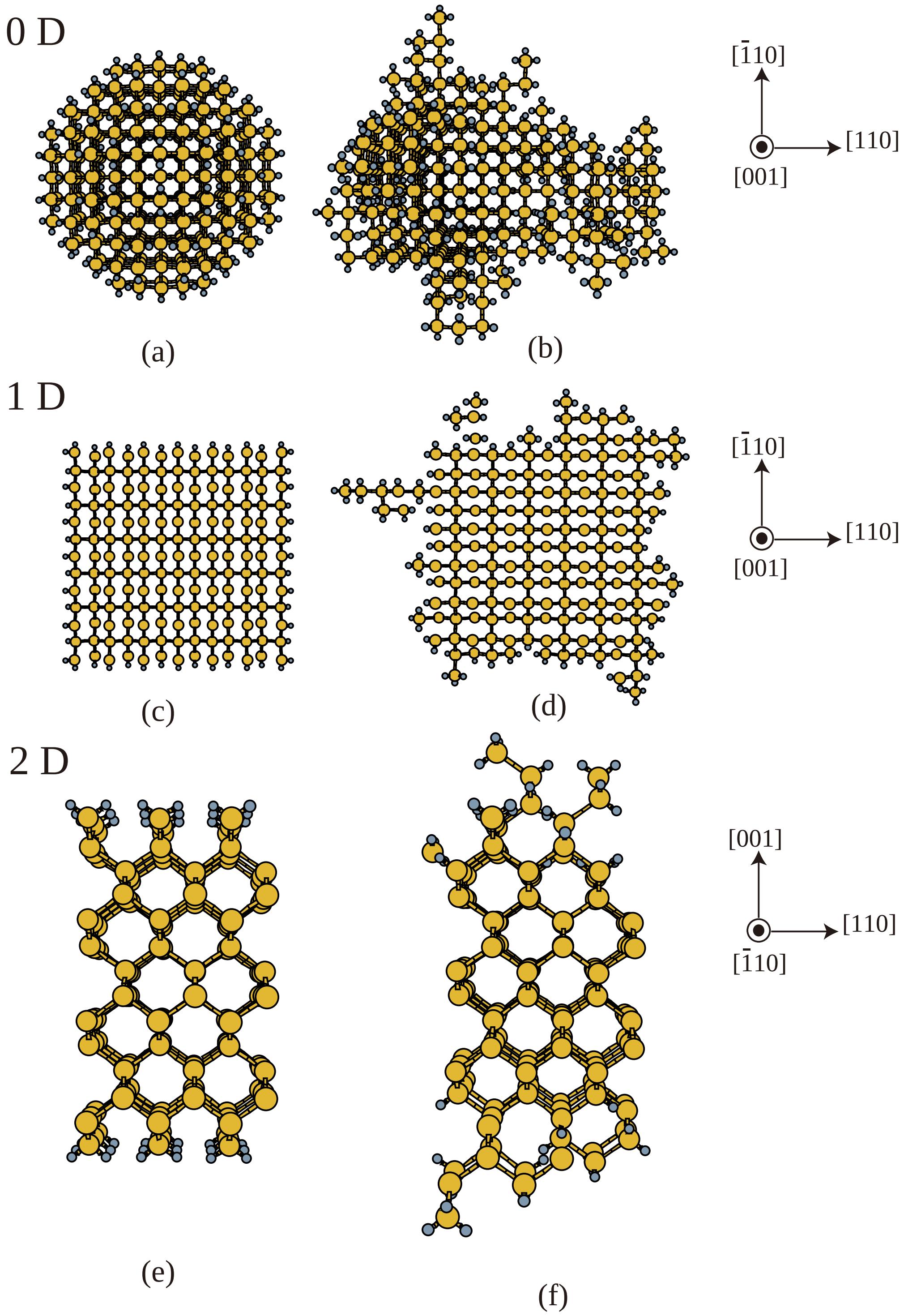

(a) (b) (c) (d) (e) (f)

Figure 4.1: Typical examples of our structure models. In all cases presented here, models are constructed by cutting out of bulk crystalline silicon (c-Si) with the diamond structure, some appropriate shapes which could be either two dimensional (2D), one dimensional (1D) or zero dimensional (0D). In each figure, a larger sphere represents a Si atom, while a smaller sphere denotes an terminator such as a hydrogen atom. Details of model construction are found in the text.

by Fig. 4.2, which is also a projection of Si atoms onto a (001) plane. In the figure, the relative positions of Si atoms along the [001] axis are expressed by the sizes of black circles, positions being at 0, $a/4$, $2a/4$, and $3a/4$ in the direction of the [001] direction, where a is the lattice constant of a diamond crystal. Notation H in Fig. 4.2 stands for a hydrogen atom introduced to terminate a dangling bond on the surface.

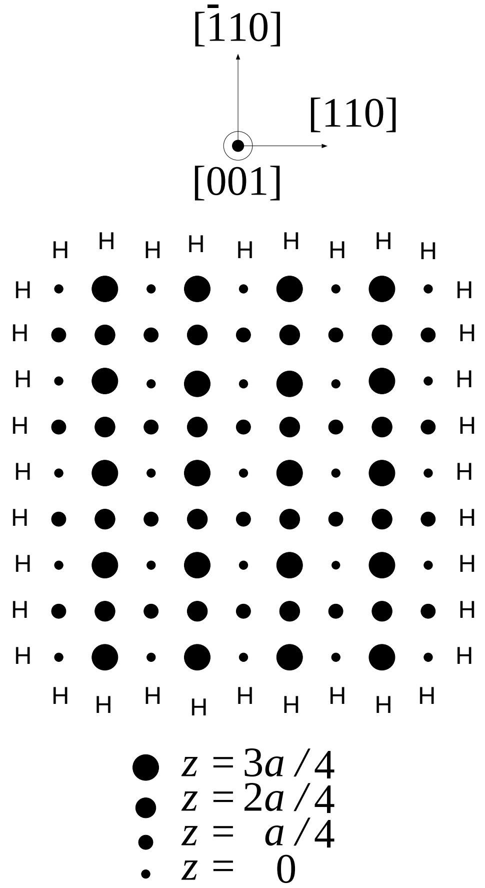

Figure 4.2: The atomic distribution in the unit cell of a thin wire as shown in Fig. 4.1 (c) is depicted as a projection onto a (001) plane so as to explain the relative positions of atoms in the direction of the [001] axis. Details are explained in the text.

Figure 4.1 (c) has the $p\bar{4}m2$ symmetry, and it is generally called an '$N \times N$ *quantum wire*'. Models are also made by cutting out, instead of a square pillar, a $N \times M$ rectangular pillar, which is usually called an '$N \times M$ *quantum wire*'.

In Fig. 4.1 (d), an example of non-symmetric thin wires, composed from comparative number of atoms as in Fig. 4.1 (c), is shown. Note that Fig. 4.1 (d) is also a projection of atoms in the four layers. Both wires presented in Figs. 4.1 (c) and (d) are obtained by stacking, periodically in the z direction (parallel to the [001] direction), the unit cells, each of which contains four layers. Accordingly, our wires are infinite in the z direction.

(3) 2 D quantum wells

Models as shown in Fig. 4.1 (e) are constructed by cutting out thin films in parallel with the (001) plane so that the symmetry is high, while models as shown in Fig. 4.1 (f) are constructed by randomly adding some atoms onto the surfaces of the thin films in Fig. 1 (e) so that the atomic configurations are made non-symmetric. Both films in Fig. 4.1 (e) and (f) are made to have the two-dimensional periodicity within the (001) place, or in other words in the x-y plane. As a consequence, our thin films are infinite in the x and y directions.

The periodic boundary conditions for 1D models in the z direction and for 2D models in the (001) plane are both introduced for the sake of calculational convenience. Except for these periodicity, none of models in Figs. 4.1 (b), (d) and (f) have space-group symmetry in atomic configurations.

For each model described in the above, we calculate the electronic states by the tight-binding method, and show band structures, energy gap E_{g}, and the thermally-averaged radiative recombination time, $\langle\tau\rangle$. The tight-binding method we use here is the third-neighbor, three-center, sp^3, orthogonal scheme presented in ref. 26. The parameters for the Si-H bonds were also determined in ref. 26 in such a way that the eigenvalues for the silane molecule are reproduced accurately. Through the investigation of $\langle\tau\rangle$, we obtain information concerning the transition between near-band-edge states. In order to study the full band, we also calculate the imaginary part of the dielectric function, ε_2.

4.3 Results 1 : the case of one dimension

We first study the case of the one-dimensional model. Note that this model has been used in the interpretation of the photoluminescence from π-silicon [17].

4.3.1 band structure

We show in Figs. 4.3 (a) and (b) the band structure calculated for the atomic configuration shown in Figs. 4.1 (a), 13 × 13 wire, and 4.1 (c), a low-symmetry wire with 182 Si atoms and 100 H atoms per unit cell. These systems have comparative band gaps, about 1.5 eV (blue-shifted compared to the bulk).

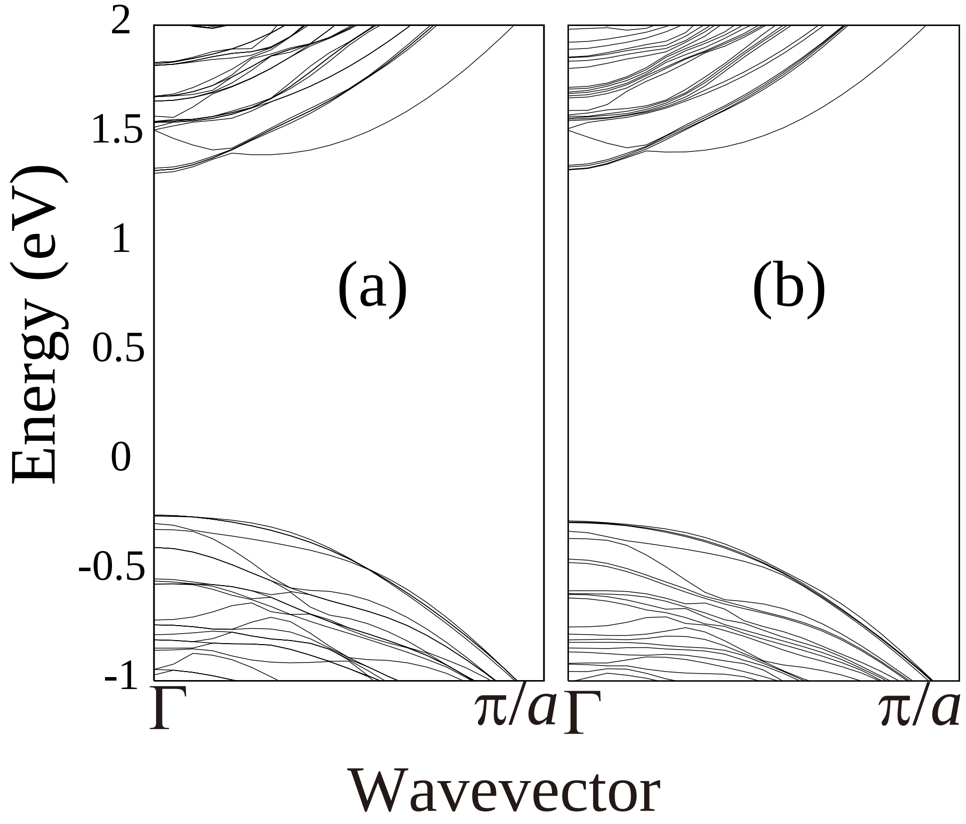

Figure 4.3: Band structure of quantum wires; (a) is the band structure for the unit cell shown in Fig. 4.1 (c), and (b) is the band structure for the unit cell shown in Fig. 4.1 (d). Both have band gap of about 1.5 eV, and are direct at the Γ-point. Parameter a in the figure denotes the lattice constant of the unit cell.

We see from Figs. 4.3 (a) and (b) that the band structure is direct at the Γ-point for both systems, as expected from previous studies [29, 67–70].

The overall dispersion of the band is similar for the two cases, except that there are many degenerate levels for the 13 × 13 wire, reflecting its symmetry.

Band structures for other unit cell were also studied, and they show more or less the same tendencies. The difference in symmetry does not substantially affect the band structure in all cases; they are all direct, blue-shifted compared to the bulk, and have the same overall dispersion.

4.3.2 relation between band gap and size

In Fig. 4.4, the optical band gap is plotted against the size of the unit cell (number of Si atoms per unit cell). The results are shown for the $N \times N$ and $N \times M$ wires, and for the low-symmetry wires. There are already a number of studies for high-symmetry systems which investigated the relation between band gap E_g and the size of the system, and all of them have stated that E_g shifts to the blue as the system size becomes smaller, reflecting the QC effect. [29, 30, 64–71] Similar results are shown in Fig. 4.4 by filled circles for high-symmetry systems and by open circles for low-symmetry systems.

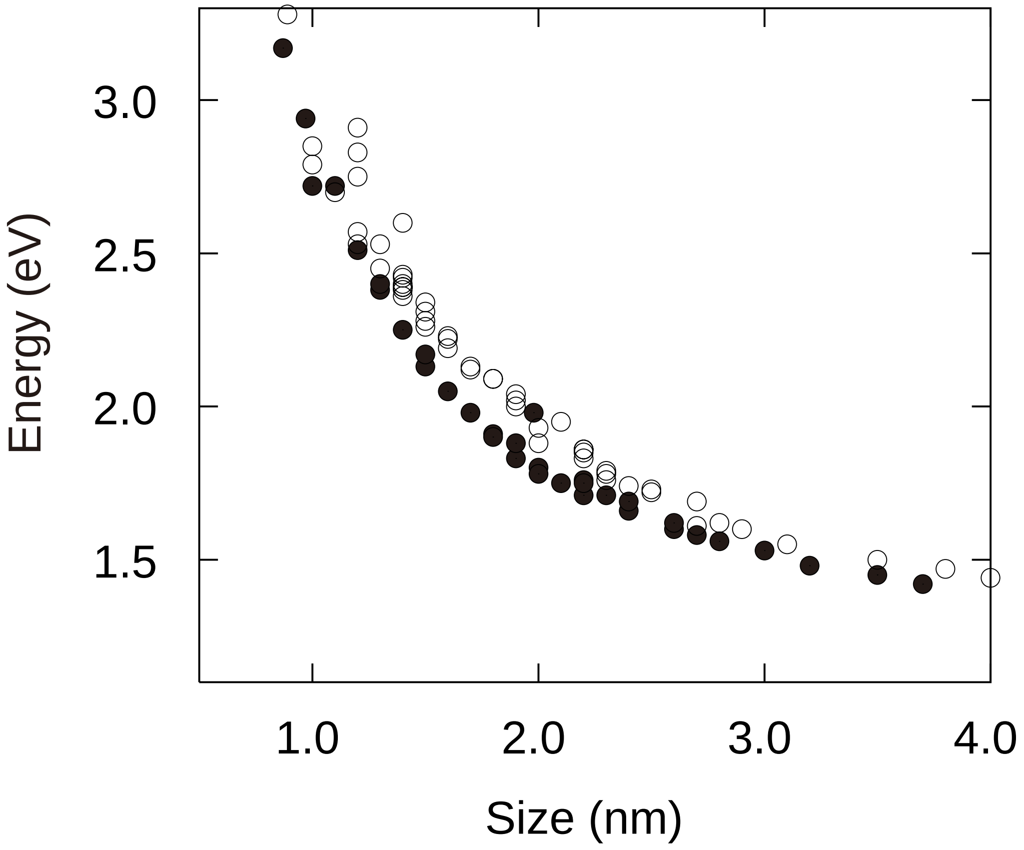

Figure 4.4: Optical band gap, E_g, plotted against the width of the wire. Open circles denote results from the low-symmetry model, while filled circles denote results from the high-symmetry model.

It is not surprising that we obtain results consistent with the QC hypothesis even for the low-symmetry systems. The interesting feature in Fig. 4.4 is that E_g is slightly larger for the low-symmetry wires than for the high-symmetry wires in all sizes. This result implies that the blue-shift of the band gap is induced not only from the QC effect, but also from the reduction in the degree of symmetry in nanostructures. It must be noted, however, that this difference is not substantial. From Fig. 4.4, we conclude that the band gap of a quantum wire is mainly governed by the QC effect, with some modifications coming from symmetry properties.

It is possible to understand the physical meaning of the slight blue-shift in terms of the effective coordination number of the Si atoms. For the high-symmetry wires, the effective coordination number is high (although much lower than the bulk value of four), while for the low-symmetry wires, it is lower. Therefore, when compared to the high-symmetry wires, the band width is narrower for the low-symmetry wires, which leads to a larger band gap.

4.3.3 relation between energy and the thermally-averaged radiative recombination time

We show in Fig. 4.5 the thermally-averaged radiative recombination time $\langle\tau\rangle$ (at 300 K) plotted against the PL emission energy E_{PL} for the $N \times N$, $N \times M$, and low-symmetry wires. The experimental results for π-Si, reproduced from ref. 73, are also shown for comparison.

The relation between τ and E_{PL} was studied in previous works for the high-symmetry structures, and it was shown that radiative recombination time (or the inverse of the oscillator strength) increases as E_{PL} decreases (or as size increases) [30, 54]. It was pointed out that τ increases (or the oscillator strength decreases) rather rapidly as E_{PL} decreases, and is inconsistent with experiments at low (<2.0 eV) energies [29, 30, 54].

We see from Fig. 4.5 that the results for the low-symmetry unit cell wires are qualitatively different from the results of the $N \times N$ and $N \times M$ wires. The results for the $N \times N$ and $N \times M$ wires are consistent with previous works; $\langle\tau\rangle$ increases rapidly as E_{g} decreases, and is inconsistent with experiments at lower energies. On the other hand, The results for the low-symmetry wires show a slower increase in $\langle\tau\rangle$, and is consistent with experiments at all energy range.

When the energy changes from 2.2 eV to 1.5 eV, $\langle\tau\rangle$ changes by more than two orders of magnitude for the $N \times N$ and $N \times M$ wires, while the change is about one order for the low-symmetry wires. The behavior of the latter is not only qualitatively very similar to

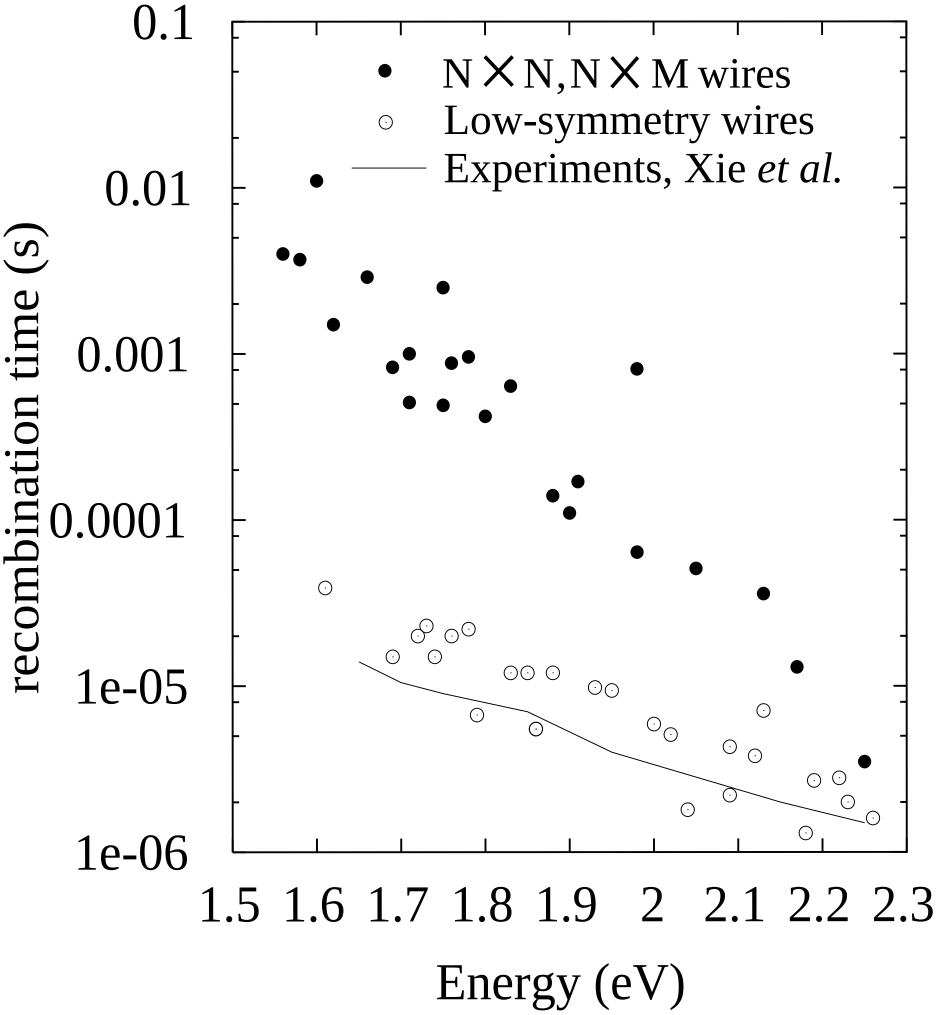

Figure 4.5: The thermally-averaged radiative recombination time plotted against the PL emission energy E_{PL} for the low- and high-symmetry wires. The results of PL decay measurements, reproduced from ref. 73, are also plotted for comparison.

experiments, but also quantitatively, as can be seen from Fig. 4.5.

Our results show that symmetry changes the oscillator strength considerably for these wires, especially for low-energy transitions. The physical meaning of this result is as follows.

Firstly, in the case of bulk Si, both the conduction and valence bands have p-symmetry, which leads to zero oscillator strength. Secondly, for the $N \times N$ and $N \times M$ wires, the translational symmetry of bulk Si is broken, which invokes mixing between s and p states at states near or at the band edge. This leads to a finite oscillator strength. In order to confirm this point, we present in Fig. 4.6 the s-p ratio for states near the band edge. Thermal average is taken as in the case of τ. From this figure, we see that as the gap energy increases

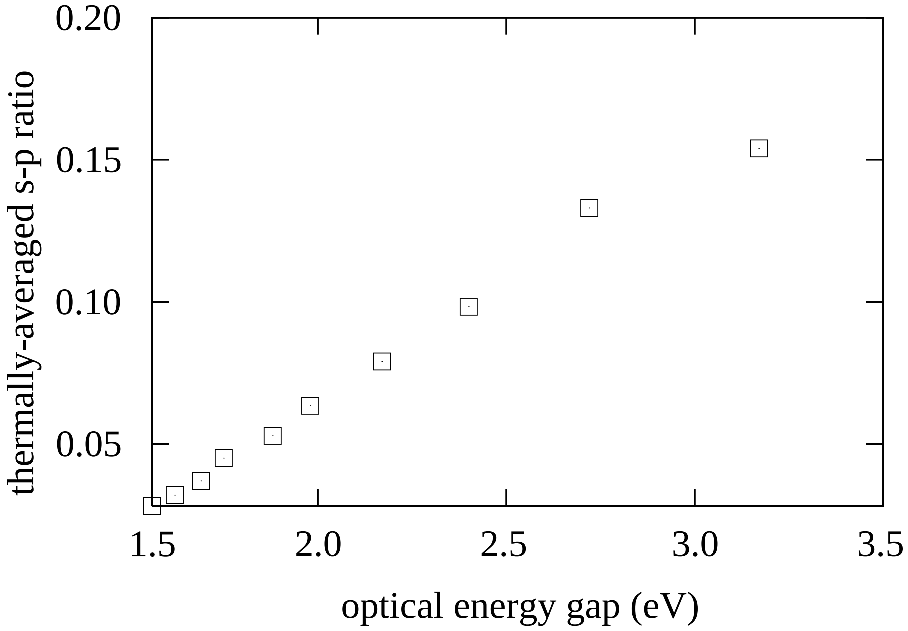

Figure 4.6: The thermally-averaged *s*-*p* ratio for $N \times N$ wires, plotted against optical band gap.

(or, as the size of the system decreases), the *s*-*p* ratio increases. This behavior accounts for the increase of τ with the decrease of the system size. However, since the symmetry of the atomic configurations and wave functions is still high, many of the terms in the summation in eq. (2.16) cancel. Finally, for the low-symmetry wires, there is no symmetry in the atomic configurations and wave functions, and all the terms in the summation in eq. (2.16) effectively contribute to the oscillator strength. In other words, the selection rule for angular momenta is relaxed when we deal with non-symmetric wires. For this reason, the low-symmetry wires give the largest values for the oscillator strength.

Before concluding the present argument, let us comment on the rather large scatter of the data for $\langle\tau\rangle$ shown in Fig. 4.5. The origin of this scatter has been discussed by Delerue, Allan and Lanoo in ref. 30. The first reason for the scattering is that symmetry of the electron and hole states varies very sensitively to the size and shape of nanostructures. The electron and hole states are highly degenerate for bulk Si, but the degeneracy is lifted in the case of nanostructures. Since the lifting of the degeneracy is different from system to system even for nanostructures of comparable size, the scattering of $\langle\tau\rangle$ arises. The second reason is that, as discussed by Hybertsen from an analytical point of view by the effective-mass theory [74], the overlap of the electron and hole wave functions is a strongly oscillating function of the size of a nanostructure. This situation is illustrated in Fig. 4.7, in which the overlap of electron and hole wave functions, plotted against nanocrystallite size, is depicted (the figure is from ref. 74). Since this overlap is roughly proportional to the oscillator strength, the data for $\langle \tau \rangle$ becomes scattered.

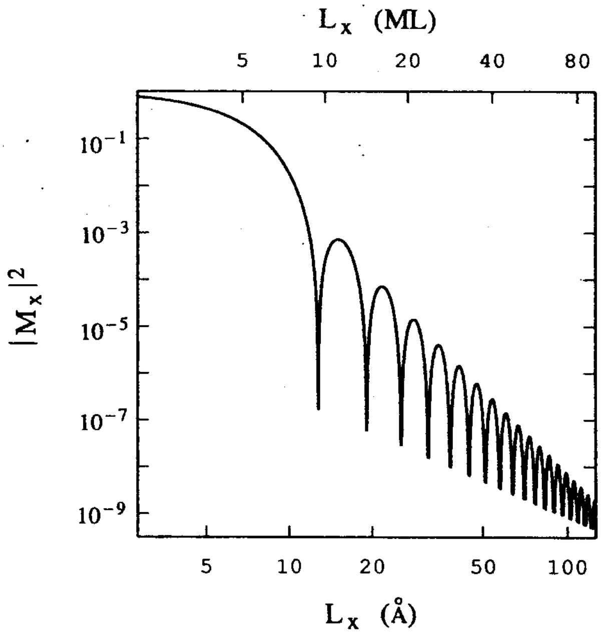

Figure 4.7: The overlap of electron and hole wave function, plotted against nanostructure size. Reproduced from ref. [74].

4.3.4 calculation of ε_2

The thermally-averaged radiative recombination time reflects the low-energy structure of the energy band. In order to investigate the structure of the full band, we calculate the imaginary part of the dielectric function, ε_2, polarized in the z-direction. Since it is not informative to show the results for all the structures we calculate, we show, as an example, the results obtained for the atomic configurations shown in Figs. 4.1 (a) and (c). These two configurations have comparative band gaps (about 1.5 eV).

In Fig. 4.8 (a), ε_2 for the full band is shown. We note that at this scale, the $N \times N$ and low-symmetry wires have almost the same values for ε_2. The only noticeable difference is that the 13×13 wire has non-continuous derivatives at several points, reflecting its symmetry. The change in symmetry most seriously influences the oscillator strength for transitions near or at

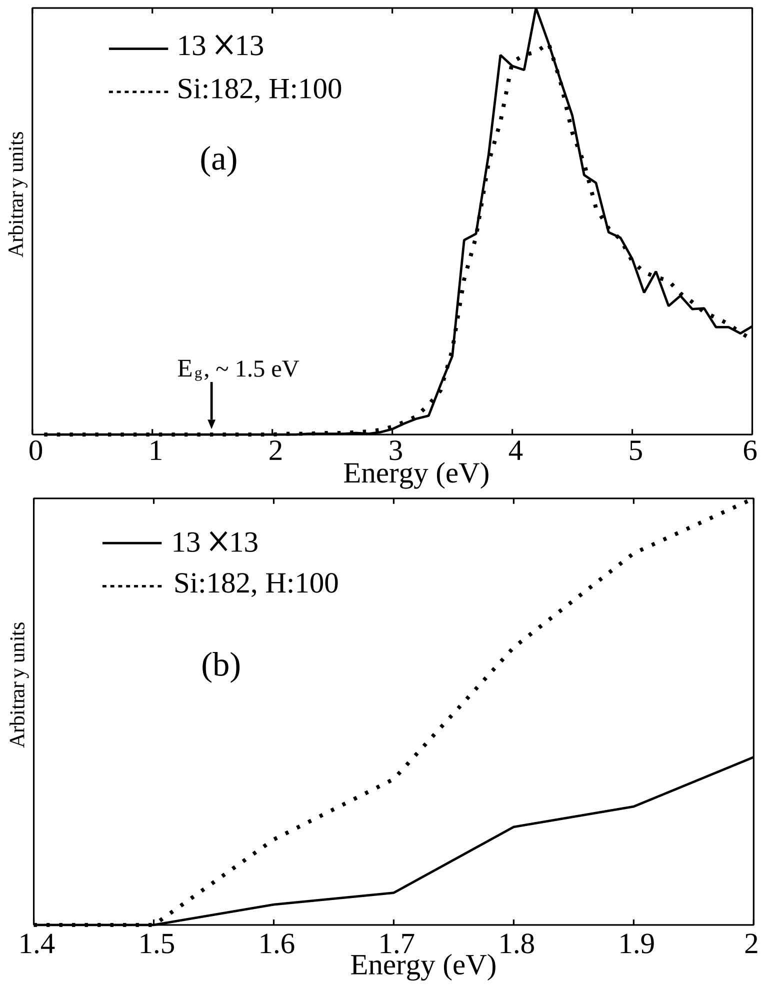

Figure 4.8: The imaginary part of the dielectric function ε_2 for the structure of Figs. 4.1 (c) and (d). The solid line corresponds to Fig. 4.1 (c), while the dotted line corrsponds to Fig. 4.1 (d). In (a), spectrum up to 6 eV is shown, while in (b), spectrum is shown for 1.5 eV to 2.0 eV.

the band edge; we see at this scale no substantial difference between the two.

The most relevant feature in Fig. 4.8 (a) is that near the band edge (about 1.5 eV), ε_2 seems to be ignorablly small. This result is consistent with experiments [75], and implies that Si nanostructures, in a sense, have indirect-like properties. In fact, ε_2 is very similar between bulk Si and nanostructured Si, as shown in Fig. 4.9, in which we compare ε_2 of bulk Si and Si quantum wire. The fact that Si nanostructures have indirect-like properties does not mean, however, that there are no direct transitions near or at the band edge, as we saw in the previous subsection.

In Fig. 4.8 (b), ε_2 for $\hbar\omega = E_{\rm g}$ to $E_{\rm g} + 500$ meV is shown. Since 500 meV corresponds to temperatures well above room temperature, Fig. 4.8 (b) contains information that is not

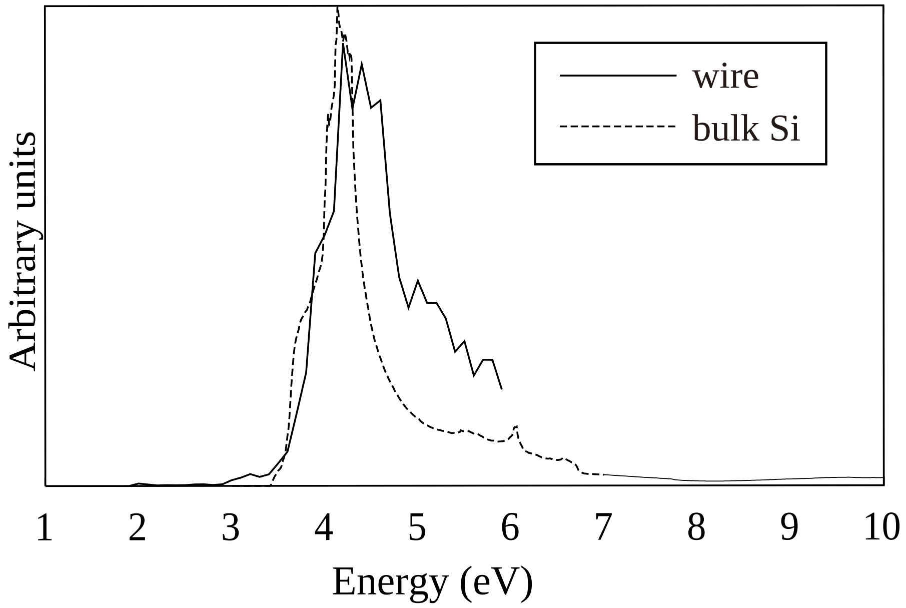

Figure 4.9: Comparison of the imaginary part of the dielectric function ε_2, solid line : Si quantum wire, dashed line : bulk Si.

included in $\langle\tau\rangle$. At this scale of Fig. 4.8 (b), we observe considerable difference between the two systems under consideration. The low-symmetry system has much better optical response than the high-symmetry system, even for transitions 500 meV above the band edge.

There is no substantial difference between the high- and low-symmetry systems for the full spectra, but when transitions near the band edge are studied, we observe substantial differences, up to about 500 meV above band edge. This result is consistent with the results obtained in the previous subsection, and can be interpreted in the same way.

The tendency that the low-symmetry wires have larger oscillator strengths persists up to 500 meV above band edge, but when the full spectrum is studied, there is no essential difference. This is because at higher energies, the optical response from states which correspond to bulk direct states come into play. Although the band edge states for the low-symmetry wires give considerable oscillator strength, it is much smaller than the oscillator strength coming from states corresponding to bulk direct states, which is not affected by the difference in symmetry of the unit cell. For this reason, ε_2 for the full spectra is virtually the same for the high- and low- symmetry structures, and the contribution to ε_2 from the higher-energy transitions is much larger than the contribution from the lower-energy transitions.

4.3.5 stokes shift

Before concluding this section, we mention the structural relaxation which occurs for the excited states. When an electron is excited from the valence band to the conduction band, the distribution of electrons changes, which triggers the rearrangement of the atomic configuration. In many cases, this structural relaxation does not cause drastic changes, such as reconstruction of the connectivity or topology for the bonds, but only the bond lengths and bond angles are modified to a certain degree. The electronic distribution in turn is varied as a result of the structure relaxation for atomic positions, and therefore the band structure is also influenced. The schematic idea of the conversion is shown in Fig. 4.10. When this modification of the band structure brings about the emission energy lower than the incident energy, the so-called Stokes shift takes place.

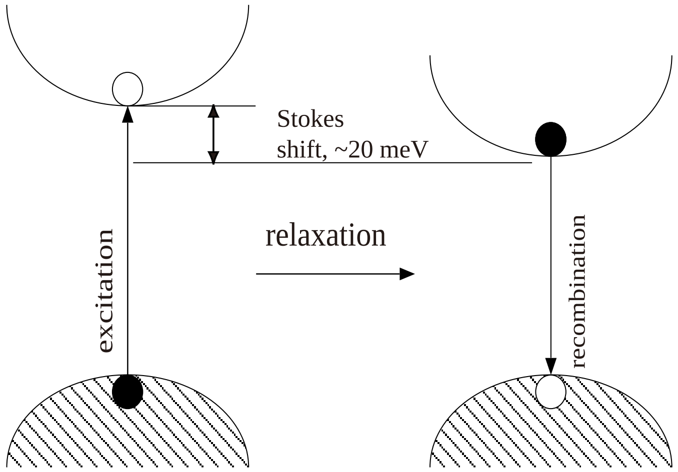

Figure 4.10: A schematic drawing on the mechanism of the Stokes shift.

In chalcogenide glasses, the structural relaxation originating from the rearrangement of the electron distribution is expected to happen more or less readily due to the fact that the coordination number is two (or in other words, there are only two bonds per atom), and that there exist the lone pairs which make the atomic structure flexible. Materials such as nanostructures are also subject to the structural relaxation because of the high percentage of surface atoms which are easily shifted. By taking this point into account, we allow the structure relaxation after the excitation of electrons, and examine the change of the band structure. Structural relaxation is evaluated by the simple tight-binding total energy method described in chapter 2. Our calculations clarify that the magnitude of the Stokes shift is about 20 meV. This result shows that the effect of the structural relaxation on E_g is not significant.

4.4 Results 2 : the case of zero and two dimension

In the present section, we further study the case of zero dimension and two dimension for the model described in Fig. 4.1.

4.4.1 band structures and band gaps

In Figs. 4.11 (a)-(c) and 4.12 (a) and (b), the optical band gap is plotted against the size of the nanostructures. Each of Figs. 4.11 (a)-(c) presents comparison between the two models which have the same dimension, while each of Figs. 4.12 (a) and (b) demonstrates comparison among the three different dimensions which belong to the same model.

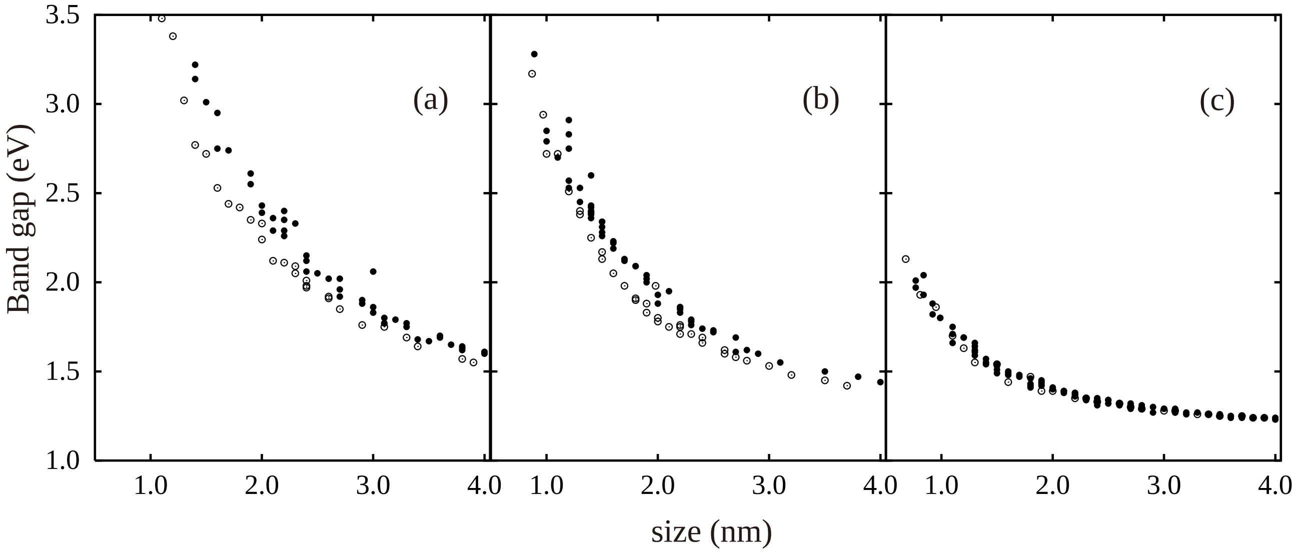

Figure 4.11: The optical band gap plotted against the size of the system. Each of the three figures presents comparison between the two models with the same dimension: (a) 0D, (b) 1D, and (c) 2D Si nanostructures. The open circles represent the results for the 'high-symmetry' models, while the filled circles represent the results for the 'low-symmetry' models.

Similar results are obtained for both 'high-symmetry' and 'low-symmetry' model, as can be seen from Figs. 4.11 and 4.12; the optical band gap is blue-shifted as the size is decreased for both model structures.

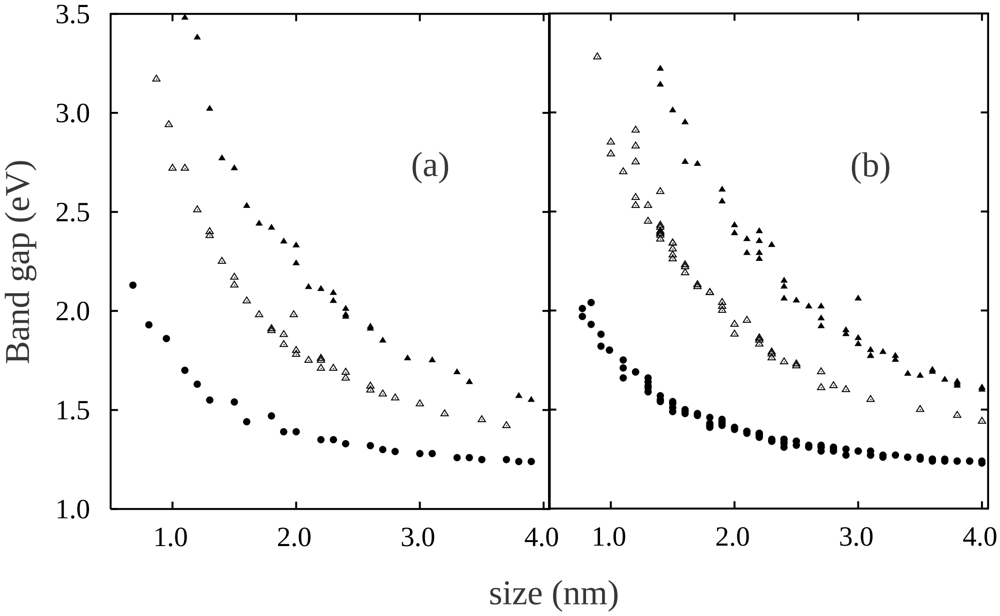

Figure 4.12: Optical band gap plotted against the size of the system. Each of these figures presents comparison among the three different dimensions which belong to the same model: (a) 'high-symmetry' model and (b) 'low-symmetry' model Si nanostructures. The filled traiangles represent the results for 0D systems, the open triangles represent the results for 1D systems, and the filled circles represent the results for 2D systems.

The values of E_g for 'low-symmetry' model systems are slightly larger than those for 'high-symmetry' model systems in all sizes for 0D and 1D systems, while it is almost the same for 2D systems. This result is interpreted by the same mechanism as described in the previous section.

It can be seen from Figs. 4.12 (a) and (b) that for both 'high-symmetry' and 'low-symmetry' model, 0D structures have the largest blue-shift, and as the dimension of the nanostructure becomes higher, the blue-shift becomes smaller. This result is understood in terms of the difference in confinement dimension. The confinement dimension for 0D nanostructures is three-dimension, while that for 1D and 2D nanostructures are two- and one-dimensions, respectively. It comes out straightforwardly that the higher the confinement dimension, the larger the blue-shift, as shown in Figs. 4.12 (a) and (b).

From the results obtained here, we conclude that the optical band gap E_g (1) increases as the system size decreases, (2) increases as the dimension of the system decreases, and (3) is not influenced very much by the symmetry of the system. These results imply that it is possible to control the energy of the luminescence by controlling the size and dimension of the nanostructures.

We finally note that all structures calculated have direct band structures (which is a trivial concept for 0D systems). Examples of the band structures for 1D and 2D systems are shown in Figs. 4.13 (a) and (b).

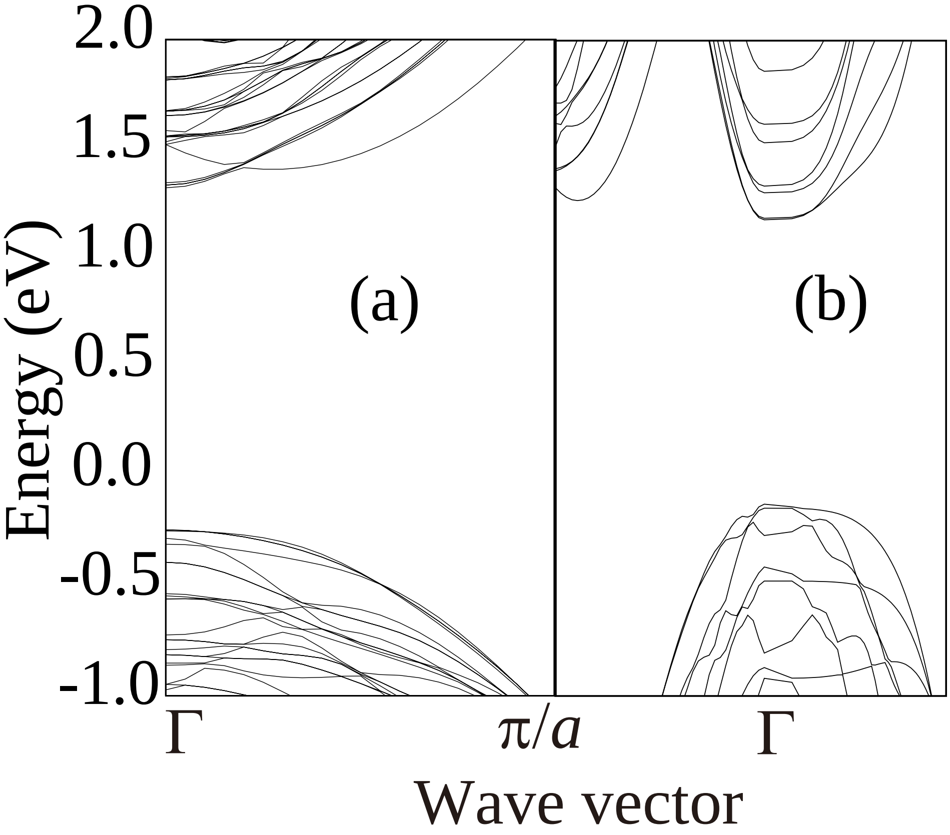

Figure 4.13: Band structures for (a) 1D and (b) 2D Si nanostructures. Both are for 'high-symmetry' models; similar results are obtained for 'low-symmetry' model structures.

4.4.2 radiative recombination rate

In Figs. 4.14 (a)-(c) and 4.15 (a) and (b), we show the results obtained for radiative recombination rates (the inverse of the radiative recombination time, hereafter referred to as $\langle \frac{1}{\tau} \rangle$), plotted against the size of the nanostructures. Each of Figs. 4.14 (a)-(b) shows comparison between the two models which have the same dimension, while each of Figs. 4.15 (a) and (b) shows comparison among the three different dimensions which belong to the same model.

Firstly, we point out that, from Figs. 4.14 and 4.15, the general tendency is that radiative recombination rate increases as the system size decreases. This result is consistent with

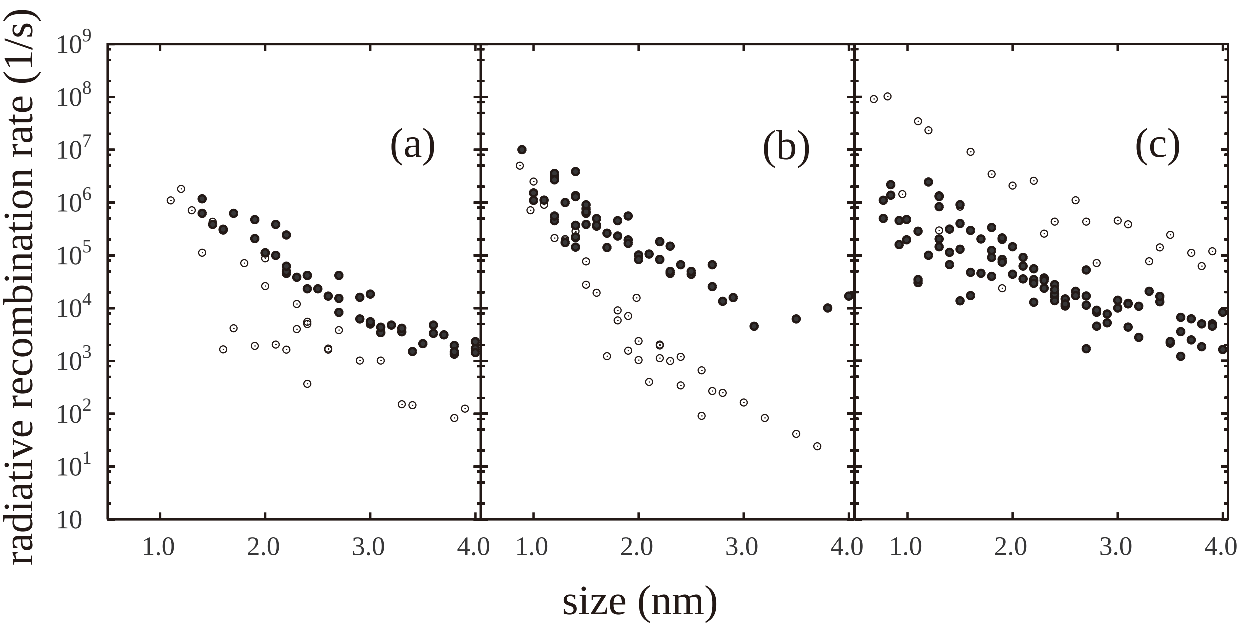

Figure 4.14: Thermally-averaged radiative recombination rate plotted against the size of the system. Each of the figures present comparison between the two models with the same dimension: (a) 0D, (b) 1D, and (c) 2D Si nanostructures. The open circles represent the results for the 'high-symmetry'models, while the filled circles represent the results for the 'low-symmetry' models.

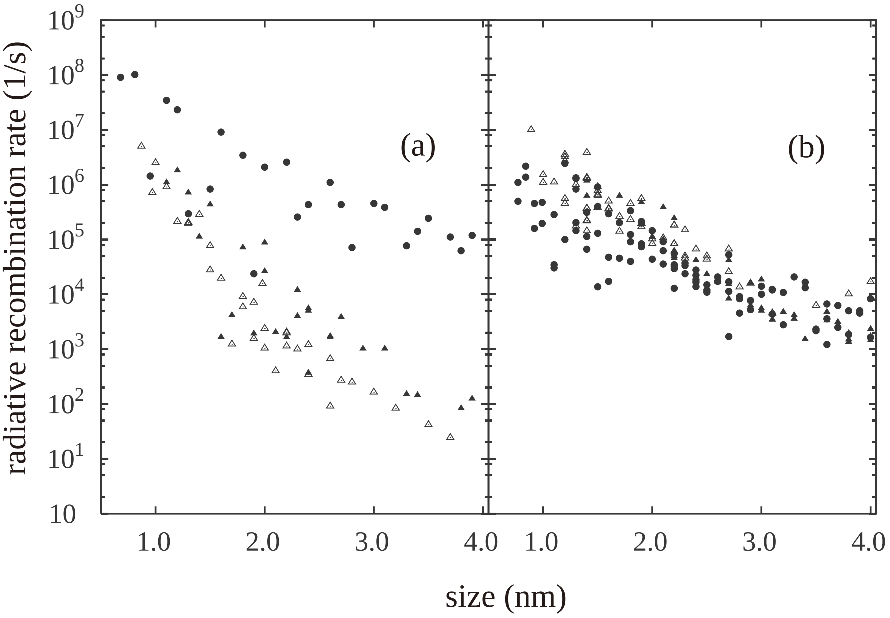

Figure 4.15: Thermally-averaged radiative recombination rate plotted against the size of the system. Each of the figures presents comparison among the three different dimensions which belong to the same model: (a) 'high-symmetry' model and (b) 'low-symmetry' model Si nanostructures. The filled triangles represent the results for 0D systems, the open triangles represent the results for 1D systems, and the filled circles represent the results for 2D systems.

previous works, and also with the discussions given in the previous section. As the size of the nanostructure decreases, the ratio of the *s*-like property in the wave function at or near the band edges (which is zero for bulk Si) increases, which leads to an enhancement of the oscillator strength.

We now give a more detailed description of our results.

Figures 4.14 (a) and (b) show the results obtained for 0D and 1D Si nanostructures, respectively. From these figures, we find that in zero- and one-dimension, the radiative recombination rate is higher for 'low-symmetry' model systems, where the atomic configurations have no point-group symmetries. This result is understood in terms of the breaking of the selection rule, as discussed in Sec. 6.3. Because the atomic configurations are non-symmetric, contributions other than *s*-*p* orbital pairs arise in the summation of eq. (2.16), which leads to an enhancement of the oscillator strength near the band-edge, and hence an enhancement of $\langle \frac{1}{\tau} \rangle$.

On the other hand, from Fig. 4.14 (c), we find that in the case of 2D systems, the situation is reversed. The radiative recombination rate is much higher for the 'high-symmetry' model. This abnormal behavior of the radiative recombination rate seems, at first sight, inconsistent with the case in zero- and one-dimension, but can be understood in terms of the phases of the wave functions in 2D systems.

Firstly, the value of the oscillator strength is governed by the summation in eq. (2.16). For systems with low symmetries, the summation results in a large value, because in this case contributions other than *s*-*p* pair arise. However, the oscillator strength can have an even larger value if, for some reason, most or all the products of the coefficients for the wave functions in eq. (2.16) have the same signs, which is the case for 2D systems.

Now we describe why the terms in eq. (2.16) all have the same signs for the case of 'high-symmetry' model of 2D systems. From the effective-mass equation, the wave function for this system can be approximately written as [31]:

$$\phi(z) = \frac{2}{L_z} \cos\left(\frac{n_z \pi z}{L_z}\right) \tag{4.1}$$

where ϕ is the wave function, z represents the position, L_z is the width of the film, and n_z are non-zero integers.

An example of s and p_x wave function pair which gives the abnormally large oscillator strength is shown in Fig. 4.16. The behavior of the wave function is consistent with eq. (4.1); the wave function is oscillating one-dimensionally. We note that the phases of the s and p_x wave functions are opposite to each other for *all atoms*. This special pair of wave functions emerge only for 'high-symmetry' model in two-dimension, whose wave functions can be written in the form of eq. (4.1). From this s-p_x pair, every nearest-neighbor terms in the summation of eq. (2.16) have the same sign, and consequently, the oscillator strength for this pair of levels becomes abnormally high.

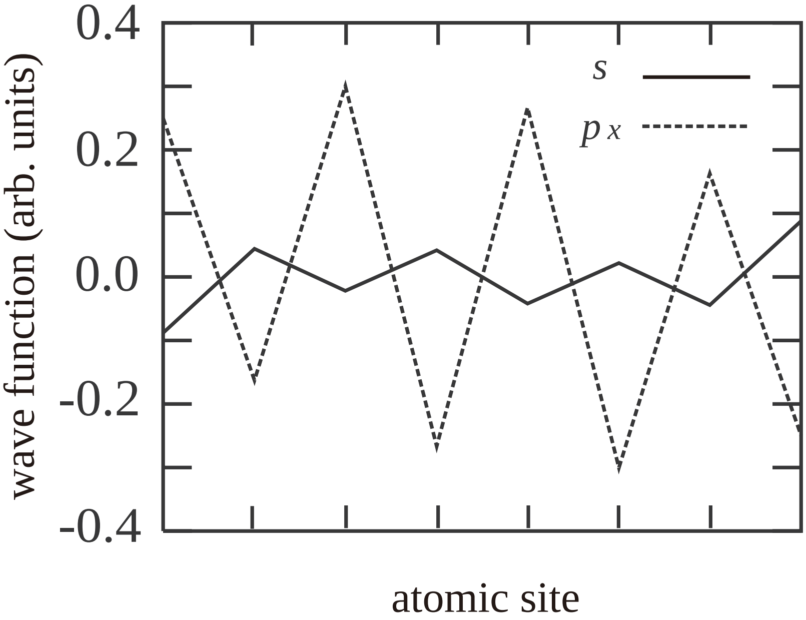

Figure 4.16: Coefficient of the s and p_x wave functions for 'high-symmetry', 2D Si nanostructures. The vertical axis represents the value of the coefficients, while the horizontal axis represents different atomic sites along the direction perpendicular to the surface (the [001] direction).

Each of Figs. 4.15 (a) and (b) shows the radiative recombination rates compared among the three different dimensions. From Fig. 4.15 (a), we find that for 'high-symmetry' model structures, 2D nanostructures have the highest recombination rate, while from Fig. 4.15 (b), we find that for 'low-symmetry' model structures, the rates have comparable values in all dimensions. From both Figs. 4.14 and 4.15, we observe that the case of 2D systems differ greatly from the case of 0D and 1D systems.

From the results obtained in this section, we conclude that the thermally-averaged radiative recombination rate $\langle \frac{1}{\tau} \rangle$ (1) increases as the system size decreases, (2) is larger for 'low-symmetry' model systems in zero- and one-dimension, (3) is larger for 'high-symmetry' model systems in two-dimension, and (4) shows the largest value for 'high-symmetry' model in two-dimension. These results demonstrate that radiative recombination rates for Si nanostructures show different behavior on changes in structural properties, such as ***sizes***, ***symmetries***, and ***dimensions***. As a consequence, we assert that, in order to fabricate functional devices, it is important to control these properties according to the results obtained in this work.

4.5 Conclusions for this chapter

In this chapter, we calculate properties such as band structure, radiative recombination time and the imaginary part of the dielectric function for high-symmetry and low-symmetry silicon nanostructures in zero, one, and two dimensions. We find that our new model with low symmetry has optical properties which considerably differ from previous models with high symmetry, and further that for one-dimensional system, this difference accounts for the discrepancy in radiative recombination time previously reported between theoretical calculations and experiments. In other words, we have succeeded in describing the behavior of the so-called 'S' band.

We observe that properties which depend on the overall electronic structure, such as band structure and the full ε_2, is practically unaffected by the change in symmetry. On the other hand, we find that properties which depend on the electronic structure near the band edge, such as the band gap, the thermally-averaged radiative recombination time, and ε_2 near the band edge, change considerably when symmetry of model systems is varied. The band gap is slightly blue-shifted because of the change in the effective coordination number, and the oscillator strength near or at the band edge is greatly enhanced because of the change in symmetry of the atomic configurations and wave functions of the quantum wire unit cell, which leads to relaxation of selection rules for angular momenta.

We note that we did not incorporate excitonic effects into our calculations, whose importance was pointed out in ref. 68. Excitonic effects can enhance the oscillator strength by about a factor of two. However, this applies for both the low and high symmetry wires, and our assertions that the difference in symmetry greatly changes the behavior of the oscillator strength, and that this difference accounts for the discrepancy previously observed between theory and experiments, are unchanged.

We further calculate the case of zero-dimensional and two-dimensional Si nanostructures. For the optical band gap E_{g}, we find that it increases as the size and dimension of the system decrease. For the radiative recombination rate, $\left\langle \frac{1}{\tau} \right\rangle$, we observe that in 0D and 1D, it is larger for 'low-symmetry' model systems, while in 2D, it is larger for 'high-symmetry' model systems. Our results are interpreted by a simple argument based on the effective mass approximation.

From our calculations, we conclude that, for the purpose of understanding the PL from Si in detail, it is necessary to incorporate point-group symmetry properties explicitly into the model for atomic configurations.

Chapter 5

Silicon nanostructure with local disorders

5.1 Introduction for this chapter

According to ref. 20, it is possible to classify the observed luminescence from nanostructured Si into four categories in order of wave length; (1) the near-infrared luminescence, (2) the near-infrared-green 'S' (slow) band luminescence, (3) the green-blue 'F' (fast) band luminescence, and (4) the ultra violet luminescence.

Out of the four types of luminescence listed above, the most well-studied is the 'S' band luminescence. The 'F' band luminescence has also been studied with great interests, though not as extensively as the 'S' band luminescence. The near-infrared and ultra violet luminescence have been studied less frequently, and in any case they are not of our interest in these series of our work which aim theoretical elucidation of nanostructured Si as a possible device of visible luminescence. From this view point, we are concerned only with luminescence in the aforementioned categories (2) and (3).

It has been confirmed from experiments that the so-called 'S' band luminescence is observed in porous or nanocrystalline Si samples which are relatively well-passivated, while the so-called 'F' band luminescence is achieved when π-Si is thermally-oxidized [54].

Experimental studies have revealed the essential aspects for the 'S' and 'F' bands as follows.

As for the 'S' band [20, 54], (a) the optical band gap is blue-shifted from bulk Si, the blue-shift being larger for the smaller nanostructures, (b) the luminescence spectrum is broad, with a tunable peak over a wide range of energy (from 1.4 eV up to 2.2 eV, or even higher), (c) the spectral decay time is in the order of microseconds at room temperature, and (d) the spectral decay time is dependent on luminescence energy, the higher-energy luminescence having the shorter decay time.

As for the 'F' band, on the other hand, some aspects of the spectral characteristics are totally different from those for the 'S' band luminescence, as described in the following [20, 54, 76]; (a) the optical band gap is blue-shifted from bulk Si, (b) the luminescence spectrum ranges from about 1.8 eV to about 3.2 eV with a peak at around 2.6 eV, (c) the spectral decay time is very fast being of the order of nanoseconds, (d) the spectral decay time is independent of the luminescence energy.

Canham in his pioneering study proposed that the origin of the 'S' band luminescence lies in the size itself of Si quantum wires, whose band gap and radiative efficiency are governed by the quantum confinement (QC) effect for nanometer-sized materials [17]. Following this original proposal, quite a number of experimental and theoretical studies have been performed in order to confirm the validity of this statement [54].

In the previous chapter, we have introduced a new structural model devoid of point-group symmetries for Si quantum wires. We have shown that our model yields radiative recombination time which agrees remarkably well with experimental results for the 'S' band luminescence. This is in contrast to previous studies, which failed to show such beautiful agreement [29, 30, 54]. The atomic configurations in our model have lower symmetry than the previously-studied models, the latter having high point-group symmetries in the atomic configurations. We have shown that the oscillator strength near the band edge, and hence the radiative recombination time, change considerably when the symmetry of a Si nanostructure is changed. Because it is unlikely that realistic nanostructures have high point-group symmetries, we asserted that our model is a more realistic model for the 'S' band luminescence.

On the other hand, the spectral characteristics for the 'F' band luminescence cannot be explained even by our model of chapter 4. Nor can they be explained by the models put forward by other workers. Above all, the previous models [29, 30, 54] (1) can realize a decay time in the order of nanoseconds only in the energy region of band gaps larger than 4.0 eV, and (2) give the decay time clearly dependent on the energy of the luminescence. Neither of these features are found in the ‘F’ band luminescence.

In the work described in chapter 4 which successfully accounts for the characteristics of the ‘S’ band luminescence, we have studied model structures lacking point-group symmetry alone. This means that, in our previous model, the local order in atomic configurations is preserved; *i.e.*, the bond-length and bond-angles are kept fixed. This is a good assumption for the ‘S’ band luminescence, because crystallinity is known to be preserved even for very small nanostructures in the case of the ‘S’ band luminescence [20]. However, this may not be a good assumption for the ‘F’ band luminescence, because, as pointed out in ref. 76, samples for the ‘F’ band luminescence contain small Si clusters with sizes smaller than 1 nm, and more importantly, with inhomogeneous pressures acting on their surfaces. This situation leads to considerable structural relaxation at near-surface regions. In this situation, our model for the ‘S’ band is no longer valid, and we must study nanostructures with locally-disordered atomic configurations.

Therefore, it is our purpose of the present chapter to study electronic and optical properties of Si nanostructures with local disorders, in order to elucidate the origin of the observed ‘F’ band luminescence. For the sake of comparison, let us note that, in the work of chapter 4, we studied nanostructures with low point-group symmetry and high local order. It is interesting to see how the different degrees of disorder incorporated into the model would change the electronic and optical properties of nanostructures.

The rest of the chapter will be organized as follows. In section 5.2, our model and calculational method is presented. In particular, we introduce a new model, in which structural relaxation of nanostructures with perfect and imperfect passivation is taken into account. Then in section 5.3, our results are given. Emphasis is put upon the comparison between the two models we introduce. Finally, in section 5.4, we give some conclusions for the present chapter.

5.2 Model and calculational method

As mentioned in the previous section, we perform electronic state calculations for Si clusters with local disorder as well as low point-group symmetry. For this purpose, we start with nanostructures with local order, and calculate structural relaxation for these structures under various conditions. Structural relaxation has been calculated in the past for square and rectangular Si quantum wires [29, 69, 77]. It was concluded that, for Si wires with symmetric unit cell and perfect passivation at the surface, the effects of structural relaxation are minimal [29, 69, 77]. This may not be the case for the model introduced in the previous chapter, whose unit cell is shown in Figs. 4.1 (b), (d), and (f). For this reason, we first study structural relaxation for the model structure shown in Fig. 4.1 to check its stability. Atomic configurations made in this fashion will hereafter be referred to as 'well-passivated'.

In refs. 29, 69, 77 the atomic configurations were stable because the surface dangling bonds were perfectly passivated by hydrogen. This may not be the case for the 'F' band samples. For this reason, we calculate structural relaxation for Si clusters with poor passivation. This prompts a large structural relaxation at near-surface regions. Atomic configurations made by this scheme will hereafter be referred to as 'poorly-passivated'.

The atomic configurations for the 'poorly-passivated' model are made by the following procedures:

1. by removing some hydrogen atoms from the surface region, construct arbitrary number of dangling bonds in Si clusters with perfect passivation and with sizes of about 1 nm, but no point-group symmetry,
2. allow structural relaxation to take place from the above structure of 1.,
3. re-passivate the dangling bonds by hydrogen atoms,
4. allow structural relaxation to take place from the structure of 3.

By following the above-described procedures, we obtain model structures with atomic configurations in local minima in the energy landscape. This kind of local minima is normally unreachable from the well-passivated model. It is expected that model structures obtained in this way have local disorders such as distribution of bond-lengths and bond-angles. Consequently, atomic configurations thus obtained simulate well the essential aspects of the samples for the 'F' band luminescence.

Calculations for the well-passivated model will be performed for one-dimensional quantum wires, while calculations for the poorly-passivated model will be performed for zero-dimensional Si clusters. The essence of the results is insensitive to the spatial dimension of the nanostructure.

The calculations are performed by the tight-binding method. The tight-binding model we use is the nearest-neighbor, two-center, $sp^3s^*d^5$ scheme reported by Jancu *et al.* [39]. Structural relaxation is evaluated by the simple tight-binding total energy method described in chapter 2. We calculate the optical band gap, E_{g}, and the thermally-averaged radiative recombination rate, $\left\langle \frac{1}{\tau} \right\rangle$, and compare the results obtained from the two models.

5.3 Results and discussions

5.3.1 results for the 'well-passivated' model

In this subsection, results for the 'well-passivated' model described in section 5.2 are presented. This model is very similar to the one examined in the previous chapter; the difference is that structural relaxation is taken into account.

In Fig. 5.1, examples of the relaxed and unrelaxed structures are shown. From Fig. 5.1, we see that the effects of relaxation for the core region is negligibly small, while it is appreciable near the surface. The largest relaxation we obtained in this scheme is in the order of several percent in terms of atomic positions.

In Fig. 5.2, we show the results of the thermally-averaged radiative recombination time $\langle \tau \rangle$ plotted against luminescence energy E_{PL}. From Fig. 5.2, we see that there is no substantial difference for $\langle \tau \rangle$ between the relaxed and unrelaxed structures.

From the two results shown in Fig. 5.2, we conclude that well-passivated Si quantum wires are stable against structural relaxation. It is worth noting here that, in previous studies, atomic configurations with high point-group symmetries are also shown to be stable against structural relaxation if the passivation is complete [54, 69, 77]. This indicates that, as long as a system is well-passivated, the effect of structural relaxation is practically very small, whether the point-group symmetry is high or low in the atomic configuration of the system.

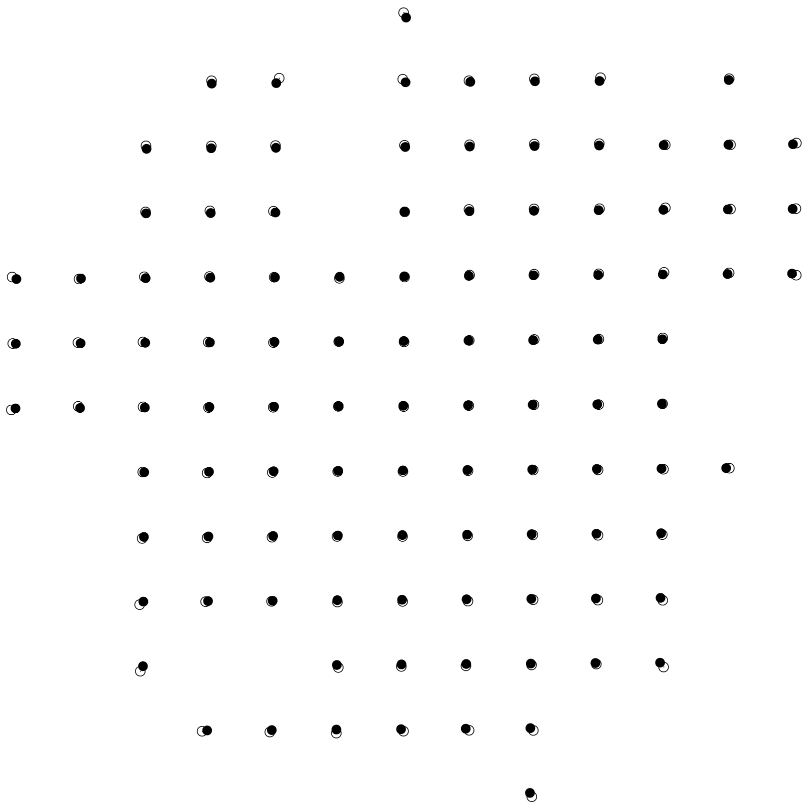

Figure 5.1: An example of a structural relaxation for the well-passivated model. The filled circles represent unrelaxed Si atoms, while the open circles represent relaxed Si atoms. The hydrogen atoms are not shown.

5.3.2 results for the 'poorly-passivated' model

In this subsection, we present results for the 'poorly-passivated' model described in section 5.2. In this model, structural relaxation mainly takes place in the vicinities of dangling bonds. Therefore, considerable amount of relaxation occurs at near-surface regions. An example of the relaxed atomic configuration is shown in Fig. 5.3. when compared to Fig. 5.1, large structural relaxation is observed for near-surface regions. The unrelaxed structures have local order, while the relaxed structures have no local order. It is very likely that electronic and optical properties differ considerably between these two cases.

In Fig. 5.4, the relation between the number of Si atoms in a certain cluster and its band gap E_g is shown. Figure. 5.4 (a) shows the results for the unrelaxed clusters, while Fig. 5.4 (b) shows the results for the relaxed clusters. It can be seen that the band gap is largely red-shifted for the structures with local disorder. The degree of the red-shift is larger than the blue-shift invoked by the quantum confinement effect, and E_g for the relaxed clusters are

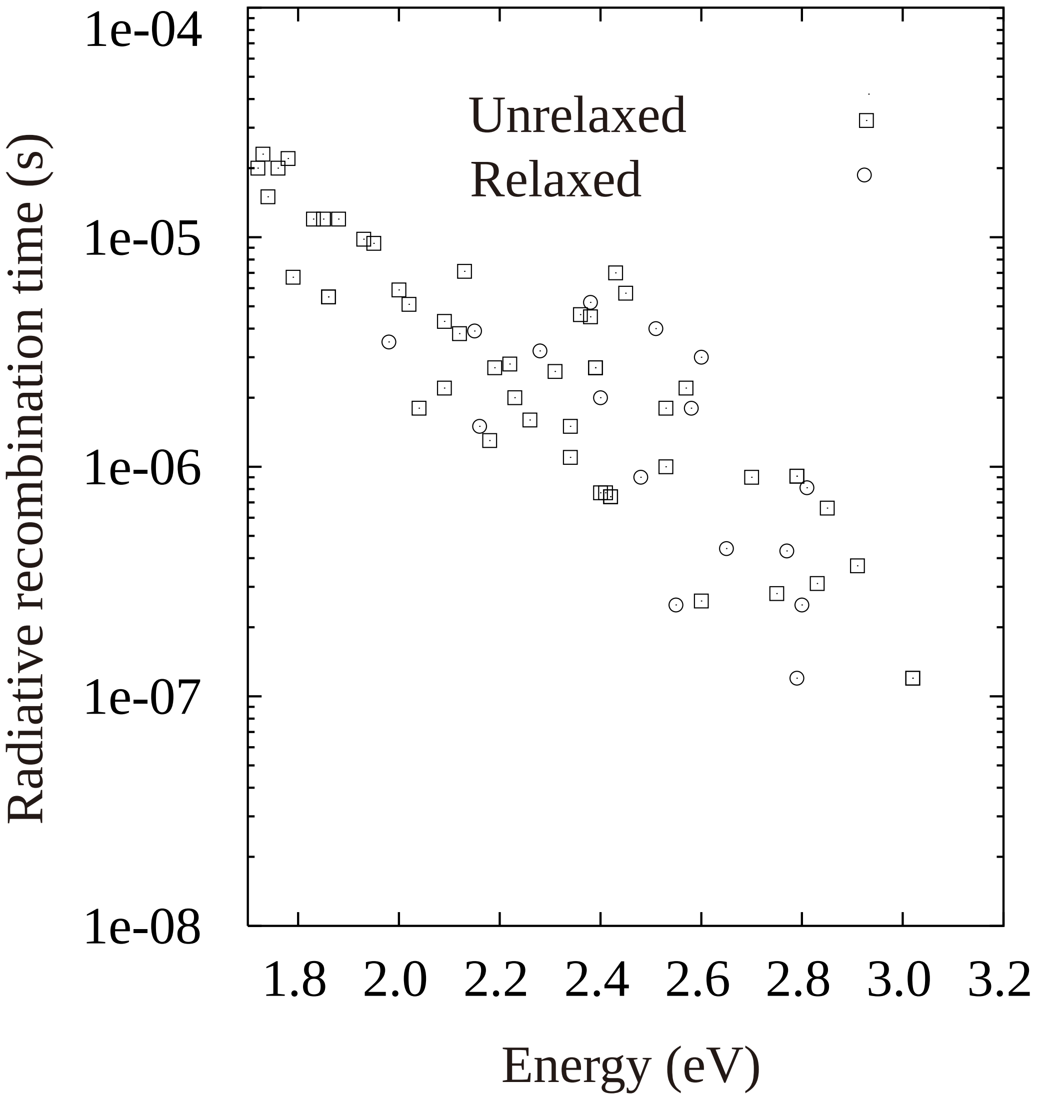

Figure 5.2: The relation between luminescence energy E_{PL} and the radiative recombination time for the relaxed and unrelaxed quantum wire.

independent of size.

Because of the local disorder, the band width is broadened, which results in the red-shift of E_{g}. The degree of the red-shift depends on the degree of disorder for the Si-Si and Si-H bonds, which differs from system to system. Furthermore, the changes in band gap induced by local disorder is much larger than the changes induced by the quantum confinement effect. For this reason, the band gap becomes independent of the system size. In other words, the system size, defined by the number of Si atoms in the system, is no longer a good measure for the characterization of that cluster. We must count in not only the number of atoms but also the degree of local disorder, the degree of asymmetry and the surface-volume ratio.

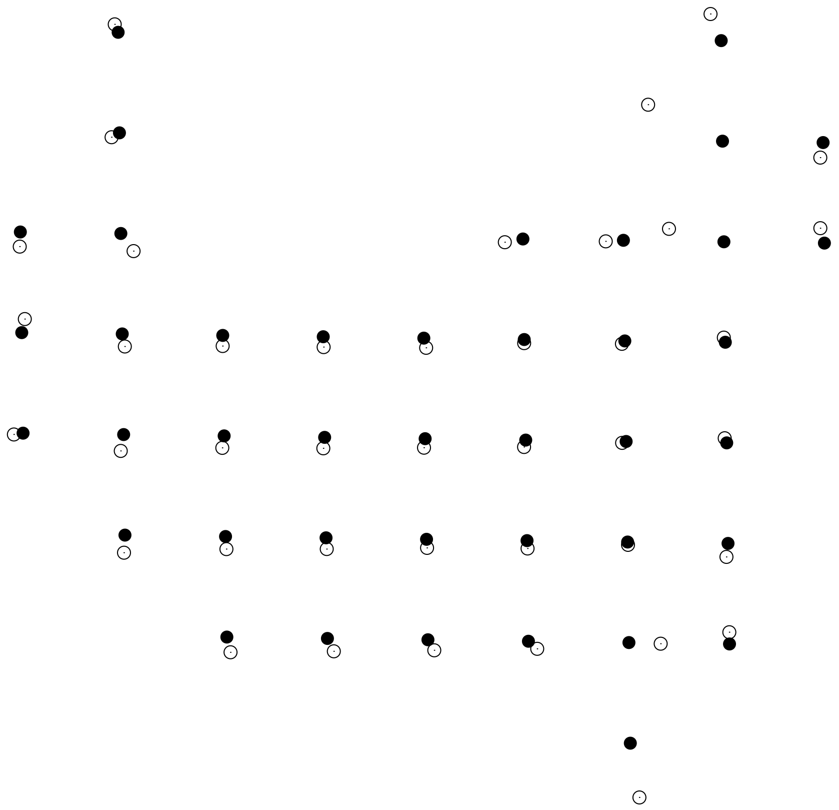

Figure 5.3: An example of a structural relaxation for the poorly-passivated model. The filled circles represent unrelaxed Si atoms, while the open circles represent relaxed Si atoms. The hydrogen atoms are not shown.

In Fig. 5.5, the thermally-averaged radiative recombination time is plotted as a function of E_{PL}. Results for both the relaxed and unrelaxed clusters are shown. We see from Fig. 5.5 that, for clusters with local disorder,

1. the luminescence energy is in the range of 1.8 eV to 3.2 eV,

2. the radiative recombination time is in the order of 10^{-9} s to 10^{-7} s, and

3. the radiative recombination time is independent of energy.

These features are in contrast with the features of clusters with local order, which are stated as follows;

1. the radiative recombination time is in the order of 10^{-7} s to 10^{-5} s, and

2. the radiative recombination time is dependent on E_{PL}; the lower the energy, the longer the recombination time.

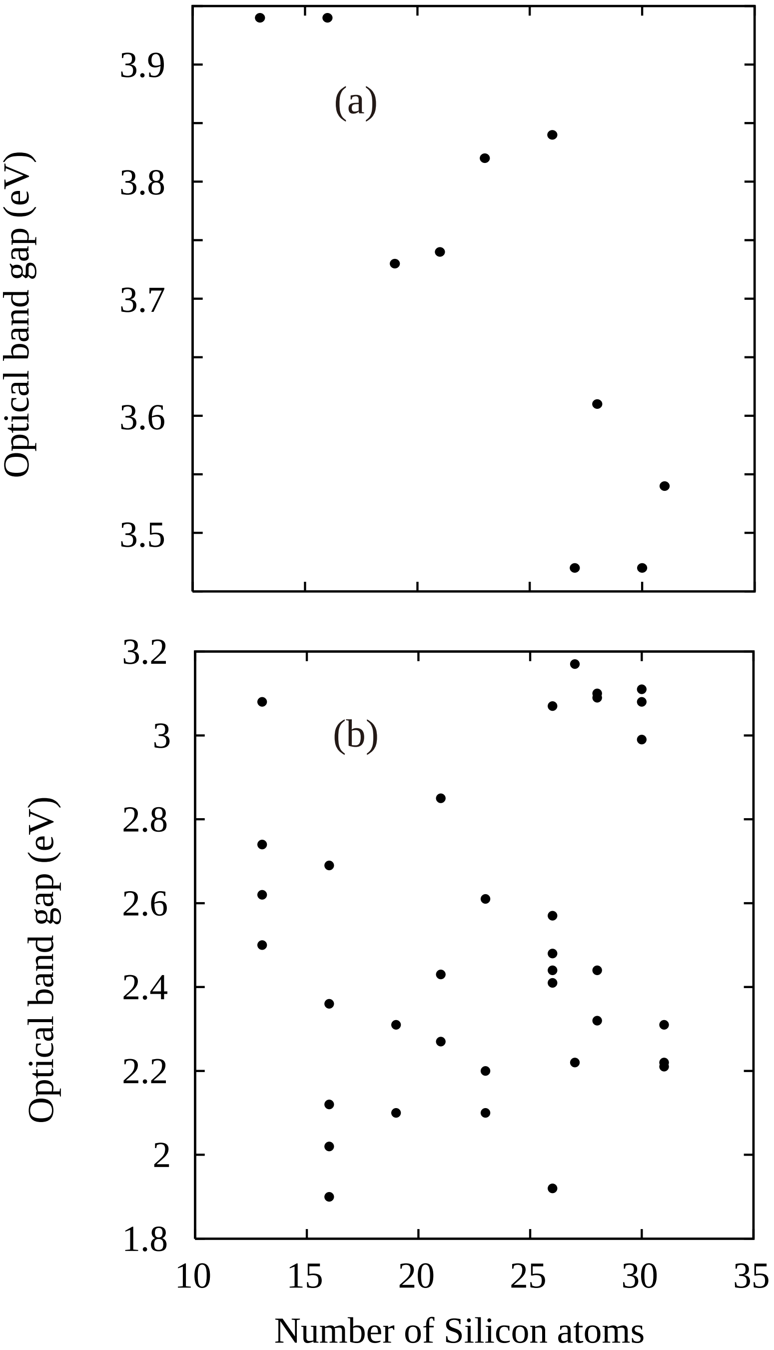

Figure 5.4: The relation between band gap E_g and the number of Si atoms, for the structures (a) without local disorder and (b) with local disorder.

The results obtained for cluster with local disorder are consistent with the main features of the experimental results for the 'F' band luminescence, *i.e.*, for Si clusters with diameter of 1 nm or less,

1. the luminescence energy ranges from 1.8 eV to 3.2 eV,

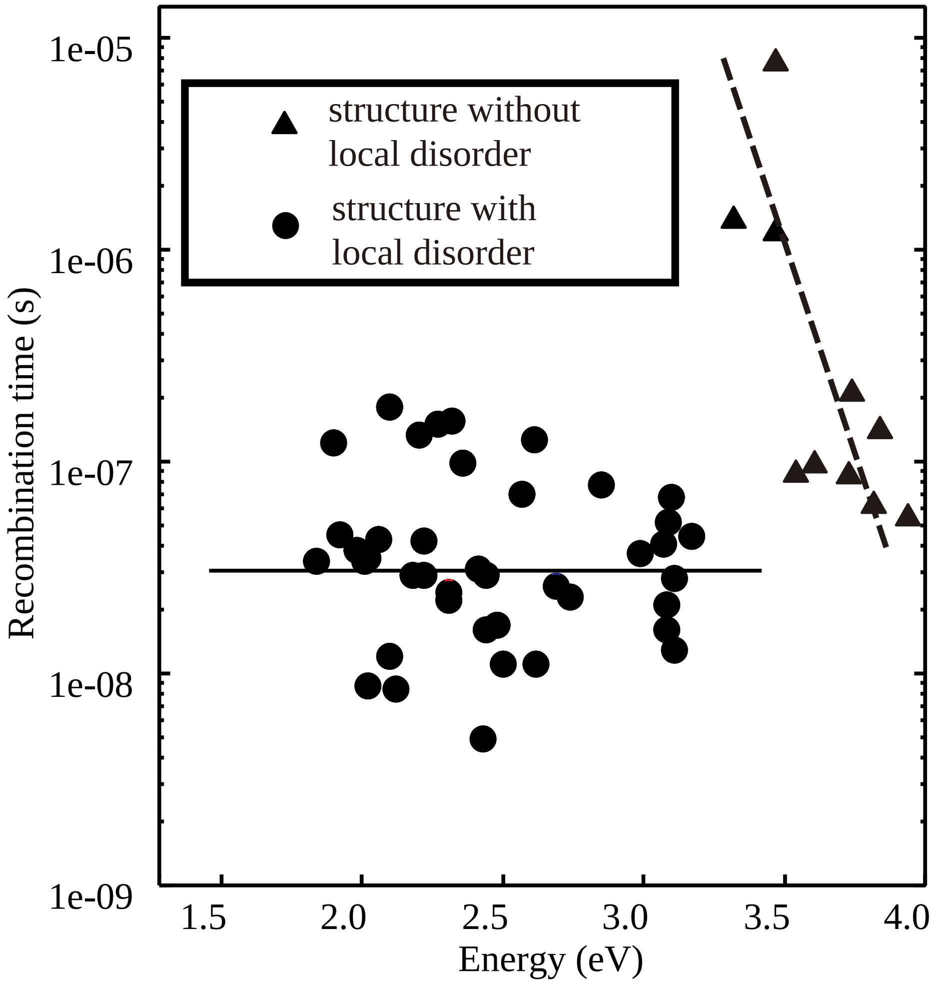

Figure 5.5: The relation between the luminescence energy E_{PL} and the thermally-averaged radiative recombination time $\langle\tau\rangle$. The filled triangles represent results for structrures without local disorder, while the filled circles represent results for structures with local disorder. The solid and dashed lines are guides for the eyes.

2. the decay time is in the order of 10^{-9} s to 10^{-8} s,

3. the decay time is independent of the luminescence energy.

These experimental results contradict with calculations on model structures which does not include local disorder, and we assert that local disorder is the key factor in the ‘F’ band luminescence.

Now let us give some comments concerning the results obtained here. At near-surface region, the atomic configuration is highly disordered, which leads to a large increase in the oscillator strength at this region. Since the degree of disorder is larger than in the case of the model introduced in chapter 4, the increase of the oscillator strength is expected to be larger. It is possible to investigate this point from the comparison of Fig. 5.5, which show that the radiative recombination time for the structure with local disorder is considerably shorter than for the structure without local disorder. Another point is that the degree of disorder differs from system to system, which leads to a large distribution for the osillator strength. Finally, the emission energy is independent of system size, ranging from 1.8 eV to 3.2 eV. These situations lead to radiative recombination time independent of the system size, with a relatively short value of 10^{-9} s to 10^{-7} s. It is not possible to obtain this result for nanostructures with local order, in which case the emission energy and oscillator strength depend largely on system size.

The structural characteristic of the locally-disordered model is also consistent with experiments, because as pointed out in ref. 76, samples showing the 'F' band luminescence contain small Si clusters with characteristic sizes of 1 nm or less, with inhomogeneous pressures acting on their surfaces. In this situation, small Si clusters with locally-disordered surfaces are made.

We note here that our calculations may be open to argument from a *quantitative* point of view, because we did not include various many-body effects, such as excitonic effects, which may contribute considerably to the oscillator strength. However, our calculations include the most essential effect, namely the dipole matrix element, and accordingly our conclusion that local disorder is the key factor in understanding the 'F' band luminescence is intact from a *qualitative* point of view.

A schematic drawing of the sample for the 'F' band luminescence is shown in Fig. 5.6. The sample consists of mostly oxidized Si, whose band gap will be much larger than that of visible light, with very small Si clusters embedded in it. In such a situation, photogeneration of the carriers will occur at the oxide region, followed by a relaxation of the carriers to the region where the energy is lower, *i.e.*, to the locally-disordered Si clusters. Then, the carriers recombine at the Si clusters to give the 'F' band luminescence, which is in the visible region. The schematic picture given above can well account for the essential features of the 'F' band luminescence, and is also consistent with the results of our calculations.

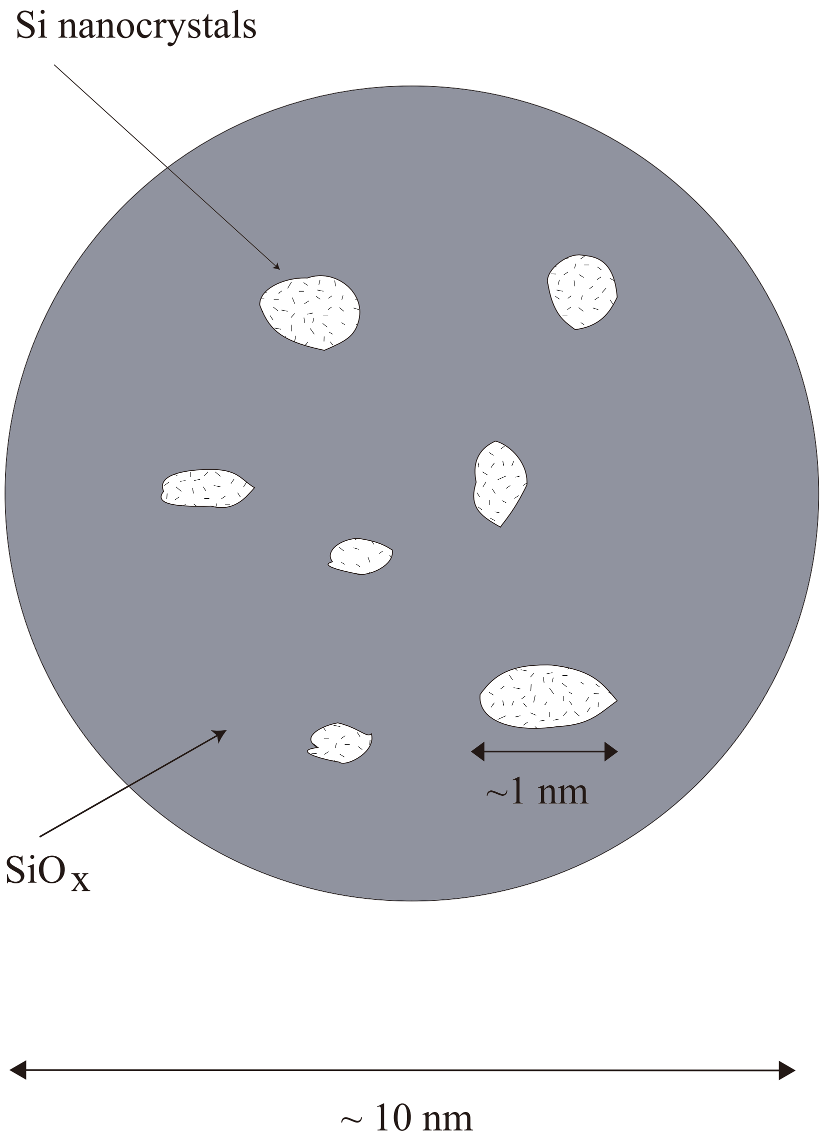

Figure 5.6: A schematic figure for thermally-oxidized porous Si. Small Si clusters with disordered surfaces are embedded in a relatively large oxide region.

5.4 Conclusions for this chapter

In the present chapter, we calculate electronic states and radiative recombination time for Si nanostructures with disordered surfaces. We find that, for Si clusters with characteristic sizes of 1 nm and disorder at the surface region, the radiative recombination time is independent of the luminescence energy, and is in the order of 10^{-9} s to 10^{-7} s. These results are consistent with the experimental results for the so-called ‘F’ band luminescence, and cannot be obtained from calculations based on a simple quantum confinement hypothesis. From our calculations, we conclude that the effects of local disorder in atomic configurations are the essential factor for the appearance of the ‘F’ band luminescence. Finally, let us state that, from the present and previous chapters, we successfully obtain a unified view on the mechanism of ‘S’ and ‘F’ band luminescence by introducing new structural models for Si nanostructures.

Chapter 6

Static and dynamical structure of liquid germanium at high density

6.1 Introduction for this chapter

Germanium (Ge) is a diamond-structure semiconductor in the solid phase, and becomes metallic upon melting [21]. Contrary to the cases of ordinary solid-liquid phase transitions, the transition in Ge is accompanied by an *increase* in the density, with significant structural changes.

Concerning atomic structures in the liquid phase, Ge under atmospheric pressure is known to have several features which are unusual when compared to ordinary simple liquids [21]. These features cannot be accounted for in the framework of the isotropic pair-potential models, which have been commonly used to describe the structures of simple liquids [78]. This fact has prompted much experimental [79–82] and simulational [83–86] studies. To list some of the findings, in particular in comparison with the properties of simple liquids; (1) the static structure factor $S(Q)$ has a distinct shoulder on the immediate right-hand side of the first peak, (2) the first peak of $S(Q)$ has a relatively small value, (3) the first peak of the pair distribution function $g(r)$ also has a relatively small value, (4) the coordination number N_c is considerably lower than N_c found in simple liquids, (5) the dip between the first and second peaks of $g(r)$ is quite shallow, and (6) the ratios of the positions of the first and second peaks of $S(Q)$ and $g(r)$ have much higher values than those for a hard-sphere liquid.

The structural features listed above have been understood as evidence that solid-like local structures persist in the liquid state for Ge [21, 87]. Unlike simple liquids, both covalent-like and metallic-like bonds are expected to exist in liquid Ge (ℓ-Ge). The competition between the two different types of bondings determines the complex local structures of ℓ-Ge. In refs. [81] and [86], it was shown that a '*disordered*' β-Sn type model, in which the structure of ℓ-Ge is characterized as β-Sn structure with disorders in bond lengths and bond angles, can well account for the essential structural features found in ℓ-Ge.

The structural properties of ℓ-Ge at atmospheric pressure have been extensively studied, as described in the above. What is not fully elucidated yet is the behavior of ℓ-Ge under pressure. When pressure is applied to ℓ-Ge, we expect that it will shrink non-uniformally. This observation is based on the following reasons: (1) the contraction of the bonds due to pressure is expected to be anisotropic because of the anisotropic nature of covalent bonds, and (2) the bonding property is anticipated to become more metallic than covalent when pressure is applied. From the above arguments, we expect that ℓ-Ge shrinks by changing its local structure when pressure is increased.

In order to clarify the above point, high-pressure experiments (up to 25.0 GPa) were performed recently [88]. The results of the experiments imply that the local structure of ℓ-Ge does indeed change in the following manner when pressure is applied [88]. In the low-pressure region, the local structure of ℓ-Ge is characterized as a '*disordered*' β-Sn type structure, a structure having a wide distribution of bond angles with essentially tetrahedral bonding of the β-Sn type, while in the high-pressure region, the local structure is characterized by a '*pure*' β-Sn structure, a structure having a narrow distribution of bond angles with peaks at characteristic angles of the β-Sn structure.

Experimental studies, however, give an understanding of the local structure in liquids only to a certain extent, because all the information obtained from experiments is limited to the one-dimensional representation projected from and averaged over the real three-dimensional atomic configurations. This is where the importance of simulational studies enters that play roles complementary to experimental studies, so that the understanding of atomic configurations in liquids is achieved in full detail. From this view point, we perform tight-binding (TB) molecular dynamics (MD) simulations on ℓ-Ge at seven different densities. We calculate $g(r)$ and $S(Q)$, and compare them with results obtained from experiments. We further study the bond-angle distribution function $g^{(3)}(r_c, \theta)$, and deduce the change in the local structure of ℓ-Ge under pressure.

The rest of the present chapter will be organized as follows. In section 6.2, our TBMD method and simulation procedure used in this work are described in detail. In section 6.3, the results obtained from our simulations, along with discussions, are presented, with special emphasis on the change in local structure of ℓ-Ge with increase of the density. Finally, in section 6.4, we draw some conclusions for the present chapter.

6.2 Simulation method

6.2.1 non-orthogonal tight-binding scheme

As mentioned in section 6.1, we perform TBMD simulations for ℓ-Ge. Since we are interested in the structure of ℓ-Ge at various densities, we need a transferable TB scheme which can accurately reproduce both the low- and high-pressure forms of Ge. This is a demanding task, since the bonding nature of Ge changes from covalent-like to metallic-like when compressed. In recent researches, it has been clarified that one way to construct such a transferable scheme, within the framework of the TB picture, is to explicitly incorporate the non-orthogonality of the atomic wave functions [50]. This procedure makes the TB model dependent on the environment of each atom, and the TB model thus obtained can accurately describe the very different bonding nature of the low-density and high-density liquids.

The TB model we use is based on the TB model described in ref. 89. This TB model includes the non-orthogonality of the wave functions in a natural way. In ref. 89, the cluster geometry of Ge was investigated, which gave good agreement with available experiments and *ab initio* MD simulations [89]. However, we found that, when applied to ℓ-Ge, the original scheme presented in ref. 89 gives inaccurate results; in particular, the high-pressure form could not be simulated accurately [90]. We therefore modify this scheme so that it is more appropriate for our simulations.

In the following, we first describe the original scheme presented in ref. 89. Then we describe the modifications we apply to this scheme.

In the original scheme, the total energy E_{tot} of the system under consideration is written in the usual fashion as follows:

$$E_{\mathrm{tot}} = E_{\mathrm{BS}} + E_{\mathrm{rep}} + E_0. \tag{6.1}$$

The first term, E_{BS}, is the band-structure energy, and is the sum of the one-electron energies $\{\varepsilon_n\}$: $E_{\mathrm{BS}} = \sum_n \varepsilon_n$, where the sum over n is taken for all occupied states. Note that in this chapter, we simply add ε_n for all occupied states, which corresponds to zero electron temperature. The second term is a repulsive term, and physically describes the repulsions of the ions and the corrections to the double counting in the band-structure energy. This term is assumed to be written in terms of pair potentials: $E_{\mathrm{rep}} = \sum_{i<j} \phi(r_{i,j})$, where $r_{i,j}$ denotes the distance between atoms i and j. The pair potential $\phi(r_{i,j})$ is written in the following form:

$$\phi(r) = \phi_0 \mathrm{e}^{-\beta(r-d_0)}, \tag{6.2}$$

where ϕ_0 and β are fitting parameters, and d_0 is the nearest-neighbor distance in diamond-structure solid at 0 K (in the case of Ge, 2.44 Å). The third term, E_0, is a constant term. This term will only shift the zero of the energy, and will not be taken into account explicitly.

The one-electron energy necessary for the evaluation of the band-structure energy is calculated from the non-orthogonal TB (NTB) method described in chapters 2 and 3. The basis set is the minimal sp^3 set. The force from E_{BS} is calculated from the Hellmann-Feynman theorem. Note that force coming from E_{rep} is easily calculated by differentiating eq. (6.2).

Now the problem is reduced to determining the Hamiltonian and overlap matrices from atomic positions. This is performed by modifying the scheme originally formulated by van Schilfgaarde and Harrison [91].

According to van Shilfgaarde and Harrison, the Hamiltonian matrix elements, for two atoms with distance r apart, in the NTB scheme is described in terms of the Hamiltonian matrix elements in the *orthogonal* TB (OTB) scheme, by the following equation:

$$H_{\lambda\lambda'\mu}(r) = V_{\lambda\lambda'\mu}(r) \left(1 + \frac{1}{K} - S_2^2\right). \tag{6.3}$$

Here, $H_{\lambda\lambda'\mu}(r)$ denotes the Hamiltonian matrix elements in the NTB scheme, $V_{\lambda\lambda'\mu}(r)$ denotes the Hamiltonian matrix elements in the OTB scheme, $\lambda\lambda'\mu$ denotes combinations of angular and magnetic quantum numbers of the atomic wave functions for the two atoms under consideration, for example, $sp\sigma$, S_2 is the 'non-orthogonality between sp^3 hybrids', defined as $S_2 = \frac{S_{ss\sigma} - 2\sqrt{3}S_{sp\sigma} - 3S_{pp\sigma}}{4}$, where $S_{ss\sigma}, S_{sp\sigma}$, and $S_{pp\sigma}$ are overlap matrix elements, and finally K is an empirical parameter being assumed to have the following distance dependence:

$$K(r) = K_0 \mathrm{e}^{\sigma(r-d_0)^2}, \tag{6.4}$$

where σ and K_0 are fitting parameters.

The overlap matrix elements $S_{\lambda\lambda'\mu}$ is also written in terms of the Hamiltonian matrix elements in the OTB scheme. This is carried out in the spirit of the extended Hückel theory, *i.e.*, [92]

$$S_{\lambda\lambda'\mu}(r) = \frac{2V_{\lambda\lambda'\mu}(r)}{K(r)(\varepsilon_\lambda + \varepsilon_{\lambda'})}, \tag{6.5}$$

where $S_{\lambda\lambda'\mu}(r)$ is the overlap matrix element and ε_λ is the on-site energy of the atoms.

Finally, the Hamiltonian matrix elements in the OTB scheme is written as follows:

$$V_{\lambda\lambda'\mu}(r) = V_{\lambda\lambda'\mu}\,(d_0)\,\mathrm{e}^{-\alpha(r-d_0)}, \tag{6.6}$$

where α is a fitting parameter, and is related to β as $\alpha = \frac{\beta}{4}$. The term $V_{\lambda\lambda'\mu}(d_0)$ is determined from Harrison's universal parameters [15].

The four fitting parameters, α (or β), ϕ_0, K_0, and σ, are determined so as to reproduce the cohesive energy for the diamond structure of Ge. Once these four parameters are given, we are able to calculate the total energy eq. (6.1) and the force consistent with this energy.

The advantage of the NTB scheme given in the above lies in that it can be constructed in a systematic manner, with a small number (four) of fitting parameters. However, from our previous work [90] we found that, when applied to ℓ-Ge as it is, the properties of the high-pressure liquids cannot be reproduced accurately. In particular, the temperature of melting was found to be too high, for example, about 3000 K at 24.0 GPa, which is much higher than the experimental value of about 1300 K at the corresponding pressure region. This point could not be improved by simply refitting the four fitting parameters, and therefore we modify the original scheme in the following manner.

1. Both the liquid and β-Sn phase of Ge are metallic, and accordingly the information of the conduction band is important. For this reason, we add an extra s^* orbital, following ref. 93. In doing so, we assume that matrix elements $V_{s^*s\sigma}, S_{s^*s\sigma}$, and $S_{s^*p\sigma}$ are zero.

Table 6.1: Parameters for our TB model. All symbols are defined in the text.

ε'_s (eV)	ε'_p (eV)	$\alpha(\mathring{A}^{-1})$	$\beta(\mathring{A}^{-1})$
-14.38	-6.36	-1.25	-3.88
ϕ_0(eV)	K_0	$\sigma_0(\mathring{A}^{-2})$	$d_0(\mathring{A})$
0.66	1.1	1.0	2.44
ε_s (eV)	ε_p (eV)	ε^*_s(eV)	$V_{ss\sigma}(d_0)$ (eV)
-8.38	-0.36	11.64	-1.30
$V_{sp\sigma}(d_0)$ (eV)	$V_{pp\sigma}(d_0)$ (eV)	$V_{pp\pi}(d_0)$ (eV)	$V_{s^*p\sigma}(d_0)$ (eV)
0.95	1.14	-0.329	0.51

2. Hamiltonian matrix elements for the OTB scheme are modified so that the band structure of the solid-diamond phase is reproduced.

3. The term ε_λ, which appears in eq. (6.5), is now assumed to be independent of the on-site energy terms of the Hamiltonian matrix, and is denoted as ε'_λ.

4. Fitting parameters α and β are assumed to be independent of each other.

We carry out the above modifications, and determine the fitting parameters so that the cohesive energies for the diamond and β-Sn structures, the band structure for the solid-diamond phase, and the liquid structure of Ge can be reproduced simultaneously. The parameters thus obtained are shown in table 6.1.

The cohesive energies for the diamond and β-Sn phases of Ge obtained by our modified scheme are shown in Fig. 6.1. As shown in Fig. 6.1, the fact that the cohesive energy versus volume relations achieved from our modified TB scheme are in good agreement with those obtained from *ab initio* calculations strongly confirms the validity of our modified TB scheme in all the volume regions covering both for the diamond and β-Sn structures.

6.2.2 simulational details

Now we list the details of the simulational conditions we adopt in this work. We perform NVT-ensemble MD simulations for ℓ-Ge at seven different densities. The densities adopted are taken from experiments. The number of atoms N is 256.

The initial configuration is constructed from a preliminary simulation in the NVE-ensemble, with 64 Ge atoms in a cubic cell of size 11.3Å × 11.3Å × 11.3Å, corresponding to a diamond-

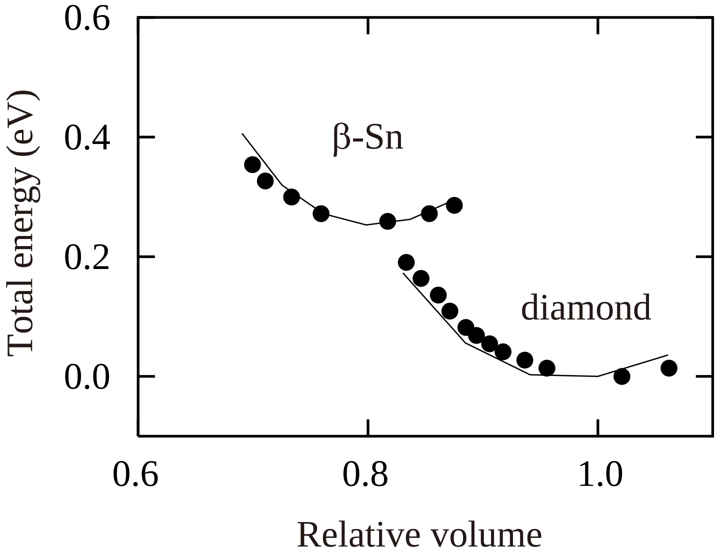

Figure 6.1: Cohesive energy curves for the diamond and β-Sn structures, plotted against volume. The unit of volume is taken as the volume for the diamond structure at 0 K. The solid lines are from our calculations, while the solid circles are from *ab initio* calculations of ref. 94.

structure solid at 0 K. The initial configuration for the preliminary simulation is diamond-structure solid. The liquid structure is realized by sequentially increasing the system total energy until the system melts. The system is judged to have melted by studying the relation between the average potential energy and temperature [95]. The initial configuration for the productive simulations is constructed by arranging four of the above-described cubes so that the resulting simulation cell is a rectangular parallelepiped of size 22.6Å × 22.6Å × 11.3Å, followed by a suitable rescaling of the entire simulation cell according to the density.

The initial velocities are drawn from a Maxwellian distribution, with the temperatures set at the experimental values. The one-electron energy is calculated at the Γ-point. Equation (2.6) is solved by direct diagonalization. The temperature of the system is controlled by means of the Nosé-Hoover thermostat [35]. The thermal mass parameter is chosen in the following manner. According to Nosé [35], the characteristic frequency of the thermostat ω_T can be written as:

$$\omega_T^2 = \frac{2gk_{\mathrm{B}}T}{Q} \tag{6.7}$$

The value of Q is chosen so that ω_T is in the same order of the characteristic frequency of the system ($\sim$ 10 ps^{-1}).

The equation of motion is integrated by using a six-value Gear algorithm [7]. The pressure of the system is evaluated from the Virial theorem [7]. The time step is chosen to be 2.4 fs. Simulations are performed over 5000 steps, resulting in a simulation time of 12 ps. The data obtained from the last 4000 steps are used to calculate physical quantities. We perform our simulations for ℓ-Ge with density ranging from 5.53 $\mathrm{g\,/\,cm^3}$ (density for ℓ-Ge at atmospheric pressure) to 7.49 $\mathrm{g\,/\,cm^3}$ (density for ℓ-Ge at $P = 25.0$ GPa). We hereafter refer to the density as ρ.

Statistical errors are estimated by assuming that the quantity under interest is a Gaussian process [7]. The simulation is divided into four parts (1000 steps for each part), and the standard deviation calculated from these four parts are deemed as statistical errors.

Finally, in Figs. 6.2 (a) and (b), we show the temperature and pressure of our simulations, plotted against density. Note that the pressure obtained from our simulations are in remarkable agreement with those of experiments with the same density.

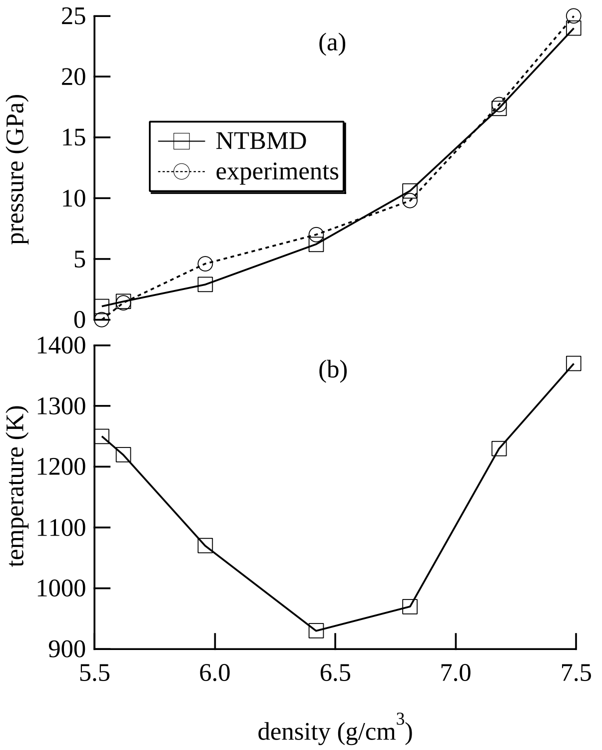

Figure 6.2: The pressure and temperature of our simualations, plotted against density; (a) : pressure, and (b) : temperature. In (a), the solid line with squares is from our calculations, while dashed line with circles are from experiments.

6.3 Results and discussions

6.3.1 static structure

Here, we study the change in the static structure as the density of ℓ-Ge increases. We investigate the following properties:

1. *two-body correlation*
    - two-body distribution function, $g(r)$, and auxiliary quantities.
    - static structure factor, $S(Q)$, and auxiliary quantities.
2. *three-body correlation*
    - bond-angle distribution function, $g^{(3)}(r_{\mathrm{c}}, \theta)$.
    - the "covalent part" of the bond-angle distribution function, $g^{(3)}_{\mathrm{covalent}}(r_{\mathrm{c}}, \theta)$.

Further, in order to obtain a visual image for the structural change, we also study the snapshots of typical atomic configurations.

two-body correlation

two-body distribution function We first calculate the two-body distribution function, $g(r)$. In Fig. 6.3, we show our results, along with the results obtained from experiments [81,88]. As can be seen from these figures, our results are in excellent agreement with experiments in all regions of density studied from the lowest up to the highest, which again confirms the validity of our NTB scheme and our choice of parameters.

We note that, as density increases, the following trends are observed from both simulations and experiments:

1. the position of the first peak, r_1, does not change dramatically, despite a great increase in density,
2. the position of the second peak, r_2, on the other hand, changes considerably,
3. the heights of the first and second peak increase,

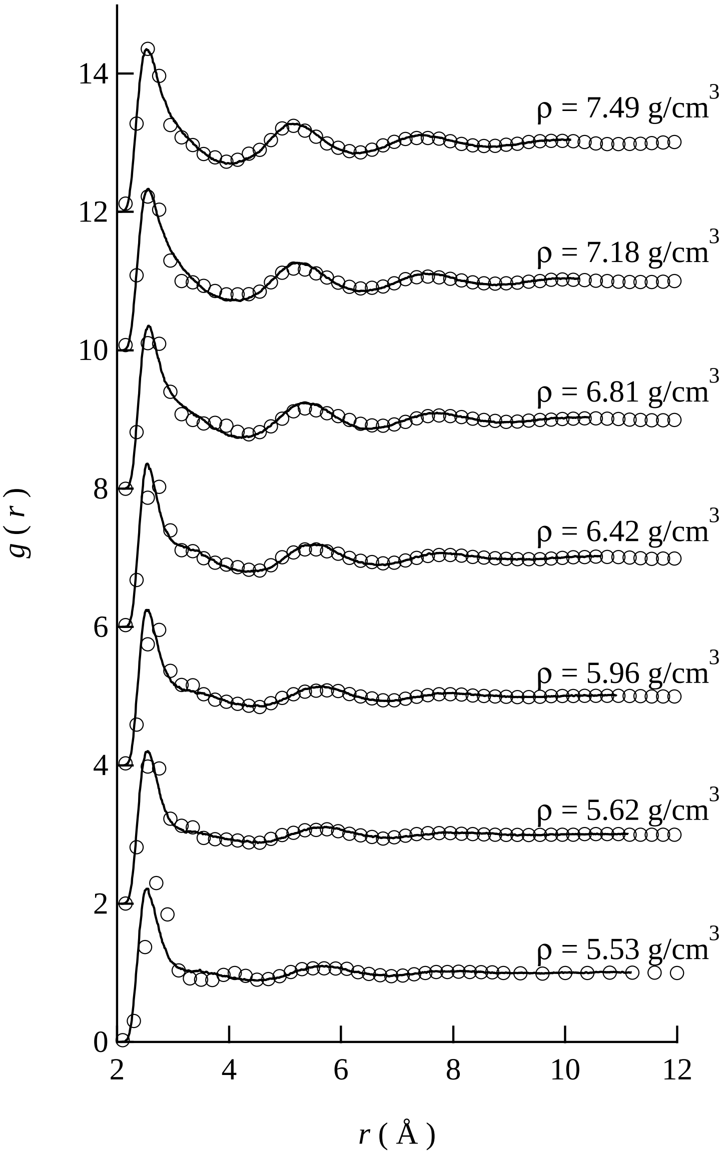

Figure 6.3: The pair-distribution function $g(r)$ at each density. The solid lines are our results, while the open circles are results from experiments. Experimental results for the lowest density is taken from ref. 81, while other results are taken from ref. 88.

4. the dip between the first and second peak becomes deeper.

In Fig. 6.4, we show r_1 and r_2 plotted against density, scaled by the corresponding values at 5.53 g/cm^3, the lowest density investigated. Also plotted in Fig. 6.4 is the cubic root of the volume of the simulation cell, which we denote as ℓ_{cell}, scaled in the same way as r_1 and r_2.

Firstly, we find from this figure that up to $\rho = 6.81\ \mathrm{g}/\mathrm{cm}^3$, r_1 increases (not decreases), small though the increment is, according to the increase of density. This is an unusual behav-

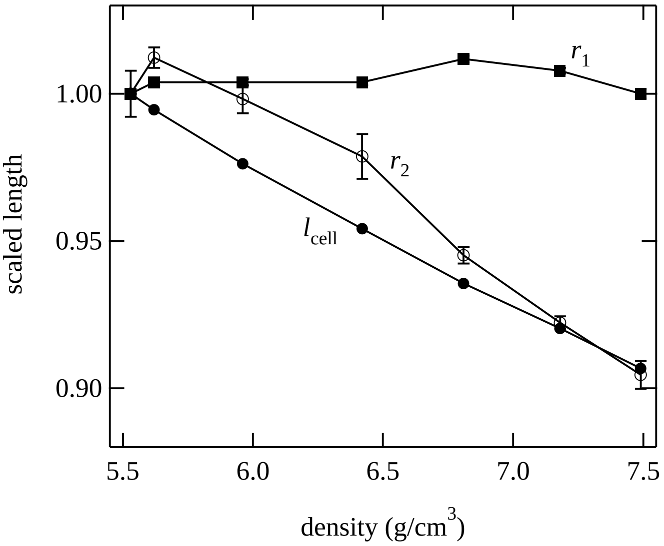

Figure 6.4: The position of the first peak of $g(r)$, r_1, and of the second peak of $g(r)$, r_2, plotted against pressure, with error bars. Also plotted in this figure is the cubic root l_{cell} of the simulation volume. All values are scaled by the corresponding values at the lowest pressure.

ior, because the volume of the simulation cell itself is obviously smaller at higher densities. The increase of r_1 implies that the application of pressure is accompanied by non-uniform compression, which leads to significant changes in the local structure.

We also find from this figure that for r_2, the behavior is as expected; it decreases as density increases. From this figure, we understand that the change of r_2 is almost proportional to ℓ_{cell}. This indicates that r_2 decreases more or less uniformly as density increases. We also note that the change of r_1 is very small compared to that of r_2. The decrease of r_1 at high density is an expected behavior, but the degree of decrease is trivially small, and it is much smaller than the decrease of r_2 and ℓ_{cell}. This implies that the local structure changes considerably for all densities investigated.

The ratio of the positions of the first and second peak, r_2/r_1, plotted against density, is shown in Fig. 6.5. This quantity is known to reflect the structure of liquids in the following way [21,96]. For isotropic liquids, the value of r_2/r_1 is about 1.91, and as the anisotropy of the local structure increases, the value of r_2/r_1 increases. We find that, for ℓ-Ge at low density, r_2/r_1 has a highly anisotropic value of 2.2, and decreases as density increases, or in other words, becomes closer to an isotropic liquid. This does not mean, however, that anisotropy

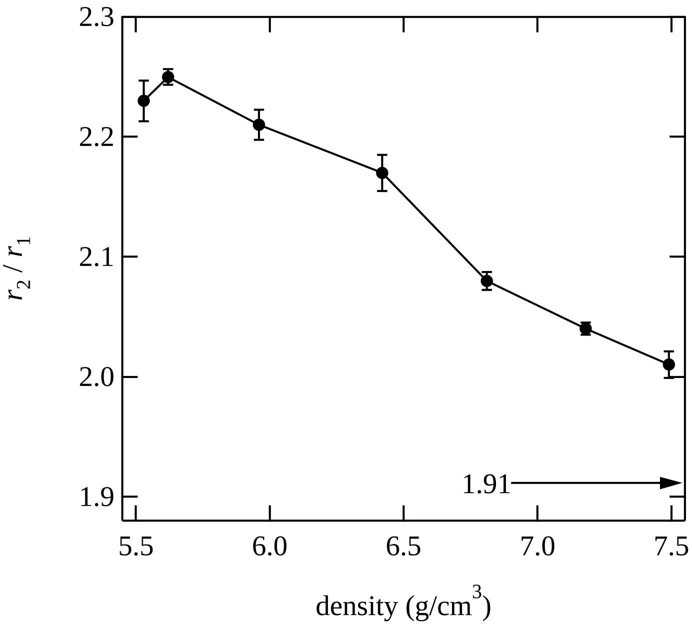

Figure 6.5: The ratio of the second and first peaks of $g(r)$ plotted against pressure, with error bars. The corresponding value for close-packed liquids, 1.91, is also shown by an arrow.

completely disappears at high pressures, because the value of r_2/r_1 is still an anisotropic value of ~ 2.0 even at the highest density investigated.

Generally speaking, it is expected that metallic bonds are isotropic and covalent bonds are anisotropic. On the basis of this fact, it is natural to assume that isotropic structures originate from metallic bonds, while anisotropic structures originate from covalent bonds. In this respect, the behavior of r_2/r_1 in Fig. 6.5 indicates that as density increases, the system becomes more metallic, although the covalent nature persists even at densities as high as 7.49 $\mathrm{g}\,/\,\mathrm{cm}^3$, the highest density investigated. We note that, from this view point, the increase of r_1 at low density is understood in terms of the weakening of the strong covalent bonds.

coordination number We now proceed to the evaluation of the coordination number N_c. Here, a problem arises as to the way to define the length of the first-coordination shell, r_fcs, because the first coordination shell is not a well-defined concept in liquids. This is particularly true for covalent liquids, because the shape of the first peak in $g(r)$ is usually highly asymmetric for these liquids. Further, the results are very sensitive to the choice of this value r_fcs. For example, $r_\mathrm{fcs} = 2.9\text{Å}$ at $\rho = 5.53\ \ \mathrm{g}\,/\,\mathrm{cm}^3$ gives $N_\mathrm{c} = 4.1$, while $r_\mathrm{fcs} = 3.3\text{Å}$, corresponding to

Table 6.2: The values of r_0, r_1, and r_{fcs}. Refer to the text for a definition of these quantities.

ρ (g / cm^3)	r_0 (Å)	r_1 (Å)	r_{fcs}(Å)
5.53	2.13	2.52	2.91
5.62	2.14	2.53	2.92
5.96	2.15	2.53	2.91
6.42	2.17	2.54	2.96
6.81	2.16	2.56	2.97
7.18	2.13	2.55	2.97
7.49	2.11	2.54	2.97

the position of the first minimum of $g(r)$, gives $N_{\mathrm{c}} = 6.4$. The difference is considerably large. Therefore, it is important that we adopt the same definition of r_{fcs} for all data, and discuss their relative changes.

In the present chapter, we define r_{fcs} as $r_{\mathrm{fcs}} = r_1 + (r_1 - r_0)$, where r_0 is the distance at which $g(r)$ starts rising; to be more precise, we take r_0 so that $g(r_0) = 0.01$. In Table 6.2, we show the values of r_0, r_1, and r_{fcs} for all of our simulations.

In Fig. 6.6 (a), we plot N_{c} against density. We see from this figure that N_{c} increases as density increases, which is consistent with our findings thus far that, as density increases, the system becomes more metallic. We note here that, even under the highest density investigated, 7.49 g / cm^3, N_{c} is less than the characteristic values found in simple liquids, which is 10-11. This is again consistent with our findings thus far that the covalent nature is preserved even at densities as high as 7.49 g / cm^3.

Now let us further study the distribution of N_{c} in Fig. 6.6 (b). With the increase of the density, a decrease of four-fold atoms and an increase of eight-fold atoms is observed, while six-fold atoms first increase with density, and decrease for densities higher than 6.81 g / cm^3. For all densities, the distribution of N_{c} changes, which implies that the local structure of the liquid is different for all densities studied.

static structure factor In the next place, we calculate the static structure factor, $S(Q)$. In Fig. 6.7, we show the calculated $S(Q)$ for all densities investigated, along with results obtained from experiments. From these figures, we see that our results are again in excellent

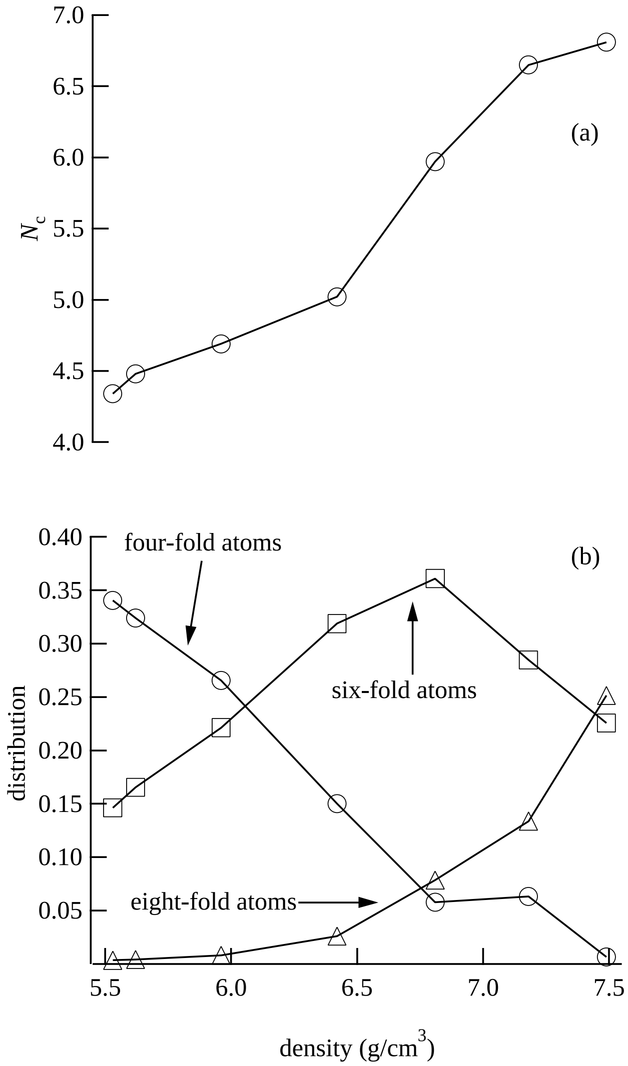

Figure 6.6: The coordination number, plotted against pressure, (a): total coordination number, and (b): distribution of the coordination number. For (b), open circles denote four-fold atoms, open squares denote six-fold atoms, and open triangles denote eigh-fold atoms.

agreement with experiments. The changes that the increase of density brings about are especially well reproduced, which provides strong evidence that our simulations give realistic atomic configurations for both low- and high-density liquids.

We note that, as density increases, the following trends are observed from both simulations and experiments:

1. the shoulder on the immediate right-hand side of the first peak becomes less distinct, although it still exists at $\rho = 7.49\ \mathrm{g}/\mathrm{cm}^3$.

2. the height of the first peak increases.

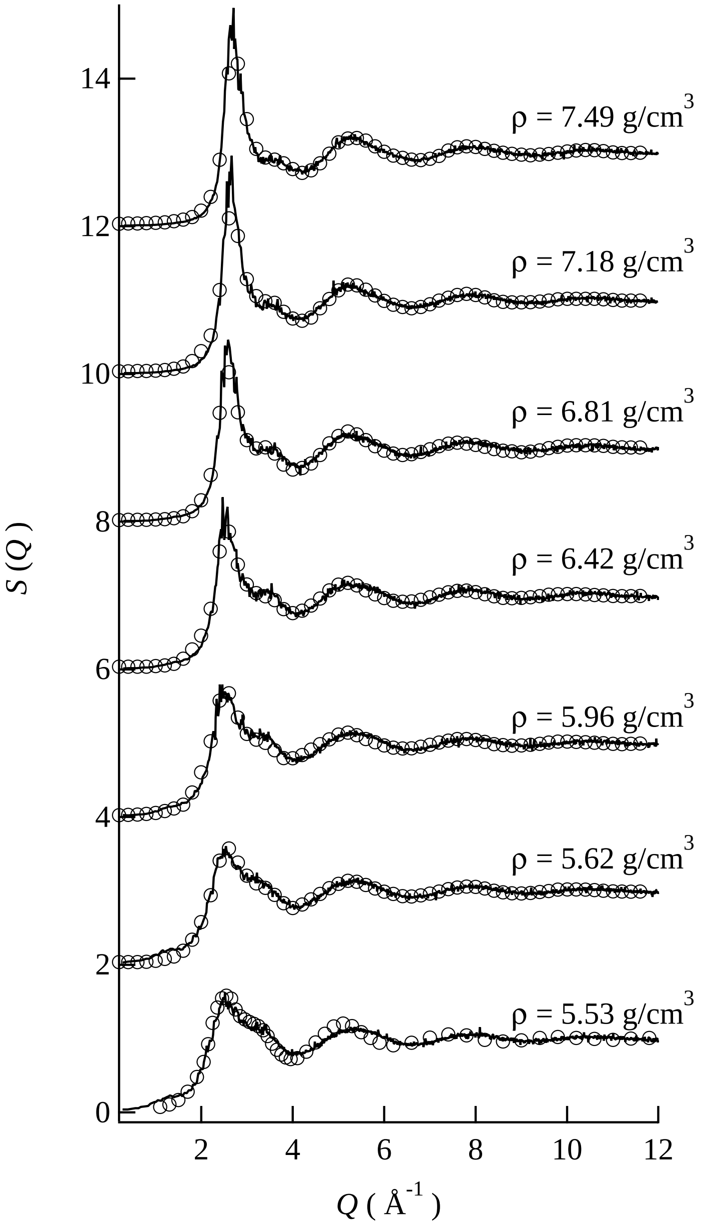

Figure 6.7: The static structure factor $S(Q)$ at each density. The correspondence of the solid lines and open circles are the same as those in Fig. 6.3.

3. $S(Q)$ at $\rho = 7.49\ \mathrm{g\,/\,cm^3}$ resembles $S(Q)$ of ℓ-Sn at ambient pressure.

Among the features listed above, the most striking one is that the shoulder next to the first peak, which has been interpreted as evidence that covalent bonds persist in the liquid state [21, 87], decreases in magnitude as density increases. We also note that the shoulder, although less distinct, still exists at $\rho = 7.49\ \mathrm{g\,/\,cm^3}$.

These findings give support to the results obtained from $g(r)$, that (1) the degree of metallic nature in the liquid increases as density increases, and (2) covalent bonds still exist at densities as high as 7.49 $\mathrm{g/cm^3}$. This behavior of ℓ-Ge is also seen from the ratio of the first and second peaks of $S(Q)$, Q_2/Q_1, plotted against density, shown in Fig. 6.8. This quantity, along with

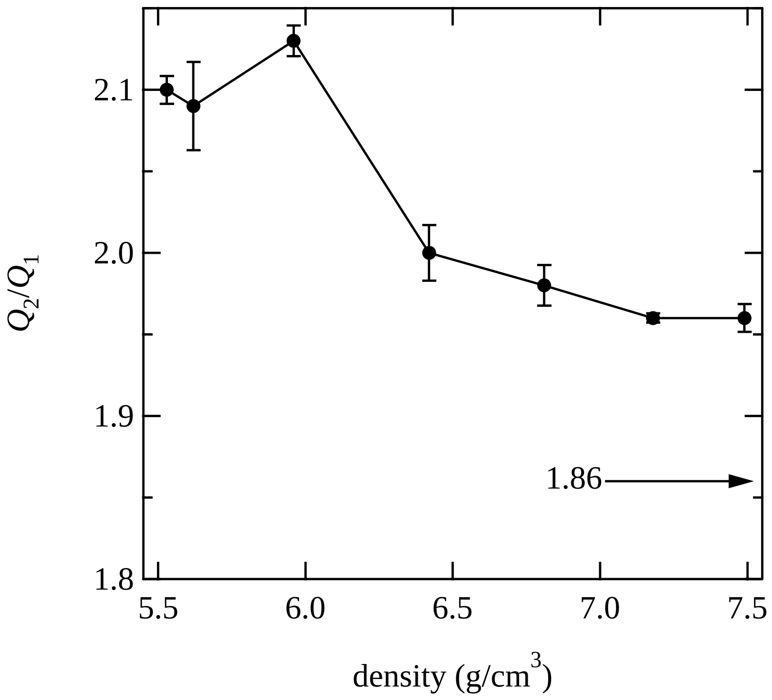

Figure 6.8: The ratio of the second and first peaks of $S(Q)$, plotted against pressure. The corresponding value for close-packed liquids, 1.86, is also shown by an arrow.

r_2/r_1, has been used to characterize the structure of liquids [21, 96]. For close-pack liquids, Q_2/Q_1 typically takes the value of 1.86, and as the anisotropy of the local structure increases, Q_2/Q_1 also increases [21, 96]. From Fig. 6.8, we find that at low densities, Q_2/Q_1 is about 2.1-2.15, a highly anisotropic value, and for densities higher than 6.81 $\mathrm{g/cm^3}$, Q_2/Q_1 is about 1.95-2.0, which is close to the value found for ℓ-Sn at ambient pressure, but larger than the close-pack value of 1.86. This behavior of Q_2/Q_1 again indicates that covalent and anisotropic structure at low density becomes a more metallic and isotropic structure as density is increased.

three-body correlation

bond-angle distribution function From both $g(r)$ and $S(Q)$, we have seen thus far that the local structure of ℓ-Ge is covalent and anisotropic in the low-density region, while it is more metallic and isotropic in the high-density region. We have also seen that the atomic configurations of ℓ-Ge are not completely isotropic even at densities as high as 7.49 $\mathrm{g/cm^3}$. We will now proceed on to the calculation of the bond-angle distribution function, which will make our discussions clearer. An important point is that this property about the bond-angle distribution cannot be derived from experiments. In other words, the properties of this kind, non-attainable from experiments, are exactly what gives credit to simulational work for elucidating the detailed atomic configurations in liquids.

The bond-angle distribution function, $g^{(3)}(r_c,\theta)$, gives the distribution of the angles formed by pairs of vectors drawn from a reference atom to any two other atoms within a cutoff radius r_c of that reference atom. In Figs. 6.9 (a) and (b), we show $g^{(3)}(r_c,\theta)$, normalized by $(\sin\theta)^{-1}$. We take two different values for r_c, namely, r_1 and r_{fcs}.

From Figs 6.9 (a) and (b), we observe significant changes in the distribution of the bond angles according to the increase of density. For the low-density liquids, we find a broad peak at 90°-110°, characteristic of covalent, tetrahedral bonding from both cutoff distances. The position of the peak is roughly the same in both cases. At $r_c = r_{\mathrm{fcs}}$, we find another peak around 60°. This peak corresponds to contribution from metallic bonds. The two-peak structure of $g^{(3)}(r_c,\theta)$ for the low-density liquids clearly shows that the bonding in ℓ-Ge is indeed a mixture of covalent and metallic bonds, and that the local structure of ℓ-Ge is determined from the competition of these two kinds of bonds.

On the other hand, $g^{(3)}(r_c,\theta)$ of high-density liquids differs greatly from that of low-density liquids. For $r_{\mathrm{c}} = r_{\mathrm{fcs}}$, the 90°-110° peak found for the low-density liquids shifts to the low-angle side according to the increase of density, and becomes a broad peak, ranging from 60° to 80°-90°. We also find that the peak position of this peak depends on the value of r_{c}. For $r_{\mathrm{c}} = r_1$, the peak position is about 90°, while for $r_{\mathrm{c}} = r_{\mathrm{fcs}}$, the peak position shifts to the low-angle side. Finally, we observe a slight hint of another peak at around 150°-180° for both cutoff distances.

This behavior of $g^{(3)}(r_c,\theta)$ indicates that, for high-density liquids, the local structure is almost isotropic, with a broad characteristic peak at 60°. However, $g^{(3)}(r_c,\theta)$ of the high-density liquid is not completely isotropic, as the 60°-90° peak is actually too broad in width and too low in height for a completely isotropic liquid. The behavior of $g^{(3)}(r_c,\theta)$ at high

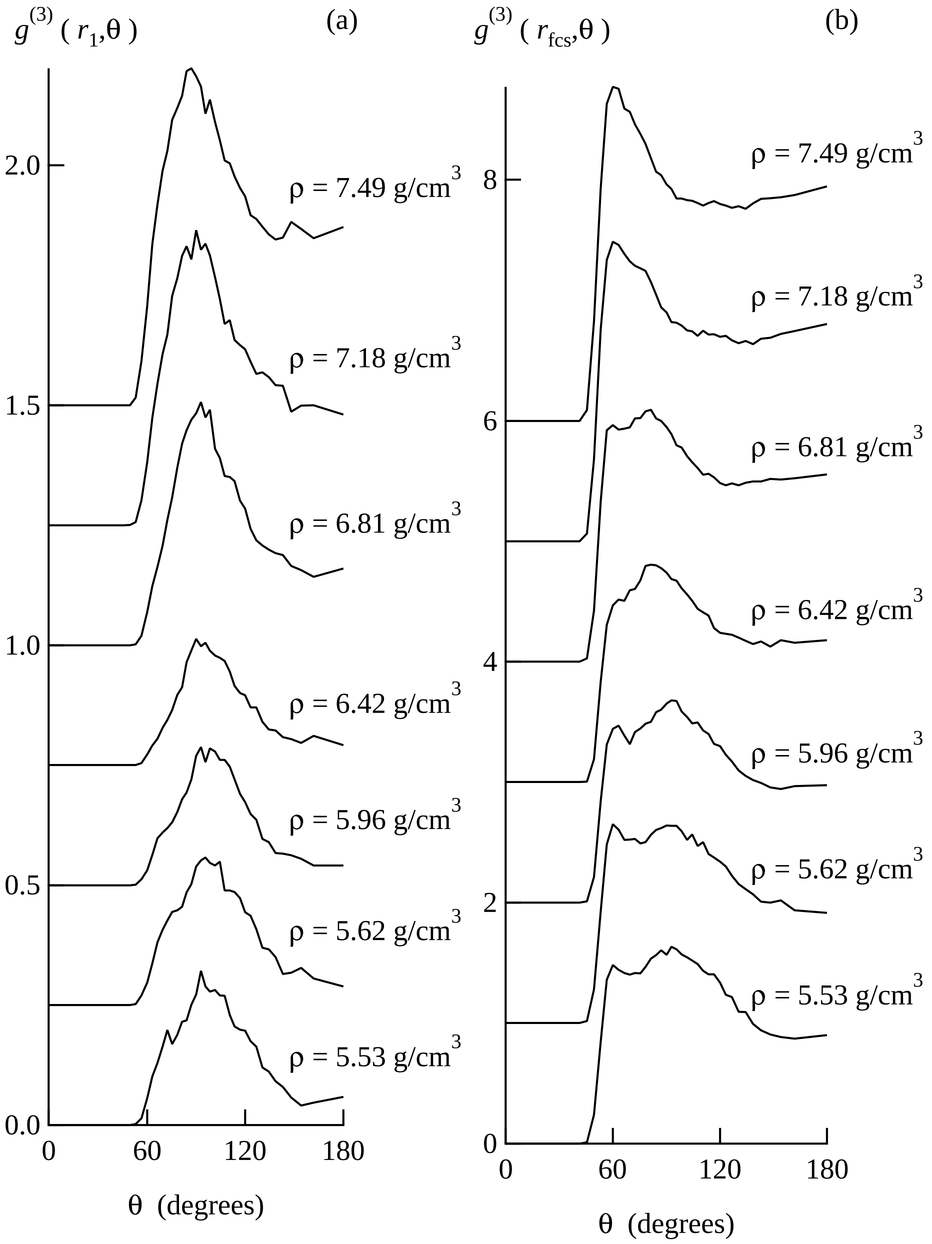

Figure 6.9: The bond-angle distribution function $g^{(3)}(r_{\mathrm{c}},\theta)$ at each density.

pressures can also be interpreted as mixture of covalent and metallic bonds, with higher percentage of metallic bonds. This point is investigated further in the following.

"covalent part" of the bond-angle distribution function We have seen that, for both the low- and high-density liquids, the local structure is characterized as a mixture of covalent and metallic parts. Now, let us try to divide $g^{(3)}(r_c,\theta)$ into these two parts.

We firstly assume that the contribution to $g^{(3)}(r_c,\theta)$ from the isotropic part of atomic configurations is expressed by that obtained from a Lennard-Jones (LJ) 9-6 liquid, which we will denote as $g^{(3)}_{\text{isotropic}}(r_c, \theta)$. We calculate $g^{(3)}_{\text{isotropic}}(r_c, \theta)$ at $T^* = 1.0$ and $\rho^* = 0.8$, where T^* and ρ^* denote scaled temperature and density for the LJ potential [7, 97], respectively. We note that the temperature and density chosen are in the region of the stable liquid phase of the LJ 9-6 potential [97–99]. The value of r_c for $g^{(3)}_{\text{isotropic}}(r_c, \theta)$ is chosen as ~ 1.20, where the unit of length is again the scaled units of the LJ potential [7, 97]. The reason why we extract the contribution from the isotropic part from the whole atomic configuration is that we like to clarify the behavior of the anisotropic contributions. In other words, we regard the difference $g^{(3)}(r_c, \theta) - g^{(3)}_{\text{isotropic}}(r_c, \theta)$ as the contribution from the anisotropic part of atomic configurations, which is mainly attributed to the covalent nature of cohesion. As a result, this difference is expected to provide us with ample information about the local configurations of atoms. We denote this difference as $g^{(3)}_{\text{covalent}}(r_c, \theta)$, which we try to express by the sum of five Gaussians to be fitted properly.

In Figs. 6.10 (a) and (b), we show the results of such fitting procedures for ℓ-Ge at $\rho = 5.53\ \text{g}/\text{cm}^3$ and $7.49\ \text{g}/\text{cm}^3$, with the value of r_c in $g^{(3)}(r_c, \theta)$ chosen as $r_c = r_{\text{fcs}}$. From Figs. 6.10 (a) and (b), we see clearly that the ratio of metallic bonding is indeed larger for high-density ℓ-Ge than low-density ℓ-Ge, in agreement with our findings from $g(r)$ and $S(Q)$.

In Fig. 6.11, we show $g^{(3)}_{\text{covalent}}(r_c, \theta)$ for all densities investigated. From these figures, we find significant differences in low- and high-density liquids.

For low-density liquids, we have a single broad peak, with peak position at $\sim 90°$. This broad peak can be interpreted as reflections of essentially tetrahedral bonding of the β-Sn type, with a very wide distribution for the bond angles. This type of distribution for the bond angle is consistent with the '*disordered*' β-Sn model [81, 86] mentioned in section 6.1, in which the structural features is characterized by a β-Sn structure with a wide distribution of bond angles. Note that it is not possible to characterize this distribution by a single β-Sn-type structure, because if this were the case, there must be another peak at the high-angle side. Instead, we observe a broad, featureless tail. This structure is interpreted as a structure close to the β-Sn structure but with large fluctuations in the atomic configurations. The broad tail is interpreted as originating from distribution of β-Sn-like structures, with different c/a ratios.

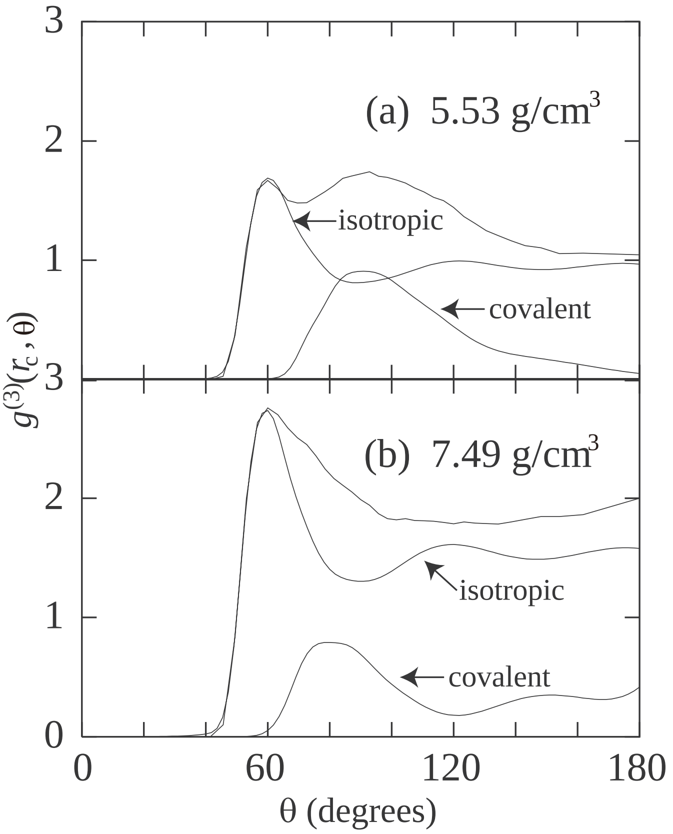

Figure 6.10: Examples of the fitting results described in the text for (a): 1.1GPa, and (b): 24.0GPa.

As density is increased, we find that the width of this peak becomes gradually narrower, and at 6.81 g / cm^3, a new peak arises at 150°-180°. We also observe a dip at $\sim$ 120° at the high-density region. The relatively narrow peak is interpreted as a mixture of the 75°, 94°, and 105° peaks for the β-Sn structure, while the 150°-180° peak is interpreted as the 150° and 180° peaks for the β-Sn structure. The dip at $\sim$ 120° reflects the fact that there is no characteristic peaks for β-Sn structure in the region between 105°-150°. This type of distribution of the bond angle is consistent with the '*pure*' β-Sn structure mentioned in section 6.1, in which the essential structural features is characterized by the β-Sn structure with relatively narrow distribution of bond angles. The behaviors of $g^{(3)}_{\text{covalent}}(r_c, \theta)$ show that the structural model suggested from experiments [88], that low-density liquids have '*disordered*' β-Sn structure while high-density liquids have '*pure*' β-Sn structure, well accounts for the covalent part of the liquid.

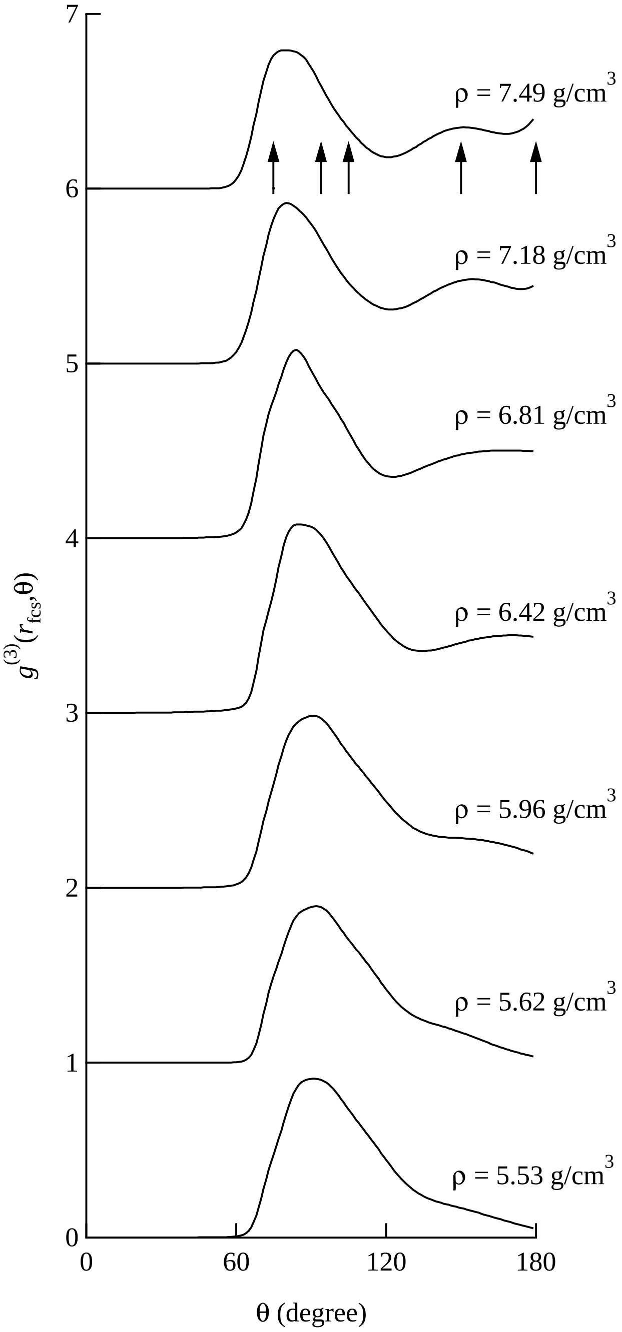

Figure 6.11: The covalent part of $g^{(3)}(r_c, \theta)$. The arrows drawn for $\rho = 7.49$ g / cm^3 indicate the characteristic angles for the solid β-Sn structure.

snap shots of atomic configurations

Finally, we show snap shots of atomic configurations at $\rho = 5.53$ g / cm^3 in Fig. 6.12 (a), and at $\rho = 7.49$ g / cm^3 in Fig. 6.12 (b). In these figures, atoms less than r_{fcs} apart are connected by bonds. From Fig. 6.12, we visually confirm that long-range order is completely lost, and

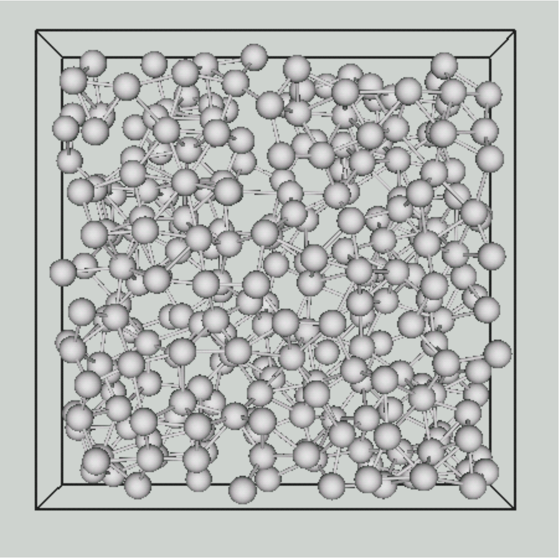

(a) ρ=5.53 g/cm^3

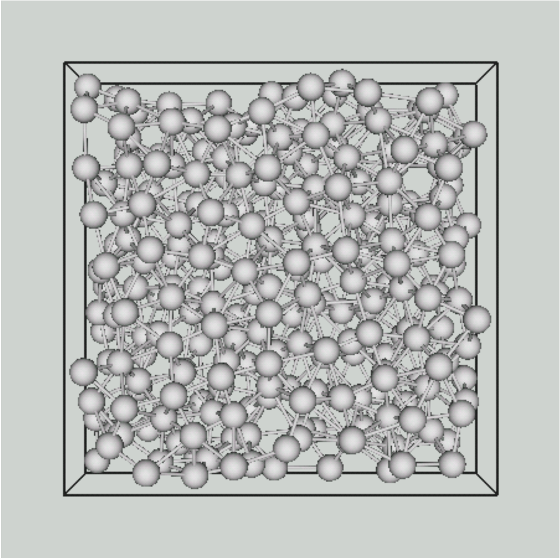

(b) ρ=7.49 g/cm^3

Figure 6.12: Snapshots of the atomic configurations, (a): 5.53 $\mathrm{g/cm^3}$, (b): 7.49 $\mathrm{g/cm^3}$

that the local structures of the low- and high-density liquids differ greatly. As found from $g(r), S(Q)$, and $g^{(3)}(r_c, \theta)$, the low-density liquid has low coordination with an anisotropic local structure, while the high-density liquid has high coordination with a more isotropic local structure. We note, however, that behaviors found for $g^{(3)}_{\text{covalent}}(r_c, \theta)$ is difficult to observe from these figures.

6.3.2 dynamical structure

Now let us study the change in the single-particle dynamics. For the dynamical structure, we calculate the following properties:

- mean square displacement (MSD),
- velocity autocorrelation function (VAF), $\psi(t)$,
- diffusion constant, D, calculated from both MSD and VAF,
- spectrum density $\psi(\omega)$.

For the high-density liquids, we also compare our results with those of crystalline β-Sn structure at high-temperature ($T = 800\,\mathrm{K}$).

mean-square displacement

In Fig. 6.13, we show the MSD obtained at each density. From this figure, it is readily seen that (1) the system shows liquid-like diffusive behavior at all densities studied, and (2) the low-density liquid is more diffusive than the high-density liquid. The better diffusive behavior of the low-density liquid is easily understood in terms of the coordination number of the system. Since the low-density liquid has smaller coordination number, it is possible for the atoms to move more freely, resulting in better diffusive behavior.

velocity autocorrelation function

Now we present the VAF calculated from our simulations in Fig. 6.14. At low densities, we find a peak around $\sim 0.2\,\mathrm{ps}$. For a purely Brownian motion, the VAF will show an exponential decay; the presence of a peak implies that there are some characteristic modes within the dynamics. In this case, it reflects the fact that covalent bonds persist in the liquid phase. As the density increases, we find that this peak becomes more distinct, and at high densities, the VAF starts to oscillate. This behavior of the VAF shows that the so-called "cage effect", in which an atom is trapped within a "cage" formed by themselves, is significant for high-density ℓ-Ge. The same phenomenon is seen for the low-density liquid to a certain extent, but the larger diffusive motion for the low-density liquid prevents the atoms from staying

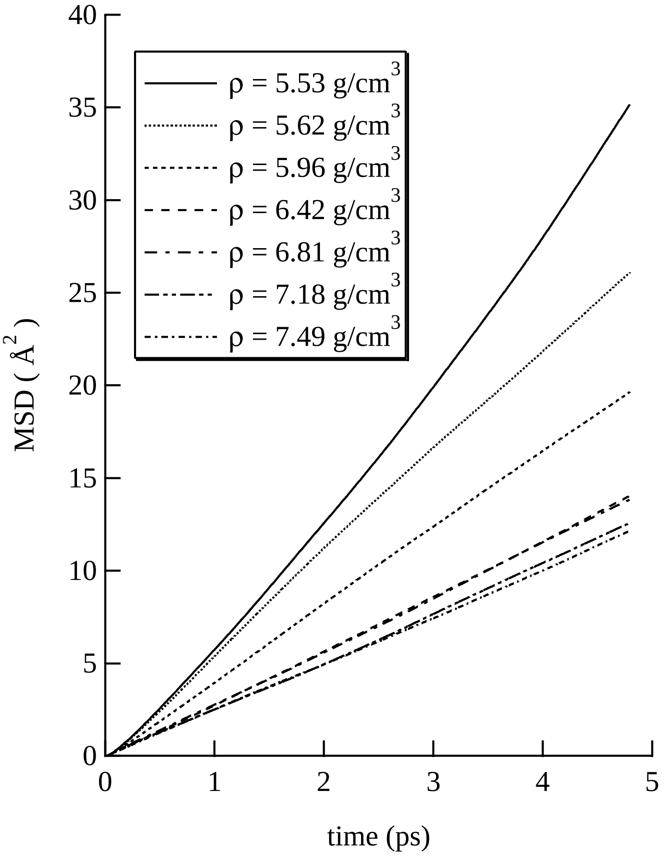

Figure 6.13: The mean-square displacement at each pressure.

within a certain region for a long time, resulting in a smaller cage effect than the case of the high-density liquid.

We now compare our results with those obtained from other simulations. In Fig. 6.15, we compare our VAF for the lowest density to that obtained in ref. 84. We observe immediately that their results and our results are quite similar; the hump is present at $t = 0.2$ ps, and further the VAF tends to zero at times longer than $t = 0.6$ ps. One difference is that the VAF obtained in ref. 84 oscillates slightly beyond $t = 0.6$ ps, and does not decay completely. This is because we are working with a larger unit cell and longer simulation time, leading to smaller statistical errors in our case.

diffusion coefficient

The diffusion coefficient D, calculated from both the MSD and the VAF, is shown in Fig. 6.16. As expected, the values obtained from the two method are reasonably close to each other.

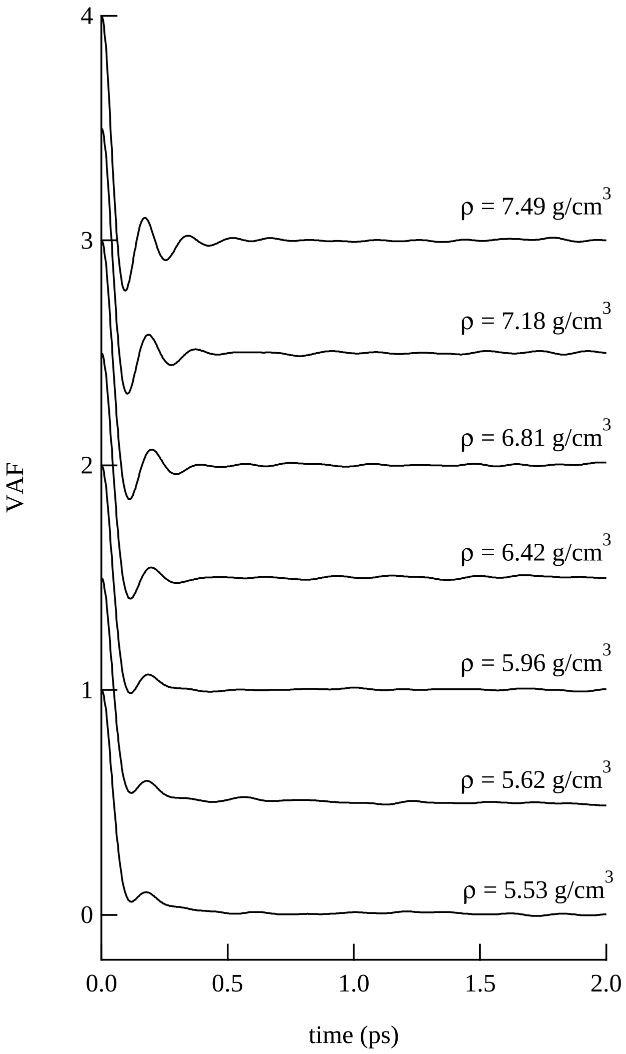

Figure 6.14: The velocity autocorrelation function at each pressure.

spectrum density

Here, we study the spectrum density. This property is important in that it is related to the phonon modes in the system.

We present in Fig. 6.17 the results for the spectrum density. For the low-density liquid, we find a hump-like peak at $\sim 30\,\mathrm{ps}^{-1}$, reflecting the phonon mode of the covalent bond. This mode softens with density increase at low densities, but at higher densities, it gradually hardens with density increase, and for the highest density studied, shifts to $\sim 35\,\mathrm{ps}^{-1}$. At the highest density studied, we find another peak at $\sim 10\,\mathrm{ps}^{-1}$. This behavior for the high-density liquid again reflects the strong cage effect found in high-density ℓ-Ge.

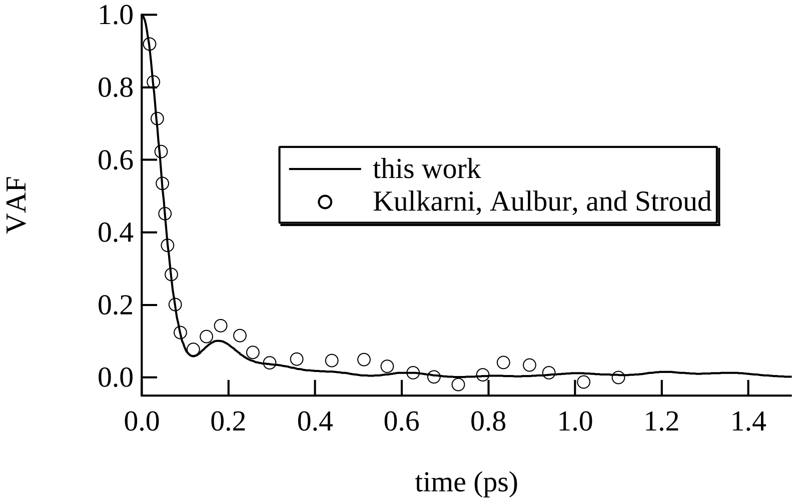

Figure 6.15: Comparison of the VAF, solid lines : VAF from our simulations, and circles : VAF from ref. [84].

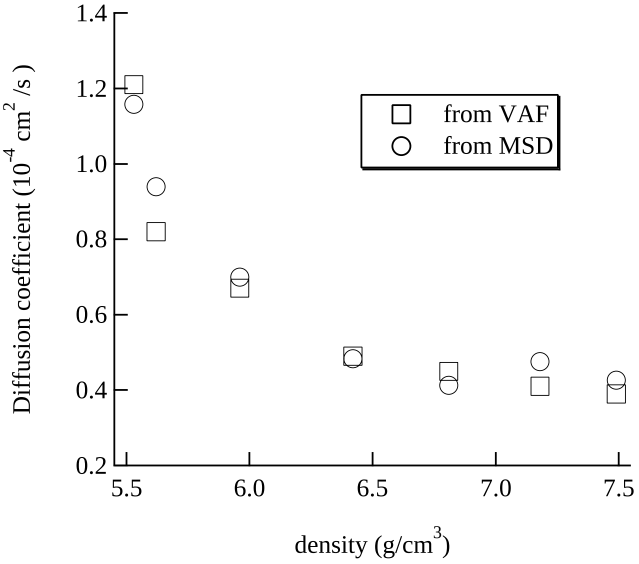

Figure 6.16: The diffusion coefficients D calculated from the VAF and the MSD. Open squares are D calculated from the VAF, while open circles are D calculated from the MSD.

comparison with crystalline β-Sn crystal

Finally, we compare our results with those of crystalline β-Sn structure. The dynamical structure of crystalline β-Sn are obtained from simulation performed with the same density, with $T = 800\,\mathrm{K}$.

In Fig. 6.18, the VAF and spectrum density are plotted for both high-density liquid Ge and crystalline β-Sn structure. The results show that the dynamical structure of ℓ-Ge and

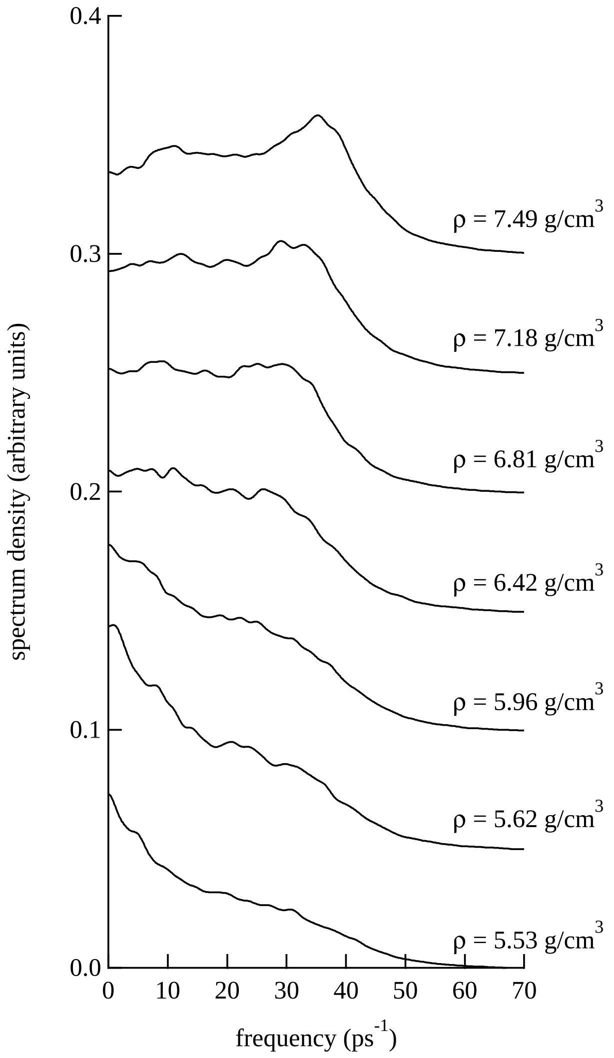

Figure 6.17: The spectrum density at each pressure.

β-Sn crystal are quite similar. For the VAF, we find that the period of oscillation is roughly equal; only the liquid damps much faster, reflecting the disorder and diffusion present in the liquid. For the spectrum density, the peaks are located at comparable frequencies, but the distribution for the high-density liquid is broader. Another difference is seen in the region where the frequency is almost zero; these modes correspond to diffusive modes, which is completely absent for the case of the β-Sn structure.

From these results, we clearly observe that the dynamical structures of high-density ℓ-Ge are similar to those of the β-Sn structure, with differences coming from disorders and diffusion present in liquids.

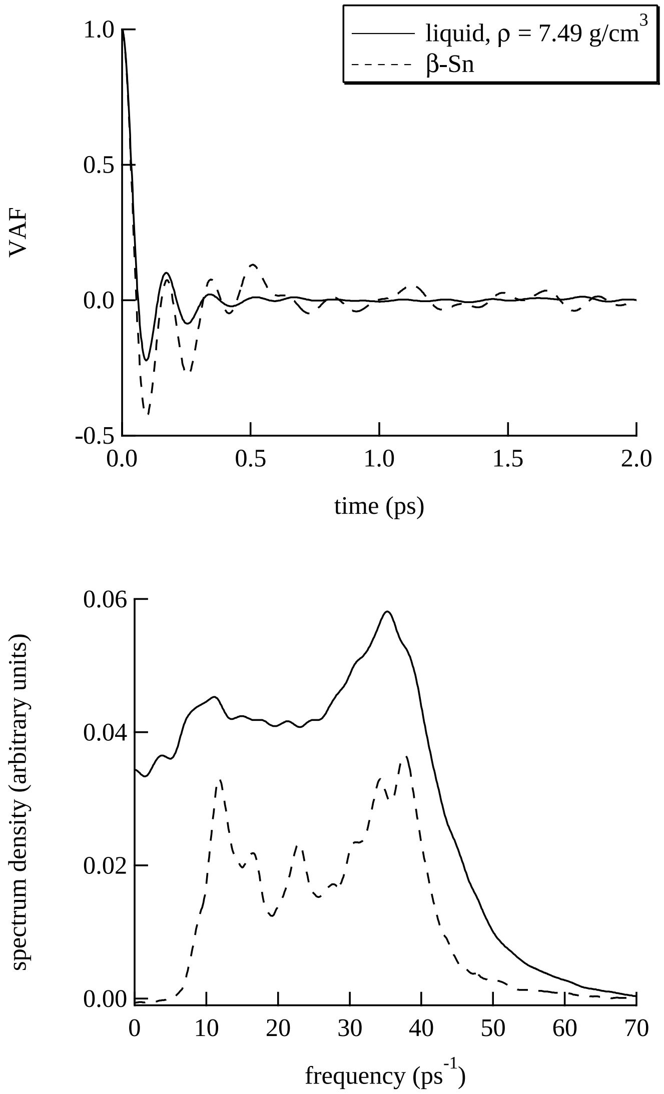

Figure 6.18: Comparison between the dynamical structures of high-density liquid and high-temperature β-Sn crystal, (a): for the VAF, and (b): for the spectrum density. Solid lines represent data for the high-density liquid, while dashed lines represent data for the high-temperature crystal.

6.3.3 summary of results and discussions

The results obtained in the present section are summarized as follows.

I Static structure,

1. *two-body correlation*
    - from $g(r)$,

      (a) the position of r_1 does not change dramatically, despite a great increase in the density,

  - **(b)** the dip between the first and second peak increase,
  - **(c)** coordination number N_{c} increases with density
- from $S(Q)$,
  - **(a)** the shoulder on the immediate right-hand side of the first peak becomes less distinct,
  - **(b)** the height of the first peak increases,

2. *three-body correlation*
   - from $g^{(3)}\left(r_{\mathrm{c}}, \theta\right)$,
     - **(a)** at low densities, a broad peak at $90^{\circ} \sim 110^{\circ}$ is found,
     - **(b)** at high densities, a broad peak at 60° is found,
   - from $g_{\text{covalent}}^{(3)}\left(r_{\mathrm{c}}, \theta\right)$,
     - **(a)** at low densities, the local structure of ℓ-Ge is interpreted as a mixture of tetrahedral covalent bonds and isotropic cohesion,
     - **(b)** at high densities, the local structure of ℓ-Ge interpreted as a mixture of covalent bonds close to crystalline β-Sn structure and isotropic cohesion
     - **(c)** isotropic cohesion is more significant for the high-density liquid

II Dynamical structure

- from MSD,
  - **(a)** diffusive behavior is found for all densities
  - **(b)** low-density liquids diffuse more readily than high-density liquids
- from $\psi(t)$,
  - **(a)** The so-called “cage effect” is larger for the high-density liquids,
  - **(b)** the VAF of high-density liquids are similar to that of high-temperature crystalline β-Sn
- spectrum density, $\psi(\omega)$.

(a) a shoulder-like phonon peak is found at $\sim 30\,\mathrm{ps}^{-1}$ for the low-density liquids, while a two-peak structure, with peak positions at $\sim 10\,\mathrm{ps}^{-1}$ and $\sim 35\,\mathrm{ps}^{-1}$, is found for the high-density liquids

(b) the spectrum density for the high-density liquids are similar to that of high-temperature crystalline β-Sn

Our results from the static structure imply that, for the low-density liquids, the covalent bonds are significant, while for the high-denity liquids, the covalent bonds are not as significant. On the other hand, the dynamical structures show that the dynamics of low-density liquids are relatively closer to Brownian dynamics, while those of the high-density liquids are relatively closer to the corresponding crystalline systems. The results for the static and dynamical structures, at first glance, seem to contradict, but it is possible to interpret these results in the following manner.

For low-density liquids, the covalent bonds are relatively more significant than the metallic bonds. This results in an open structure, as seen from our calculations, which is why the atoms diffuse more readily than high-density liquids. Consequently, the dynamical structures become close to those of Brownian dynamics, despite the existence of a large percentage of covalent bonds. On the other hand, for high-density liquids, liquid-like isotropic bonds are relatively more significant compared to the case of low-density liquids. This results in a more close-packed structure compared to low-density liquids, leading to less diffusive behavior. As a consequence, dynamical structures have significant "cage effects", and further, become close to those of crystalline systems, despite the fact that covalent bonds are not as significant as in the case of low-density liquids.

6.4 Conclusions for this chapter

In this chapter, we perform TBMD simulations on ℓ-Ge at seven different pressures. We find that the local structure of ℓ-Ge changes very much under pressure, as suggested from experiments [88].

Our TB scheme is constructed by modifying an NTB scheme reported previously [89]. The calculated $g(r)$ and $S(Q)$ from our TB scheme are found to be in excellent agreement with experimental results.

For $g(r)$, we have found that r_1 increases as density increases at low pressures, which is a consequence of the significant change in the local structure. We have observe that r_2/r_1 has the covalent values at low pressures, and isotropic values at high pressures. For $S(Q)$, we find that the shoulder next to the first peak decreases as density increases, which is interpreted as evidence that the covalent bonds in ℓ-Ge decrease with increasing density. We also observe that this shoulder, although small in magnitude, still exists at the highest density investigated. We find that Q_2/Q_1 shows similar behaviors as r_2/r_1. The general trends found from $g(r)$ and $S(Q)$ are that local structure of ℓ-Ge can be interpreted as a mixture of covalent and metallic parts, and that the ratio of the metallic part increases as density increases, although covalent bonds still exist at $\rho = 7.49\ \mathrm{g\,/\,cm^3}$ ($P = 24.0$GPa). The agreement between our simulational results and experimental data concerning $g(r)$ and $S(Q)$ confirms the validity of our new TB scheme.

The advantage of simulational work over experiments consists in the fact that it makes possible to evaluate the properties about atomic configurations which are not achieved from experiments. Such properties include the bond-angle distribution function $g^{(3)}(r_c, \theta)$ which is fully analyzed in the preceding section. Our analyses clarify that, at low pressures, the atomic configuration of ℓ-Ge is a mixture of tetrahedral covalent bonds (or '*disordered*' β-Sn structure) and isotropic cohesion, while, at high pressures, the configuration is a mixture of covalent bonds as regarded as '*pure*' β-Sn structure and isotropic cohesion. The key to the success of this detailed analyses has been the idea to extract the contributions from the essentially anisotropic part of atomic configurations by subtracting the contributions from the isotropic nature of atomic distributions, $g^{(3)}_{\mathrm{isotropic}}(r_c, \theta)$ from the total value of the bond-angle distribution, $g^{(3)}(r_c, \theta)$.

We also calculate the dynamical structure of the system. From the mean-square displacement, we find that high-density ℓ-Ge is less diffusive than low-density ℓ-Ge, while from the velocity autocorrelation function and the spectrum density, we find that the dynamical structures of high-density ℓ-Ge is quite close to those of the β-Sn structure, again showing that covalent contribution to the high-density ℓ-Ge is characterized as '*pure*' β-Sn structure.

Chapter 7

Amorphous germanium: glass transition and high-density structure

7.1 Introduction for this chapter

Amorphous germanium (a-Ge) is a network-forming amorphous solid, with essentially tetrahedral bonding at atmospheric pressure. The particular interest of this system lies in that it seems to have a very different short-range order from liquid germanium (ℓ-Ge). This fact implies that a large structural change occurs as the liquid is quenched into a-Ge via glass transition, but a detailed analyses of such large structural change have been limited. Simulational methods are best suited to study such problems.

Glass-transition simulations of Ge have been performed by *ab initio* MD [44] for $N = 64$ and by classical Stillinger-Webber potential [95] for larger systems [100]. Since the marked feature of an amorphous solid is the presence of short-range order and the absence of long-range order, it is useful to perform MD simulations based on quantum-mechanically-derived forces for systems larger than $N = 64$. With this situation in mind, it is the first purpose of the present chapter to perform glass-transition simulation of Ge by our $O(N)$ tight-binding molecular dynamics ($O(N)$ NTBMD) method. We quench ℓ-Ge from well above melting temperature into an amorphous solid, with $N = 512$. We thoroughly examine the structural properties at each temperature, and deduce the structural change of Ge as it transforms from liquid to super-cooled liquid, and finally into amorphous solid.

The behavior of a-Ge under pressure has been of considerable interest in the past, since tetrahedrally-bonded amorphous materials show complex structural changes when compressed

[101]. Of particular interest is the possibility of polyamorphism, in which some distinct phases of low-density amorphous (LDA) and high-density amorphous (HDA) structures realize.

In order to elucidate the high-pressure form of a-Ge, several experimental studies have been made [101–103]. The results of these studies imply that, depending on the sample preparation and pressure-loading conditions, it is possible that different types of high-pressure structures realize. In ref. 101, a “distorted β-Sn structure” was reported as high-pressure form of a-Ge. Note that the β-Sn structure is the high-pressure form of crystalline Ge (c-Ge) [104]. In ref. 102, it was reported that 25% of the atoms in a system transform into crystalline β-Sn, while the rest of atoms remain amorphous. No significant structural changes were found in ref. 103.

A simulational study on the topic has been performed in ref. 105, in which a clear first-order transition from an LDA phase to an HDA phase was reported. The initial amorphous structure was prepared using the Wooten-Winer-Weaire (WWW) algorithm [106], which generates defect-free tetrahedral amorphous configurations, usually referred to as “continuous random network (CRN)”. According to the aforementioned experimental studies, the results are not necessarily the same if some different initial configurations are used. For this reason, it is interesting to further pursue this problem by means of computer simulations, using initial configurations other than those prepared from the WWW algorithm.

From the above considerations, our next purpose of the chapter is to perform molecular dynamics (MD) simulations for a-Ge at low to high densities, and show that the structural change of a-Ge takes place upon compression. We again use $O\,(N)$ NTBMD scheme constructed in chapter 3. As our initial atomic configuration, we use the amorphous structure of Ge obtained through a glass-transition simulation performed prior to this calculation. We gradually increase the density of the system, and systematically examine the atomic configuration and dynamical structure of the system at each density.

The rest of the chapter is organized as follows. In section 7.2, we describe the conditions of our calculations, for both the glass-transition simulation and compression of a-Ge. In section 7.3, we give our results for glass transition of Ge, while in section 7.4, we describe the structural change of a-Ge with the increment of density. Finally, we conclude this chapter in section 7.5.

7.2 Conditions of the calculations

In the present chapter, we first perform glass-transition simulation of Ge from temperatures well above melting point. After we obtain an amorphous structure in this manner, we gradually increase the density of the system, and study the structural changes which occur when a-Ge is compressed. In this section, we describe the conditions of these simulations.

For both cases, we perform $O(N)$ NTBMD simulations in the NVT ensemble, with temperature controlled by the Nosé-Hoover thermostat [35]. The conditions of the $O(N)$ NTBMD are the same as those described in chapter 3. Note that, for the glass-transition simulation, we use the $O(N)$ method which exactly conserve the total charge of the system, while for the simulation of low- and high-density amorphous Ge, we use the approximate scheme described in section 3.3.2, which greatly reduces memory requirements. This is because calculations of high-density a-Ge is memory-consuming when the former method is used.

The thermostat parameter is chosen in the same way as in chapter 6. The number N of atoms is chosen as $N = 512$. The equation of motion is integrated by a six-value gear algorithm [7], with a time step of 2.4 ps. The initial velocity for the atoms are drawn from the Maxwell distribution.

7.2.1 glass transition

Firstly, in order to study the glass transition of ℓ-Ge, we start our simulations at $T = 1650$ K, well above the melting temperature (about 1200 K), and decrease the temperature by 200 K at every 4.8 ps. This corresponds to a quench rate of 4.2×10^{13} K $/s$. Physical properties at each temperature are calculated from data accumulated from the last 3.6 ps. We repeat this procedure until the temperature is 50 K.

The density of the system ρ is taken as $\rho = 5.53$ g / cm^3. At this density, the system is in a stable liquid phase. This density is larger than the experimental value (4.79 g / cm^3) for amorphous germanium (a-Ge) under atmospheric pressure [107]. In order to compare our results with experiments concerning a-Ge, a final run is performed with the density set at the experimental value of *a*-Ge by rescaling the simulation cell and the positions of the atoms accordingly, at $T = 300$ K.

7.2.2 low- and high-density amorphous Ge

Now we describe the conditions we adopt to study low- and high-density amorphous Ge. We set the temperature T as 300 K. The density ρ is initially chosen as 4.79 $\mathrm{g/cm^3}$, which is the experimental value of *a*-Ge at atmospheric pressure [107]. After we perform MD simulations of about 6.0-12.0 ps, we compress the whole simulation cell by about 1% in linear dimension. Statistical averages at each density are taken from data obtained through the last 3.6 ps. We perform this procedure until the density is 7.69 $\mathrm{g/cm^3}$. At each density, the static and dynamical structures of the system are calculated.

7.3 Results 1 : glass transition

In this section, we perform quench simulations of Ge from liquid to amorphous phase, using the $O(N)$ NTBMD implemented in chapter 3. Not only does this calculation have interests of its own, but also it serves as a realistic test for our newly implemented calculational scheme.

Calculations of this kind has been performed by *ab initio* MD [44] for $N = 64$ and by classical Stillinger-Webber potential [95] for larger systems [100]. Since the marked feature of an amorphous solid is the presence of short-range order and the absence of long-range order, it is useful to perform MD simulations based on quantum-mechanically-derived forces for systems larger than $N = 64$.

7.3.1 glass transition

When a liquid is rapidly quenched, the diffusion of atoms becomes increasingly difficult, and the system generally transforms from a liquid into glass at a glass transition temperature T_g, where T_g in many cases depends on the quench rate [108]. In order to show that we have simulated a glass transition for Ge, we present here the following quantities:

- pressure of the system, and
- mean-square displacement (MSD), and diffusion coefficients derived from it.

pressure of the system

Firstly, we present in Fig. 7.1 the pressure obtained from our simulations, plotted against temperature. The marked feature of Fig. 7.1 is that an abnormal *increase* in the pressure is observed from $T = 450$ K to $T = 250$ K, reflecting the fact that for Ge, the liquid phase is more dense than the solid phase. This result shows that the system is solid-like at temperatures below $T \sim 450\,\mathrm{K}$.

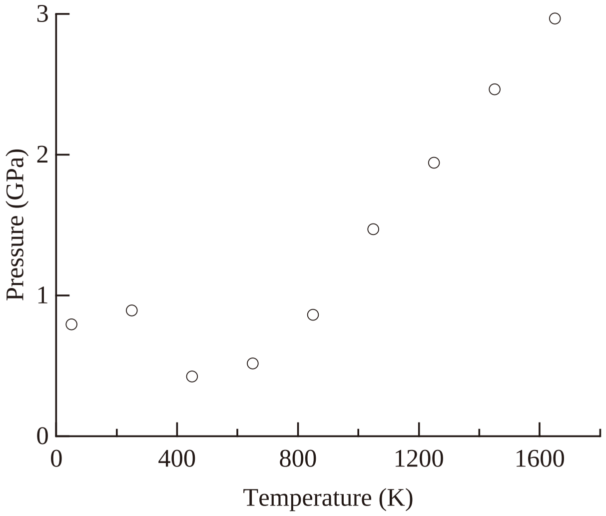

Figure 7.1: Pressure plotted against temperature

mean-square displacement and diffusion coefficients

Next, in Fig. 7.2, we show the mean square displacement (MSD) of the atoms, calculated at different temperatures. We also show in the inset of Fig. 7.2 the diffusion coefficients D. We clearly see from Fig. 7.2 that as temperature decreases, diffusion becomes less significant. In particular, we observe an abrupt decrease in D (by about a factor of five) from $T = 650$ K to $T = 450$ K, which indicates a transition from a diffusive phase (a liquid) to a non-diffusive phase (a solid). As we show in what follows, the solid phase thus achieved turns out to be non-crystalline, or in other words, a glass, and accordingly the cross-over temperature is identified as the glass-transition temperature T_g. We note that the diffusion coefficient obtained at $T = 1250$ K in a liquid phase is $D = 1.2 \times 10^{-4}$ cm^2/s, in excellent agreement with experiments ($D = 1.21{\times}10^{-4}$ cm^2/s) [109] and *ab initio* MD ($D = 1.2{\times}10^{-4}$ cm^2/s) [84].

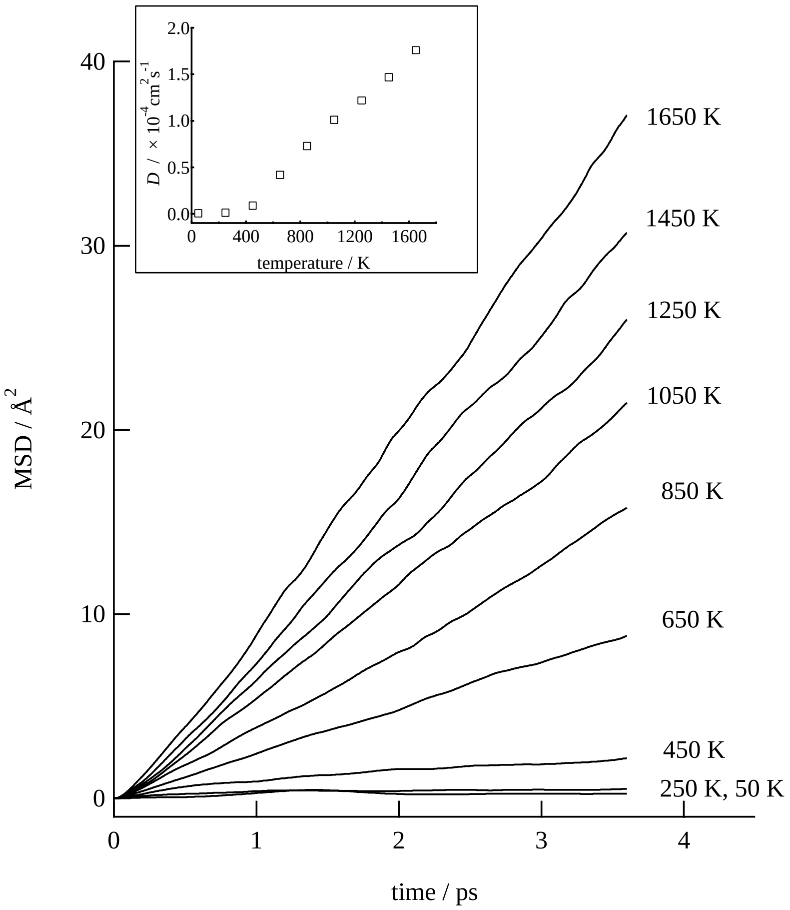

Figure 7.2: The mean-square displacement (MSD) at each temperature, plotted aganist time of the simulations. Inset : The diffusion coefficients calculated from the MSD.

7.3.2 static structure

Now we move on to the investigation of the static structure as the temperature of the system decreases. The following quantities are calculated:

1. *two-body correlation*
    - two-body distribution function, $g(r)$, along with auxiliary quantities such as the coordination number,
    - static structure factor $S(Q)$.
2. *three-body correlation*
    - bond-angle distribution function, $g^{(3)}(r_{\mathrm{c}}, \theta)$.

We also compare our results for a-Ge with available experimental data.

two-body correlation

two-body distribution function In Fig. 7.3, we show the results obtained for the two-body distribution function, $g(r)$.

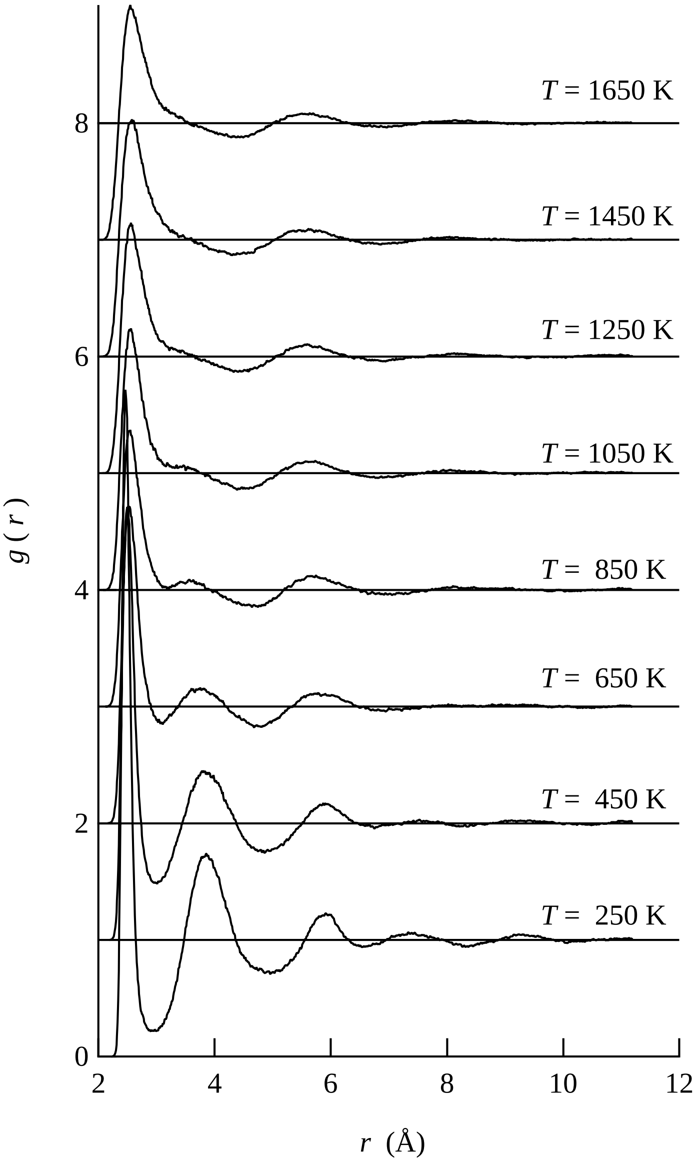

Figure 7.3: The pair-distribution function $g(r)$ calculated at temperatures shown in the figure.

Firstly, we summarize the temperature change of $g(r)$ as follows: as we lower the temperature, (1) the peaks become sharper, (2) the position of the first peak, r_1, shifts to the low-r side, (3) the hump-like peak next to the first peak becomes a distinct peak, and its peak position, r_h, shifts to the high-r side, and (4) a clear trough arises between the first peak and the hump-like (the second) peak, which becomes more distinct as the temperature decreases.

We show in Fig. 7.4 the position of the first peak, r_1, the position of the hump-like peak, r_h, and the ratio of the two positions, r_h/r_1, plotted against temperature. We note that the positions of further peaks do not change. The large change of $g(r)$ between $r = 2.0$ to 6.0 Å implies a very large change in the local atomic structure.

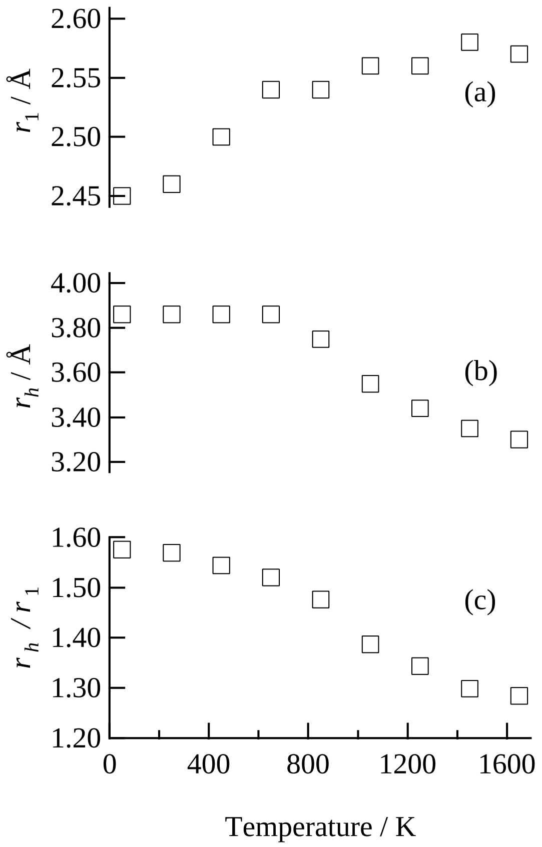

Figure 7.4: The position of the first peak, r_1, the hump-like peak, r_h, and tow ratio of the two positions, r_h/r_1, plotted against temperature.

Among the changes listed above, the most marked one is in the behavior of the hump-like peak next to the first peak. For amorphous solids, this peak is easily interpreted; it simply expresses the correlation between second-neighbor atoms in the diamond structure. This is understood from the presence of a well-defined trough, and the value of r_h/r_1, which is 1.58, close to the diamond value of 1.63 (Fig. 7.4). In the liquid and super-cooled liquid region, the situation is not that easy. The local structure in this region has been interpreted as combination of randomly-packed configuration, hereafter referred to as “isotropic configuration”, and anisotropic, tetrahedral-like bonds originating from covalent bonds, hereafter referred to as simply "covalent bonds" [44, 49, 84]. Note that we use the term "isotropic configuration" for randomly-packed configurations on the basis of the fact that a random packing takes place when the interatomic interactions are *isotropic*. The absence of a trough between the first peak and the hump-like peak in the liquid region implies that sufficient amount of isotropic configurations exist in this region. Further, the covalent bonds are not diamond-like as in the case of amorphous solids, because if this were the case, the ratio r_h/r_1 will have the same value. The value of r_h/r_1 for $T = 1650$ K is about 1.3 (Fig. 7.4), and therefore the covalent bonding in this region is not diamond-like. We speculate that the covalent bonds in the liquid region are actually a combination of several β-Sn-type bonding, with different c/a ratios, as discussed in chapter 6. In this case, the origin of the hump-like peak is interpreted as contribution from the second, third, and fourth neighbor atoms of the β-Sn-type structure.

coordination number We further calculate the coordination number, N_{c}, from the obtained $g(r)$. For the calculation of N_{c}, we need the value of r_{fcs}, the length of the first-coordination shell. The value of r_{fcs} is easily determined for amorphous and super-cooled liquid region, where there is a well-defined first minimum. Ambiguity arises concerning the way to define r_{fcs} in the liquid region, where no clear first minimum appears in our simulations. In the present section, we determine r_{fcs} by extrapolating from the values obtained at lower temperatures. Note that this definition of r_{fcs} is not the same as that adopted in chapter 6. The value of r_{fcs} is not unique in non-crystalline systems; an important point is to stay consistent throughout the discussion.

In Fig. 7.5, we show N_{c} and its distribution, plotted against temperature. We clearly see from this figure that the coordination number is classified into three categories. In the temperature region of $1250 \text{ K} < T < 1650$ K, the system is in the liquid state. The coordination number is about 5.8 at $T = 1650$ K and decreases slightly towards $T = 1250$ K, while the distribution is almost unchanged with decreasing temperature, showing that the structural change in this region is not significant. In the temperature region of $650 \text{ K} < T < 1050$ K, the system is in the super-cooled liquid phase. A rapid decrease of N_{c} is observed between 1250 K

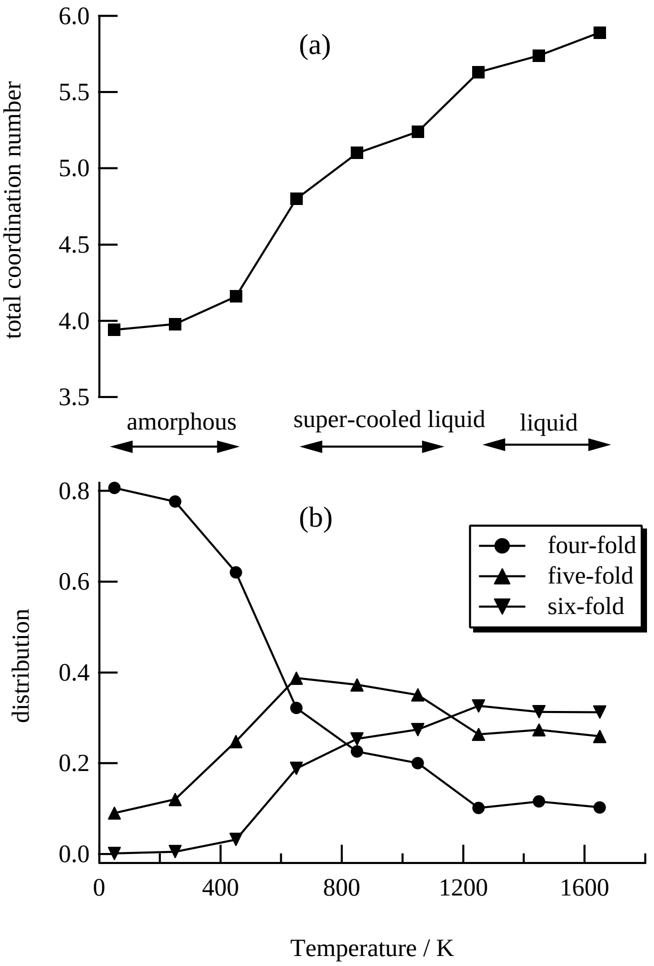

Figure 7.5: The total coordination number N_c (a) and its distribution (b) plotted against temperature.

and 1050 K, and decreases further as temperature decreases. A remarkable point is that the change in the distribution of N_c is quite large in this region, implying a considerable change in the atomic configuration in this temperature region. The number of six-fold atoms decreases, while the number of five-fold and four-fold atoms increases as temperature decreases. This behavior indicates that the atoms start preferring four-fold coordinations typical of covalent bonds while isotropic coordinations become unfavorable. Finally, in the temperature region of 50 K $< T <$ 450 K, the system is in the amorphous solid phase. The coordination number decreases rapidly between 650 K and 450 K, reaching a value close to four. The distribution of N_c shows that the bonding is almost completely four-fold, implying that most of the atoms in the amorphous solid region is covalently-bonded.

static structure factor Now let us discuss the temperature change in $S(Q)$. In Fig. 7.6, we show our results obtained for $S(Q)$. As in the case of $g(r)$, the most remarkable change of

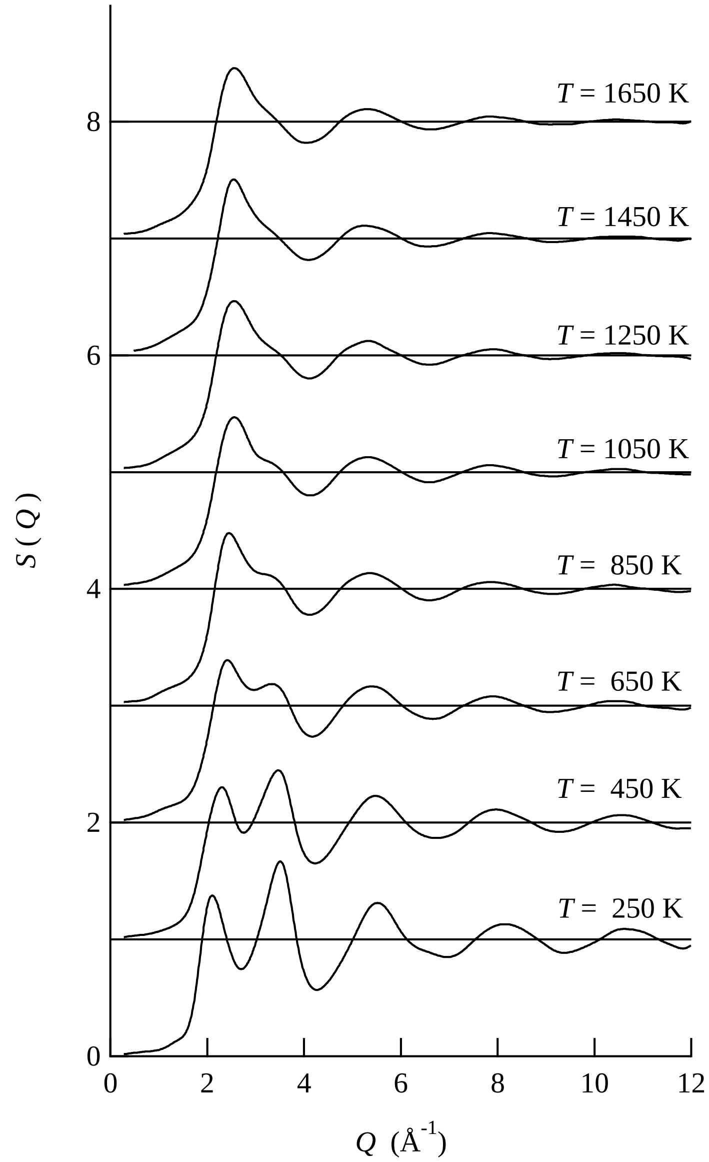

Figure 7.6: The static structure factor $S(Q)$, calculated at the temperautures shown in the figure.

$S(Q)$ is observed at the hump next to the first peak. As the temperature decreases, the hump, which is characteristic of group IV liquids [21], becomes more distinct, and finally becomes a well-defined peak in the amorphous region. As temperature decreases, covalent bonds rapidly increase, and isotropic configurations rapidly decrease, until the system becomes almost totally covalent in the amorphous region. We note that the hump of $S(Q)$ becomes more distinct as this change takes place; however the hump does exist at high temperatures. This result implies that a certain number of covalent bonds are present even in liquids [87].

comparison with experiments Finally, we compare our results with experiments. We use the results obtained from our final simulation, performed at $\rho = 4.79$ g / cm^3 and $T = 300$ K. In Figs. 7.7 (a) and (b), we show experimental $g(r)$ and $S(Q)$ [107] (squares) in comparison with those obtained from our simulations (solid lines). We find that, for both $g(r)$ and $S(Q)$, the agreement is excellent, showing that our simulations give realistic atomic configurations for a-Ge. The very good agreement between experiments and calculations shows the validity of our $O(N)$ NTB model. The coordination number in this case is 3.84, in good agreement with the experimental value of 3.68 [107]. The percentage of four-fold bonding in this case is about 80 %. The remaining atoms are mostly three-fold coordinated (about 16 %),

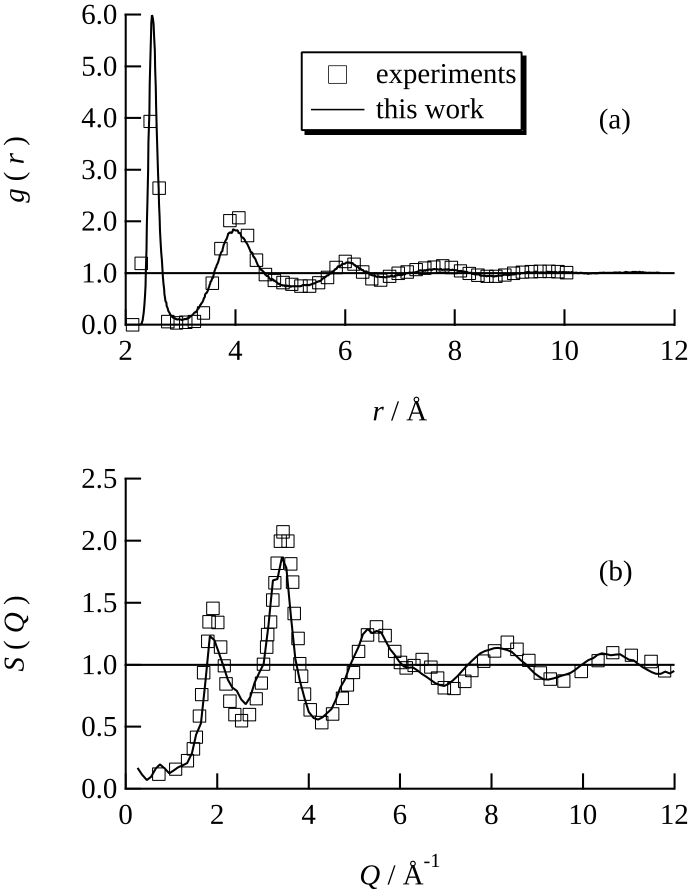

Figure 7.7: Comparison between our simulation and the experimental results of ref. 107; (a) : $g(r)$, (b) : $S(Q)$. The open squares denote experimental results, while the solid lines denote our results.

while atoms with five-fold coordination appears with much less probability (about 3 %). From these results, we deduce that the defects in our amorphous structures are mostly dangling bonds rather than the so-called “floating bonds” [110].

three-body Correlation

bond-angle distribution function Systems with covalent bonding, like Ge, show characteristic behaviors in the three-body correlation. Here, we present the bond-angle distribution function, $g^{(3)}(r_c, \theta)$, which gives the distribution of the angles formed by pairs of vectors drawn towards two neighboring atoms within the cutoff distance r_c from a reference atom. We show in Fig. 7.8 the results obtained for $g^{(3)}(r_c, \theta)$, normalized by $(\sin\theta)^{-1}$, at $r_c = r_1$ and r_{fcs}.

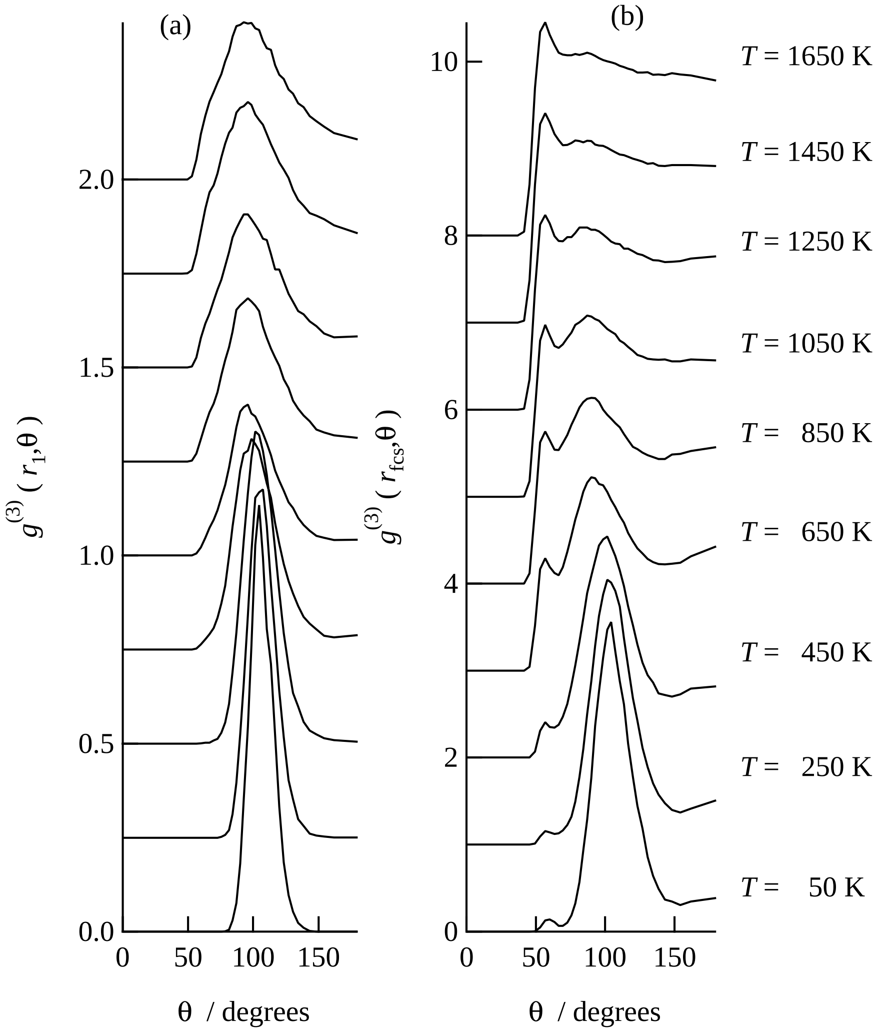

Figure 7.8: The bond-angle distribution function $g^{(3)}(r_c, \theta)$ at different temperatures; (a): $r_c = r_1$, (b): $r_c = r_{fcs}$, where r_{fcs} is the length of the first coordination shell.

In Fig. 7.8 (a), which demonstrates the results for $r_\mathrm{c} = r_1$, we find at $T = 1650$ K a characteristic broad peak at around $90\,^\circ \sim 100\,^\circ$, with a very long tail towards the high-angle side. We also find a slight vestiges of a peak at around $60\,^\circ$. The peak around $90\,^\circ \sim 100\,^\circ$ comes from four-fold bonding while the peak at $60\,^\circ$ is the influence of random packing. Tetrahedral bonding for the diamond structure peaks at $109.5\,^\circ$, and therefore the broad peak is interpreted as contribution from distorted tetrahedral bonding. We note that the distorted tetrahedral structure cannot be interpreted as a single β-Sn-like structure, because if this were the case, another characteristic peak must appear in the high-angle region. Instead, we observe a broad, featureless tail. As discussed in chapter 6, this structure is characterized as a “disordered” β-Sn structure, a structure close to the β-Sn structure but with large fluctuations in the atomic configurations. The broad tail is interpreted as originating from distribution of β-Sn-like structures with different c/a ratios, as implied from chapter 6 and analyses of $g(r)$.

As the temperature decreases, we find that the broad peak becomes narrower, and the high-angle tail becomes less significant. We also find that the peak shifts to higher angles, approaching the value of the diamond structure, $109.5\,^\circ$. At $T = 50$ K, where 80% of atoms have four-fold coordination (Fig. 7.5), the peak is at $106.5\,^\circ$. We clearly find from this behavior that, as temperature decreases, the local structure up to $r = r_1$ changes gradually from a distorted tetrahedral structure to a diamond-like tetrahedral structure.

Figure 7.8 (b) shows the results for $r_\mathrm{c} = r_\mathrm{fcs}$. The most prominent difference from Fig. 7.8 (a) is the increase of the $60\,^\circ$ peak in the liquid and super-cooled liquid region. This behavior shows that, when the search is made in a larger region around each atom, the isotropic nature of atoms at higher temperatures is more clearly observed. As temperature decreases, this contribution clearly decreases, and almost completely disappears at $T = 50$ K, resulting in a bond-angle distribution similar to the one for $r_\mathrm{c} = r_1$. The behavior of $g^{(3)}\,(r_\mathrm{c}, \theta)$ depends greatly on the value of r_c for the liquid and super-cooled liquid. This is because the isotropic coordination and the covalent bonds have different characteristic lengths from each other. In the amorphous solid region, we find no considerable difference. This indicates that in this region, the bonding is almost exclusively covalent, which is consistent with the analyses of $g(r)$.

7.3.3 dynamical structure

In this subsection, the change of dynamical structures with temperature decrease is studied. The quantities taken into account are the following:

- velocity autocorrelation function, $\psi(t)$,
- spectrum density, $\psi(\omega)$.

velocity autocorrelation function

In Fig. 7.9, the VAF is plotted for different temperatures. In the liquid region, we find a single

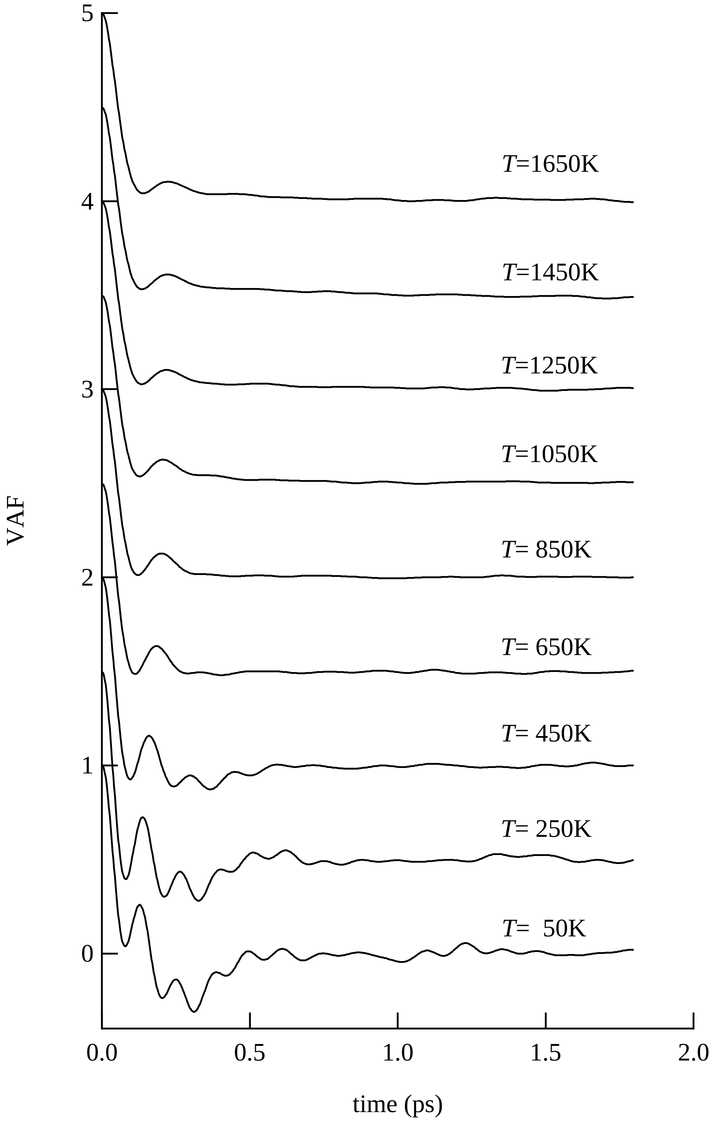

Figure 7.9: The velocity autocorrelation function obtained at each temperature.

peak at $t \sim 0.2\,\mathrm{ps}$. This peak, as discussed in chapter 6, shows that covalent bonds exist in the liquid phase. As the temperature decreases, we find that this peak becomes more significant, and shifts to shorter times. Finally, a drastic change is observed around the glass-transition temperature; a new peak arises around $0.25\,\mathrm{ps}$, and the decay becomes much slower, indicating that in the glass region, the system is more strongly correlated in time than in the liquid and super-cooled liquid regions.

spectrum density

We further study the spectrum density in Fig. 7.10. In the liquid region, we find a shoulder-like peak at $\omega \sim 30\,\mathrm{ps}^{-1}$, reflecting vibrational mode coming from the covalent bonds.

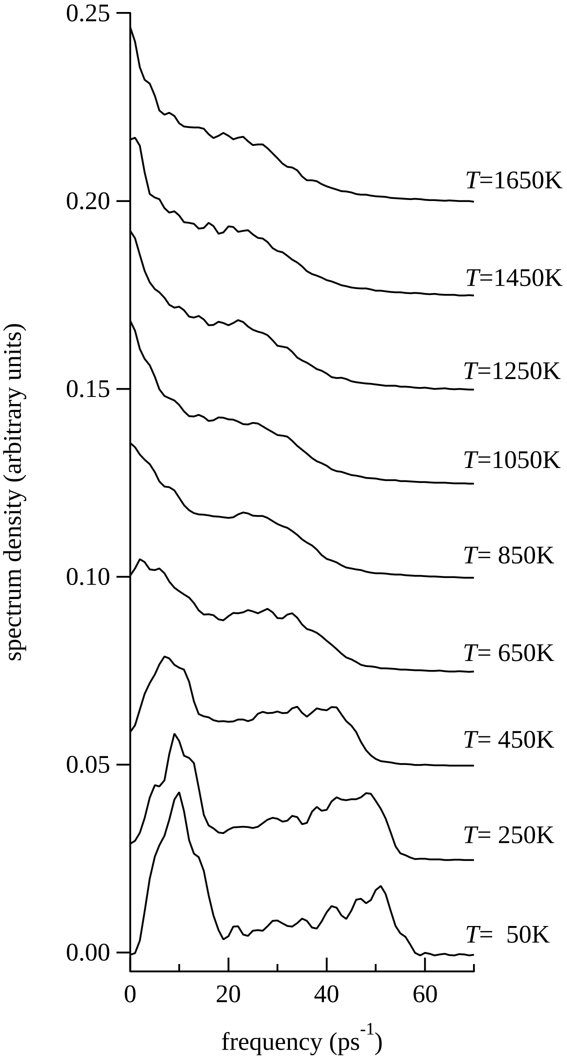

Figure 7.10: Spectrum density obtained at each temperature.

This peak, however, is not a distinct one, and most of the system is diffusive, as discussed in chapter 6. As the temperature decreases, the shoulder-like peak becomes more distinct, accompanied by a hardening of this mode. Again a drastic change is seen after the glass transition; the spectrum density becomes a two-peak structure, with a new peak at $\omega \sim 10\,\mathrm{ps}^{-1}$. In connection with the phonon modes of crystalline Ge, it is possible to assign the low-frequency peak as the TA mode, and the high-frequency peak as the TO mode.

7.3.4 summary of results and discussions

The results obtained in the present section are summarized as follows.

I Static structure,

1. *two-body correlation*
    - from $g(r)$,
        - **(a)** the peaks become sharper with temperature decrease,
        - **(b)** the hump-like peak next to the first peak becomes a distinct peak with temperature decrease,
        - **(c)** coordination number decreases as temperature decreases, and becomes four in the amorphous solid region.
    - from $S(Q)$,
        - **(a)** with temperature decrease, the shoulder on the immediate right-hand side of the first peak becomes a distinct peak.
        - **(b)** with temperature decrease, the height of the first peak becomes lower, while that of the second peak becomes higher, until the height of the two peaks are reversed.
2. *three-body correlation*
    - from $g^{(3)}(r_{\mathrm{c}}, \theta)$,
        - **(a)** for $r_{\mathrm{c}} = r_1$:

  - ▷ high temperature: a peak at $90^\circ \sim 100^\circ$, with a long tail towards the high-angle side.
  - ▷ Shift of the peak to the high-angle side with temperature decrease.
  - ▷ low temperature (amorphous solid): a single peak near the tetrahedral angle

(b) for $r_\mathrm{c} = r_\mathrm{fcs}$:

  - ▷ high temperature (liquid and super-cooled liquid): increase of the isotropic (60°) peak
  - ▷ low temperature (amorphous solid): no essential changes from the case of $r_\mathrm{c} = r_1$.

II Dynamical structure

- from $\psi(t)$,

  (a) single hump-like peak at $t \sim 0.2\,\mathrm{ps}$ for the liquid region,

  (b) drastic change at the glass-transition temperature

- spectrum density, $\psi(\omega)$.

  (a) a weak phonon peak at $\omega \sim 30\,\mathrm{ps}^{-1}$,

  (b) hardening of phonon modes with temperature decrease,

  (c) emergence of a new peak at $\omega \sim 10\,\mathrm{ps}^{-1}$ in the amorphous region.

We observe significant changes in both the static and dynamical structures as the system transforms from a stable liquid to super-cooled liquid, and finally into an amorphous solid. The origin of the structural change is in the increase of covalent bonds within the system as temperature decreases.

This situation is best seen from the behavior of the bond-angle distribution function. For high-temperature liquids, $g^{(3)}(r_\mathrm{c}, \theta)$ shows different distributions for different cutoff distances. This implies the existence of both isotropic bonds and covalent bonds. As the temperature decreases, we observe that the magnitude of the 60° peak for longer r_c gradually decreases, and finally in the amorphous solid region, the $60\,^\circ$ peak almost disappears. The $60\,^\circ$ peak is contribution from isotropic bonds, and therefore, the decrease of its magnitude indicates the increase of the covalent bonds.

Covalent bonds have the lowest internal energy when they form a certain bond angle (in this case, the tetrahedral angle $109.5\,^\circ$). On the other hand, the special angle formed by covalent bonds leads to open structures, which amounts to a large value in the PV term and the entropy term within the free energy of the system. From these considerations, it is possible to interpret the large structural change with decrease of the temperature as follows. System at relatively high temperature tends to have relatively close-pack structures because of atomic diffusion. As temperature decreases, and diffusion of the atoms becomes less significant, the covalent bonds in the system increase in order to receive the merit of the decrease in the internal energy. This behavior of the system accounts for the tetrahedral configuration of a-Ge, and further for the higher pressure in the solid region.

7.4 Results 2 : high-density amorphous structure

In this section, we study the change in the static and dynamical structure of a-Ge with increasing density. Since the low-pressure and high-pressure forms of c-Ge are the diamond structure and the β-Sn structure, respectively, it is expected that the short-range order (SRO) of LDA Ge resembles that of the diamond structure, while the SRO of HDA Ge resembles that of the β-Sn structure. This point is confirmed in the forthcoming arguments.

7.4.1 static structure

Let us first study the change in the static structure with the increment of the density. The following quantities are investigated:

1. *two-body correlation*

   - two-body distribution function, $g(r)$, along with auxiliary quantities such as the coordination number,
   - static structure factor $S(Q)$.

2. *three-body correlation*

   - bond-angle distribution function, $g^{(3)}\left(r_{\mathrm{c}},\theta\right)$.
   - coordination-number dependent bond-angle distribution function.

In order to obtain a visual image of low-density and high-density *a*-Ge, we also study the snapshots of typical atomic configurations for the lowest and highest densities studied.

two-body correlation

two-body distribution function In Fig. 7.11, we show the two-body distribution function $g(r)$, calculated at selected densities. We also show in Figs. 7.12 (a) and (b) the positions of the first and second peak in $g(r)$, to which we refer as r_1 and r_2, plotted against density. From Figs. 7.11 and 7.12, we find considerable structural changes for *a*-Ge as the density ρ is increased.

The most remarkable change for $g(r)$ is observed in the behavior of r_1. In the low-density ($4.79\ \mathrm{g/cm^3} \sim 6.0\ \mathrm{g/cm^3}$) and high-density ($7.0\ \mathrm{g/cm^3} \sim 7.69\ \mathrm{g/cm^3}$) regions, r_1 monotonically decreases as the density increases. On the other hand, at intermediate densities ($6.0\ \mathrm{g/cm^3} \sim 7.0\ \mathrm{g/cm^3}$), r_1 *increases* as the density increases. The increase of r_1 in the intermediate-density region is an unusual behavior in the sense that the first-peak position r_1 increases on the increase of the density as well as that the increase of r_1 is almost discontinuous when the density is about $6.4\ \mathrm{g/cm^3}$. This result implies a large change in the atomic configuration at this density region. The decrease of r_1 in the low-density region or in the high-density region, on the other hand, is a normal behavior, and implies that the contraction of the system is uniform in these density regions. We also note that the position of the second peak, r_2, monotonically decreases as the density increases. Another interesting point is the behavior of the third peak, whose shape changes from symmetric to asymmetric. The asymmetry of the third peak in the high-density region implies that atoms of multiple origins contribute to this peak.

From the behavior of r_1, we obtain the following picture for the structural change of *a*-Ge with density increase. Firstly, in the low-density region, the LDA structure contracts

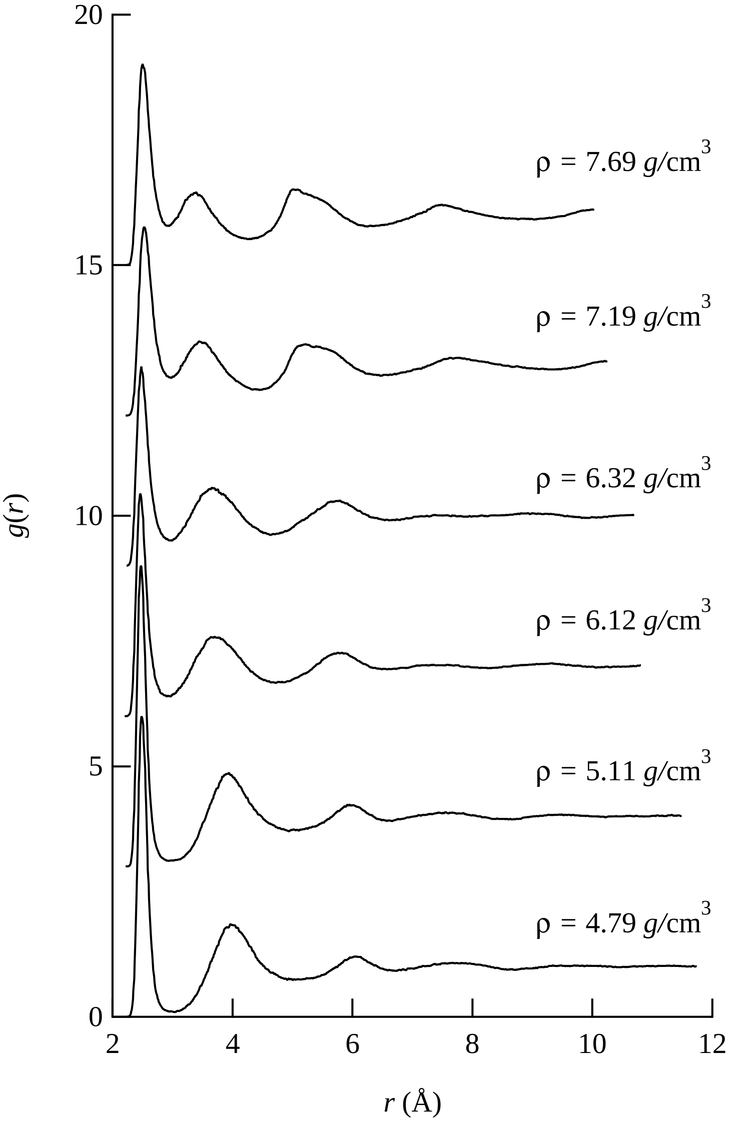

Figure 7.11: Two-body distribution function $g(r)$ calculated at selected densities.

uniformly. Then in the intermediate-density region, the system gradually transforms into the HDA structure, and finally in the high-density region, the HDA structure contracts uniformly. This structural change shows that the LDA and HDA structure obtained in our simulations belong to distinct structures.

coordination number In the next place, let us study the coordination number, N_c. The result is shown in Fig. 7.13 (a). From Fig. 7.13 (a), we find that in the low-density region, N_c is about four, showing that in this region, the bonding in the system is mostly tetrahedral. The coordination number increases as the density increases, and becomes about 6.0−6.5 in

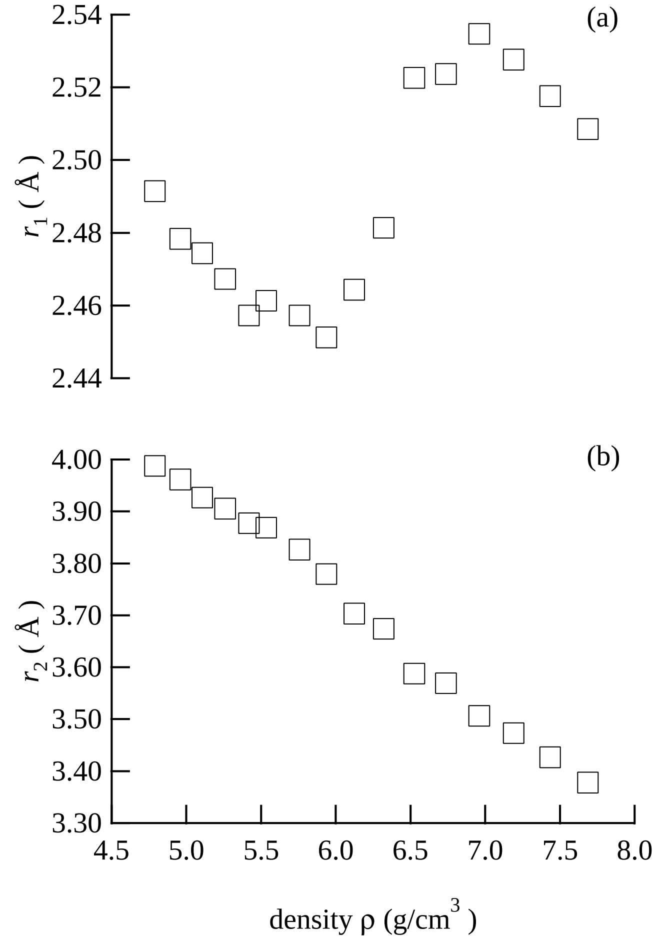

Figure 7.12: Peak positions plotted against density; (a) : for r_1, and (b) : for r_2.

the high-density region.

We further demonstrate the distribution of N_c in Fig. 7.13 (b). From this figure, we clearly observe that, in the low-density region, the system is almost exclusively tetrahedral. In the intermediate-density region, the number of atoms with four-fold coordination decrease, while the numbers of atoms with both five-fold and six-fold coordination increase. Finally, in the high-density region, the numbers of atoms with both four-fold and five-fold coordination decrease, and atoms with six-fold coordination become dominant.

static structure factor We further study the static structure factor, $S(Q)$. Since data obtained for $S(Q)$ are rather scattered, we also smooth our results with cubic spline functions.

In Fig. 7.14 we show our results for $S(Q)$, calculated at the densities as shown in Fig. 7.14. We note that, for the LDA structure, we have already shown in the previous section that our

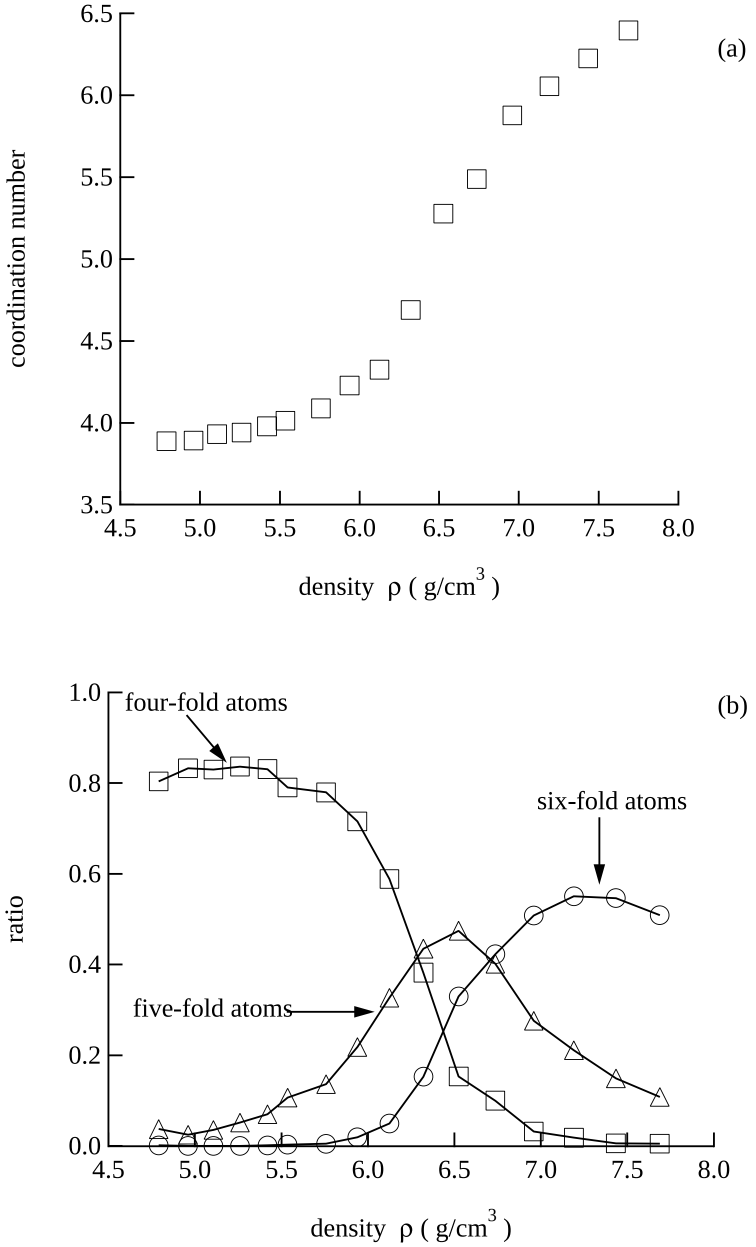

Figure 7.13: The coordination number N_{c} plotted against density, (a) : the average coordination number, and (b) : the distribution of the coordination number. For (b), the squares represent four-fold atoms, the traiangles represent five-fold atoms, and the circles represent six-fold atoms.

results for $S(Q)$ are in remarkably good agreement with experiments. When the density is increased, we find considerable changes both in the first and second peak. At low densities, the first peak is lower than the second peak, but as the density increases, the first peak becomes higher and the second peak becomes lower, until the heights of the two peaks are reversed. We note that the second peak corresponds to the characteristic "shoulder" found in liquid

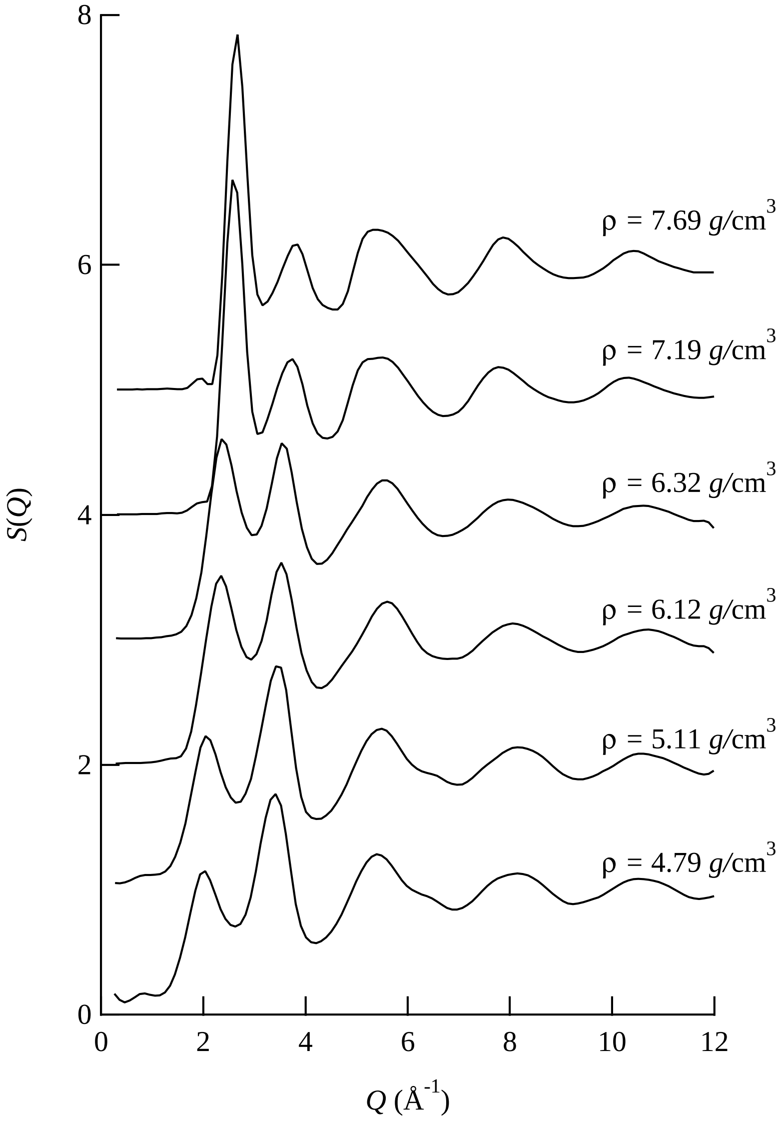

Figure 7.14: Static structure factor $S(Q)$, calculated at selected densities.

Ge (ℓ-Ge) [49, 111]. The changes of $S(Q)$ according to the increase of the density are similar to those found in ℓ-Ge, depicted in chapter 6; that is, in the case of ℓ-Ge, the "shoulder" becomes less distinct, and the first peak becomes higher as the density increases. This fact implies that structural changes of ℓ-Ge and a-Ge are, in a way, similar. One large difference is the presence of diffusion for the case of ℓ-Ge. When diffusion is present, it is difficult for the system to maintain open structures, which makes ℓ-Ge more closely packed than a-Ge. We also note that the "shoulder" for the $S(Q)$ of ℓ-Ge has been interpreted as evidence that tetrahedral-like units exist even in the liquid phase [87]. From this point of view, it is natural that the second peak for a-Ge is more distinct than the shoulder for ℓ-Ge.

three-body correlation

bond-angle distribution function The study of three-body correlation is important for systems which include covalent bonds, such as *a*-Ge, since it allows us to investigate the effects of directional bonding. The bond-angle distribution function $g^{(3)}(r_c, \theta)$ gives the distribution of bond angles, where a bond angle is defined by the angle formed by a pair of vectors drawn from a reference atom to any two other atoms within a cutoff radius r_c of that reference atom. In Figs. 7.15 (a) and (b), we show $g^{(3)}(r_c, \theta)$, normalized by $(\sin\theta)^{-1}$. Figure 7.15 (a) represents $g^{(3)}(r_c, \theta)$ calculated with $r_c = r_1$, while Fig. 7.15 (b) illustrates $g^{(3)}(r_c, \theta)$ calculated with $r_c = r_{\min}$. We note that the bond-angle distribution function is not accessible from experimental studies.

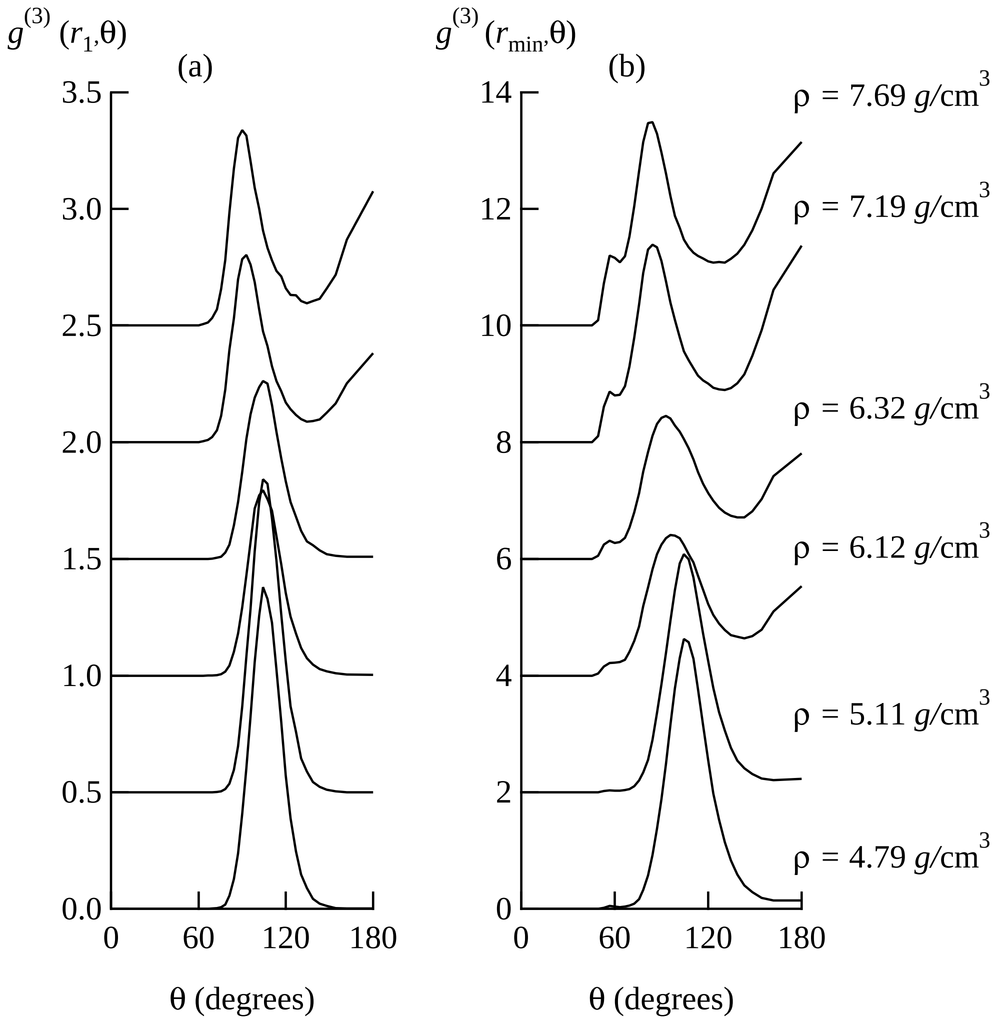

Figure 7.15: The bond-angle distribution function $g^{(3)}(r_c, \theta)$, calculated at selected densities; (a) : for $r_c = r_1$, and (b) : for $r_c = r_{\min}$.

In the low-density region, we find a single peak around the tetrahedral angle, while in the high-density region, we find a peak around $80^\circ \sim 110^\circ$ as well as around $160^\circ \sim 180^\circ$ with a trough around 120°. Note that, in either case, we have a similar distribution for both cutoff distances. This result shows that the system is uniform in low-density and high-density regions.

On the other hand, the behavior of $g^{(3)}\left(r_{\mathrm{c}},\theta\right)$ in the intermediate density region is different for the two cutoff distances, thus implying that, in this density region, the system is not uniform. From Figs. 7.15 (a) and (b), we find that, for the case of $r_{\mathrm{c}} = r_1$, the distribution is similar to that for LDA Ge, while for the case of $r_{\mathrm{c}} = r_{\mathrm{min}}$, the distribution is similar to that for HDA Ge. This result further implies that LDA-like and HDA-like structures coexist in this region. The average nearest-neighbor distance for the LDA structure is shorter than that for the HDA structure. Therefore, the behavior of $g^{(3)}\left(r_1,\theta\right)$ in the intermediate density region of Fig. 7.15 (a) reflects the existence of tetrahedral coordination as found in the LDA structures, while the behavior of $g^{(3)}\left(r_{\mathrm{min}},\theta\right)$ in the same region of Fig. 7.15 (b) confirms the existence of the short-range configuration as found in the HDA structures.

N_{c}-dependent bond-angle distribution function In order to make our point securer, we show in Fig. 7.16 the behavior of $g^{(3)}\left(r_{\mathrm{c}},\theta\right)$ for each coordination number N_{c} in the intermediate-density region, with $r_{\mathrm{c}} = r_{\mathrm{min}}$. From this figure, we observe that the distribution of four-fold coordinated atoms resembles LDA distributions, while the distributions of the five-fold and six-fold coordinated atoms resemble HDA distributions. This result reinforces the above statement of ours that in the intermediate density region, atoms with LDA-like and HDA-like configurations both exist.

snapshots of atomic configurations

In order to give a visual confirmation of the structural change of *a*-Ge with density increase, we show snapshots of atomic configurations in Fig. 7.17. Typical structures in the low-density, intermediate-density, and high-density regions are shown. The unfilled spheres represent atoms with N_{c} less than or equal to four, while the filled spheres represent other, more highly-coordinated atoms. We clearly observe that, for the low-density and high-density regions, the

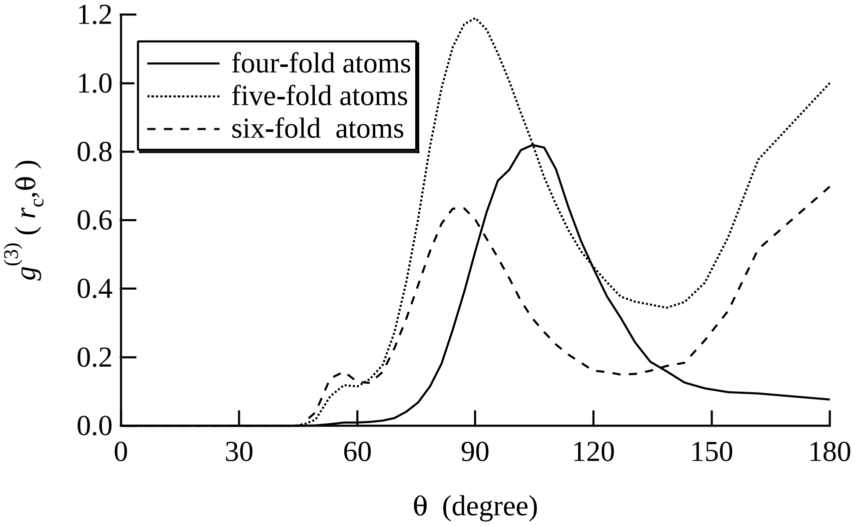

Figure 7.16: Coordination-number dependent bond-angle distribution function, calculated at an intermediate density. Solid curve corresponds to bond-angle distribution for four-fold atoms, dotted curve for five-fold atoms, and dashed line fo six-fold atoms.

atoms have a relatively uniform distribution, while for the intermediate-density region, there are both low-density-like and high-density-like regions.

7.4.2 dynamical structure

Now we look into the changes in the dynamical structure with density increase. For this purpose, the following quantities are explored:

- mean-square displacement, $\left\langle \boldsymbol{R}(t)^2 \right\rangle$,
- velocity autocorrelation function, $\psi(t)$, and
- spectrum density, $\psi(\omega)$.

We also give a comparison between the dynamical structures of high-density a-Ge and high-temperature crystalline β-Sn structure, as done for ℓ-Ge in chapter 6.

mean-square displacement

Let us first show the calculated mean-square displacements in Fig. 7.18. We observe from this figure that there are no diffusive behavior characteristic of liquids, showing that we are in fact studying amorphous solids.

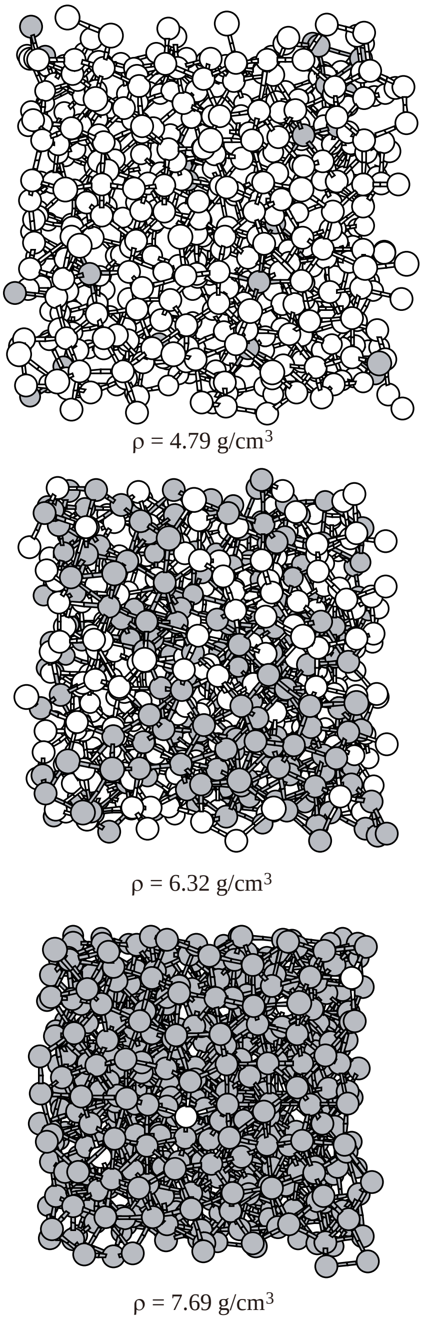

Figure 7.17: Snapshots of typical atomic configurations for a-Ge in the low-density, intermediate-density, and high-density regions. Unfilled spheres represent atoms with N_{c} less than or equal to four, while filled spheres represent other atoms.

velocity autocorrelation function

In Fig. 7.19, we show the results obtained for the velocity autocorrelation function (VAF). Figure 7.19 shows that there exist distinguished differences between $\psi\,(t)$'s for LDA and HDA structures. In particular, we observe that the peak around 0.3 ps for the LDA structures completely disappears for the HDA structures. We also see from Fig. 7.19 that, for the HDA

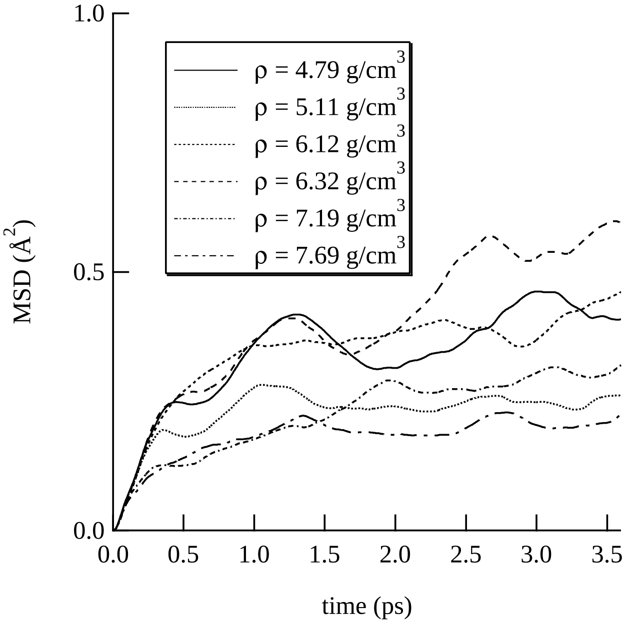

Figure 7.18: Mean-square displacements obtained at selected densities.

structures, the oscillation of the VAF is slower and damps faster. These differences in the VAF show that atoms in the HDA structures move slower and are less correlated in time than those in the LDA structures.

spectrum density

It is informative to study the Fourier transform $\psi(\omega)$ of the VAF, which is often referred to as the spectrum density, since this function is related to the phonon modes in the system. Note that ω represents the frequency of the corresponding phonon mode. In Fig. 7.20 (a), we show $\psi(\omega)$ calculated at the six densities as concerning the other properties. The most marked change observed in $\psi(\omega)$ is in the behavior of the large-scale peak on the high-frequency side. This peak is generally designated as the TO mode from correspondence with crystalline diamond Ge [112]. In Fig. 7.20 (b), we show the top position of this peak, hereafter referred to as ω_{TO}, plotted against the density ρ. At the lowest-density ($\rho = 4.79$ g / cm^3) case, the top of this large-scale peak is placed around $\omega \sim 43$ ps^{-1}. According to the increase of the density in the low-density region, the top-position frequency ω_{TO} moves towards higher frequencies. On a further increase of the density in the intermediate density region, the top-position frequency ω_{TO} is decreased. When the density is increased further in the high-density region, the top-

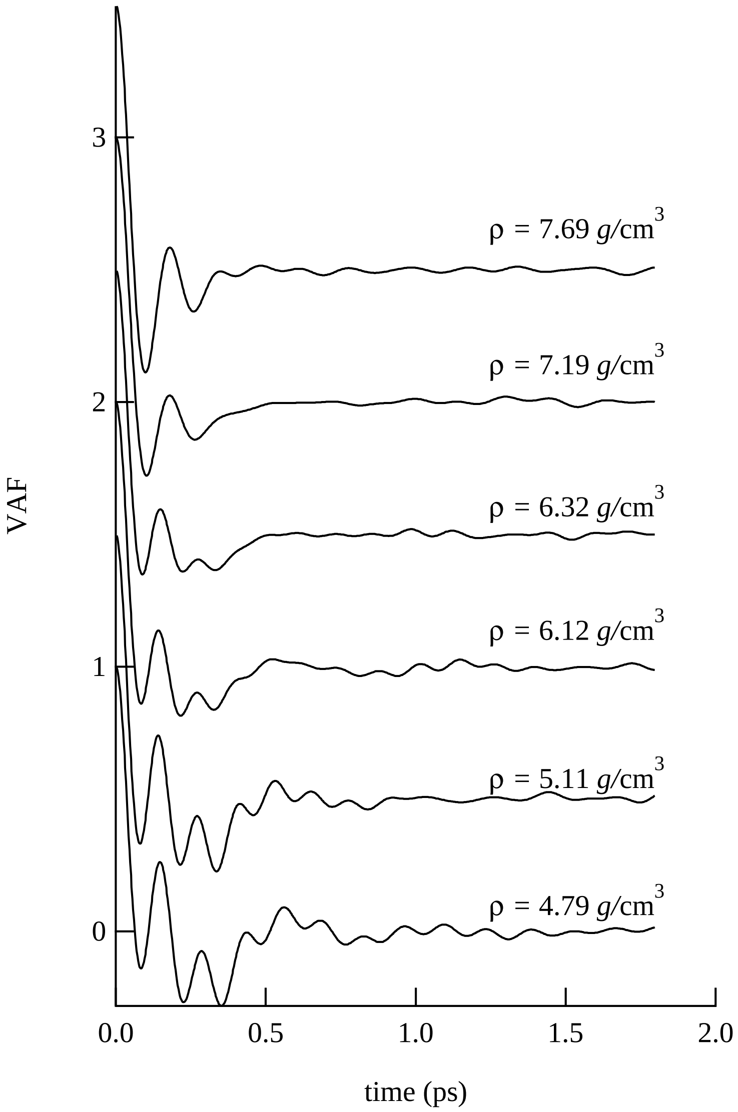

Figure 7.19: The velocity autocorrelation function, calculated at selected densities.

position frequency ω_{TO} is increased again. The increase of ω_{TO} in the low- and high-density region is related to a familiar hardening of the phonon modes accompanying the increase of the density. On the other hand, the decrease of ω_{TO} with the increase of the density indicates the occurrence of a large structural change in the intermediate-density region. In fact, the origin for this softening of the TO mode is explained in connection with the behavior of r_1 as illustrated in Fig. 7.12. Since r_1 increases as density increases at intermediate densities, the interaction between nearest-neighbor atoms weakens, which results in the softening of the TO mode in this density region.

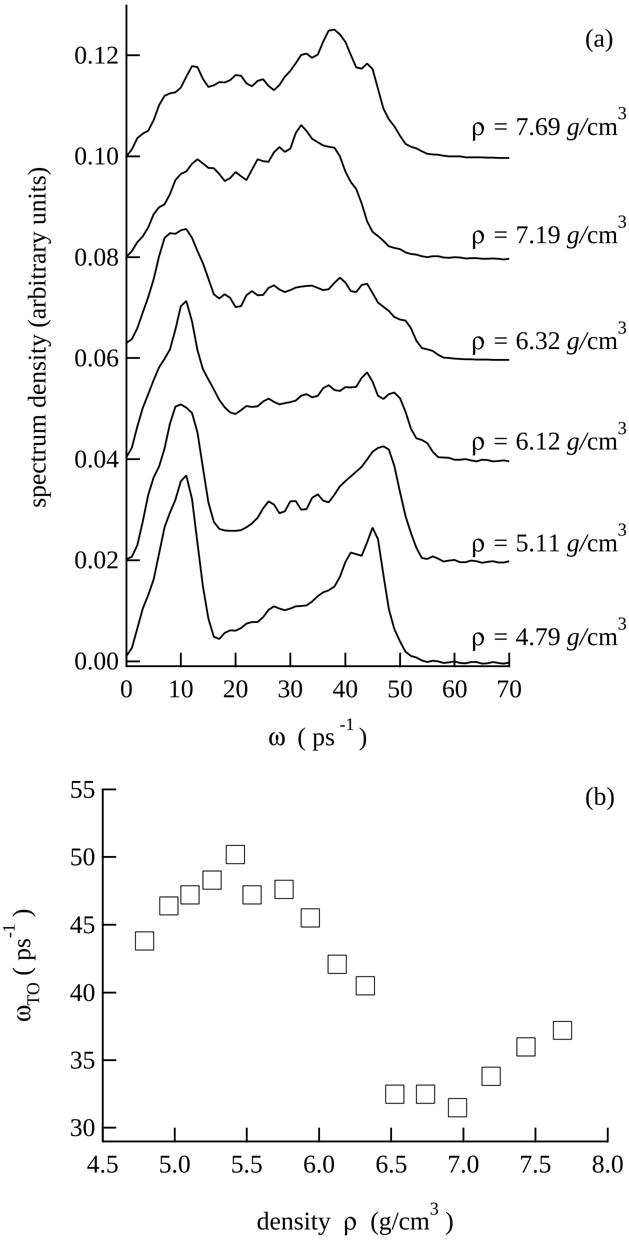

Figure 7.20: Results for the spectrum density, (a) : calculated from the VAF of Fig. 7.19, and (b) : top-position frequency ω_{TO}, plotted against density.

comparison with crystalline β-Sn

The dynamical structure of LDA Ge has previously been studied in connection with that of crystalline Ge [44, 112], but the dynamical structure of HDA Ge has not been studied so far. In order to elucidate the nature of the dynamics in HDA Ge, we compare in Figs. 7.21 (a) and (b) the VAF and the spectrum density for HDA structure and crystalline β-Sn structure simulated at $T = 800\,\mathrm{K}$. Concerning the VAF, the oscillations are quite similar, but the

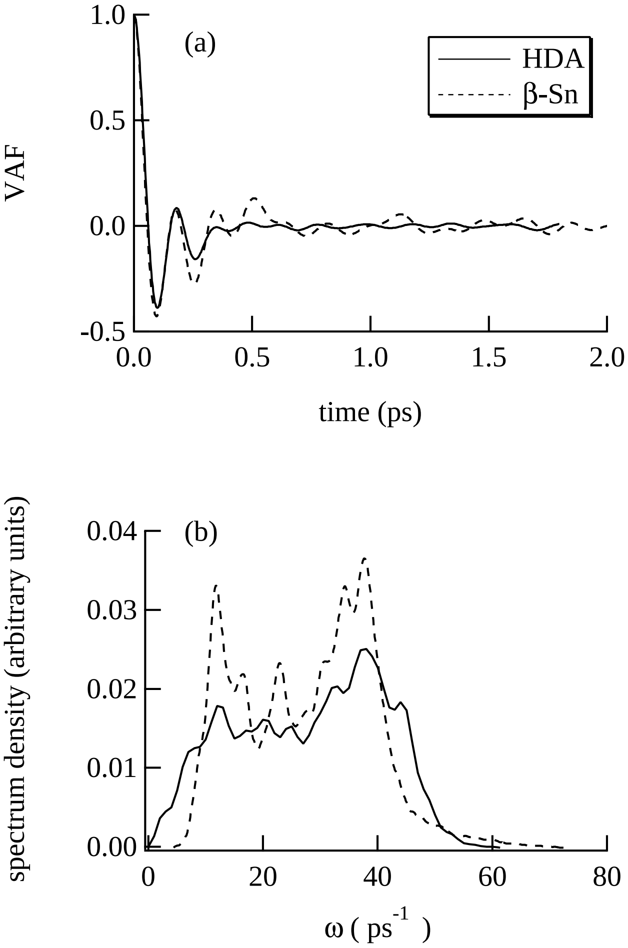

Figure 7.21: Comparison between the HDA structure and crystalline β-Sn structure, (a) : VAF, and (b) : spectrum density. The solid curve corresponds to HDA structure, while the dashed curve corresponds to crystalline β-Sn strucrure.

VAF for HDA structure damps faster than that for crystalline β-Sn structure. Concerning the spectrum density, we find that the phonon peaks appear at the corresponding frequencies, but the distribution over frequencies is broader for HDA structure than that for crystalline β-Sn structure. These results clearly show that the dynamical structure of the atoms for the HDA structure are similar to that of the crystalline β-Sn structure, except that the correlation is weaker for the HDA structure because of disorder in the atomic configurations.

7.4.3 summary of results and discussions

Now let us summarize the results obtained in the present section.

I Static structure,

1. *two-body correlation*
    - from $g(r)$,
        - **(a)** r_1 decreases with the increase of the density at low and high densities, while the opposite behavior is seen at intermediate densities. Note that the values of r_1 at low and high densities are comparable to those of the diamond and β-Sn structures, respectively.
        - **(b)** coordination number changes from four to six. Note that the coordination number for the diamond structure is four, while that for the β-Sn structures is six.
    - from $S(Q)$,
        - **(a)** the changes of $S(Q)$ according to the increase of the density are similar to those found in ℓ-Ge [49]. Note that SRO of ℓ-Ge at high density has been interpreted as combination of structures close to the β-Sn structure and isotropic structure originating from diffusive motion of the atoms.
2. *three-body correlation*
    - from $g^{(3)}(r_\mathrm{c}, \theta)$,
        - **(a)** at low densities, a single peak arises at the tetrahedral angle,
        - **(b)** at high densities, peaks occur at around $80^\circ \sim 110^\circ$ and $160^\circ \sim 180^\circ$, with a trough at around 120°. Note that the peak and trough angles are comparable to those of the β-Sn structure.

II Dynamical structure

- from MSD,
    - **(a)** a non-diffusive behavior is found,
- from $\psi(t)$,
    - **(a)** a peak around 0.3 ps for the LDA structures disappears for the HDA structures,
    - **(b)** for the HDA structure, oscillation of $\psi(t)$ is slower and damps faster.

- spectrum density, $\psi(\omega)$.

  (a) The TO mode hardens with the increase of the density at low and high densities, while the opposite behavior is seen at intermediate densities. Note that for both $\psi(t)$ and $\psi(\omega)$, the dynamical structures of HDA structure resemble those of the crystalline β-Sn structure.

From the inspection of all the results as stated in the preceding section, we come to the conclusion that, at low density, the SRO of atoms in a-Ge is tetrahedral and therefore essentially the same as that of the diamond structure, while at high density the former is close to the SRO of the β-Sn structure. Our results also show that, in the intermediate-density region, a drastic structural change accompanying the increase of the density takes place from the low-density phase to the high-density phase. Note that there exists no long-range order at all in a-Ge for any density. A remarkable point is that all the structural and dynamical properties, which are evaluated in the present simulations, consistently indicate the above-stated conclusion of ours.

Our study here sheds light on the confusion concerning the interpretation of the experimental results by different groups [101–103]. It is also worth noting that our conclusion lends support to the assertion from experiments in ref. 101 that the high-density configurations of a-Ge are expected to be the "distorted β-Sn structure". Let us emphasize, however, that the expression "distorted" used in ref. 101 is somewhat misleading, because it reminds us of "high-temperature crystal" in which the connectivity of bonds is exactly the same as that for a perfect crystal although the atomic positions themselves are thermally disordered.

The high-pressure form of a-Ge has been studied by simulational methods in ref. 105. Most of their results are similar to our results, but there are some substantial differences. To list them,

1. In their work, a clear first-order phase transition was observed, while no signs of first-order phase transition are detected in the present work. The pressure-density curve shows no discontinuities as seen from Fig. 7.22, showing that the structural change observed in our work is not of first order.

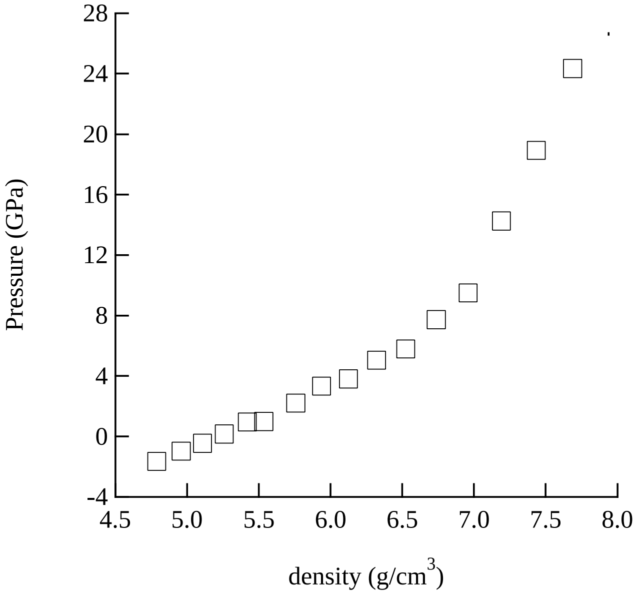

Figure 7.22: Pressure obtained from our simulations, plotted against density.

2. The high-pressure form obtained in their work is close to ours, but the bond-angle distribution function reported has more close-pack-like contributions (peak at 60 °), which implies that the structure obtained in their work is close to that of ℓ-Ge.

One possible explanation for these differences can be given from the difference in the initial atomic configuration. In ref. 105, the initial atomic configuration was constructed from the WWW algorithm, and has no defects in the atomic configuration. Actually, this kind of structure is generally known as a continuous random network (CRN). On the other hand, the initial atomic configuration used in the present study has been prepared from glass-transition simulation, and has defects in the atomic configuration [111]. We note that experimentally, a-Ge has defects; for example, in ref. 107, a coordination number of 3.68 was reported, meaning that sufficient number of dangling bonds exist in a-Ge. The presence of defects in our case makes the system readily transformable by means of compression. This situation results in no clear first-order transition and a different high-density amorphous structure.

7.5 Conclusions for this chapter

In the present chapter, we study the static and dynamical structure of amorphous Ge, using the $O\left(N\right)$ non-orthogonal tight-binding molecular dynamics scheme.

We first investigate the glass transition in Ge. We start from a liquid well above melting point, and quench it to an amorphous solid. Clear signs of glass transition are seen from the behaviors of both the diffusion coefficient and pressure of the system. The static structures of the liquid, super-cooled liquid, and amorphous Ge are extensively analyzed through the pair-distribution function, coordination number, static structure factor, and the bond-angle distribution function, while the dynamical structures are deduced from the VAF and spectrum density. From these analyses, we conclude that the structure of liquid Ge changes in the following manner as it transforms into super-cooled liquid and amorphous solid states: (1) structure originating from isotropic coordination decreases, while structure originating from covalent bonds increases, and (2) the covalent contribution changes from a highly disordered tetrahedral configuration to a diamond-like tetrahedral configuration.

We further study the change of a-Ge as the density is increased. The initial a-Ge is the one obtained in the glass-transition simulation. We gradually increase the density of the system, and analyze the static and dynamical structures for a-Ge at each density. From our analyses, we find that the short-range order of a-Ge transforms from tetrahedral at low density to β-Sn-like at high density. We also find that, at intermediate density, both low-density and high-density amorphous structures coexist. Some of the results are different from previous simulations; the differences are explained in terms of the difference in the initial atomic configurations. Finally, we note that the work performed in this chapter, together with that of chapter 6, is the first report on a comprehensive investigation concerning liquid and amorphous Ge at low to high density by computational methods.

Chapter 8

Concluding remarks

8.1 Summary of our work

The difficulty of any electronic-structure calculation lies in the complexity of the quantum many-body problem. Applicability of true *ab initio* calculations (in the sense that electron-electron interactions are handled exactly), even with the present-day, state-of-the-art computers, is still limited. Naturally, some kind of an approximation must be adopted in order to treat realistic condensed-matter systems.

The tight-binding method is one way to deal with the electronic-structure problem. The strength of the TB method is that calculations are performed efficiently. In particular, it is possible to perform $O(N)$ calculations. Its weakness, on the other hand, lies in that calculations which require detailed quantum-mechanical treatments are not easily dealt with.

In the present thesis, we applied the TB and TBMD methods to the study of photoluminescence properties in Si nanostructures, and also to the study of structural properties for covalently-bonded liquids and amorphous solids at various density. Both of these problems require careful quantum-mechanical considerations. From our studies, we have shown that the TB methods are applicable to these problems. Moreover, we have successfully performed $O(N)$ non-orthogonal TBMD simulations, showing that $O(N)$ TB is applicable to relatively complex TB models. This achievement gives way to $O(N)$ calculations of *ab initio* electronic-structure calculations based on localized basis sets.

Now we summarize the achievements obtained in the present thesis.

We described the basic concepts of the TB and TBMD methods in chapters 2 and 3. In chapter 2, discussions on the basic formulation of the TB method and a brief review of

MD simulations were given. We further described the way to extend TB calculations to MD simulations, and gave formulation at finite electron temperature. Then in chapter 3, we described the order-N TB method. In particular, emphasis was put upon order-N TB for non-orthogonal TB. We have also introduced several new techniques concerning the calculation of the expansion coefficient for the density matrix, which allowed us to increase the speed and the degree of stability for the calculation, and further decrease memory requirements by about a factor of 20. We successfully performed test MD simulations for non-orthogonal TB model of Ge, and showed that the method really works. The results obtained show, for the first time, that order-N non-orthogonal TB is in fact applicable to MD simulations.

In chapter 4 and 5, we investigated the photoluminescence properties of silicon (Si) nanostructures. Silicon nanostructures, unlike bulk Si, are known to show efficient photoluminescence at room temperature. In each of chapters 4 and 5, we introduced new structural models for Si nanostructures, and calculated their electronic states and optical properties. In chapter 4, "Si nanostructures devoid of point-group symmetry" were analyzed by the TB method. Our model differs from previous models in that it has lower symmetry. Our results revealed that the newly-introduced model well accounts for the discrepancy found between theoretical calculations and experiments in the behavior of the radiative recombination time for the so-called 'S'-band luminescence. This result was interpreted as follows: because of the lower symmetry of our new model, some forbidden transitions become allowed, which leads to a change in the behavior of the radiative recombination time. In chapter 5, we introduced another new model. Here, structural relaxation was taken into account for two types of Si nanostructures, namely, "well-passivated Si nanostructures" and "poorly-passivated Si nanostructures". The "poorly-passivated Si nanostructures" were modeled by the following procedures: for some Si nanostructure under consideration, (1) prepare dangling bonds at the surface region, (2) calculate structural relaxation for the nanostructure obtained in (1), (3) re-passivate the nanostructure, and (4) calculate structural relaxation for the nanostructure of (3) to obtain the final atomic configuration to be used in the analyses of the optical properties. The "well-passivated Si nanostructures" gave results which are essentially the same as those found in chapter 4, while the "poorly-passivated Si nanostructures" gave results which well describes the behaviors of the so-called ‘F’-band luminescence. From our work, we have obtained a unified view on the mechanism of ‘S’- and ‘F’-band luminescence by introducing new structural models for Si nanostructures.

We have further studied the static and dynamical structures of liquid (ℓ-) and amorphous (a-) Ge in chapters 6 and 7. In particular, we thoroughly investigated the properties at high density, which are barely known as of now. In chapter 6, we built a NTBMD scheme applicable to the study of ℓ-Ge at low to high density by introducing a new basis and by refitting empirical parameters for existing NTB model of Ge. We carried out TBMD simulations at low to high density, and evaluated the static and dynamical structures at each density. The obtained results were found to be in excellent agreement with available experimental data. From our analyses, we found that the following changes occur with density increase: (1) random configuration typical of liquids increases, and (2) configurations originating from covalent bonds become close to those of the β-Sn structure. In chapter 7, TBMD simulations on a-Ge were performed. We used the order-N, NTBMD scheme constructed in the present work. Firstly, we have done a glass-transition simulation for Ge. We started from a liquid well above melting point, and quenched it to an amorphous solid. The static and dynamical structures of the liquid, super-cooled liquid, and amorphous Ge were extensively studied. We clarified that the large structural change which occurs during the glass transition is addressed to the increase of the covalent bonds. We further increased the density of a-Ge obtained in order to study the structural change of a-Ge with density increase. At each density simulated, we carefully analyzed the static and dynamical structures of a-Ge. Our results show that the local configuration of a-Ge transforms from tetrahedral configuration at low-density to six-fold coordinated, β-Sn-like configuration at high density. We have also found that, at intermediate density, both low-density and high-density amorphous structures coexist. From the present work, a comprehensive knowledge concerning liquid and amorphous Ge at low to high density has been obtained for the first time.

8.2 Work left to be performed

A natural extension for the present work is the development of $O(N)$ methods for *ab initio* electronic-structure calculations. Perhaps this demanding task may be possible by the so-called *ab initio* TB methods [113]. In these methods, the Hamiltonian and overlap matrix elements are calculated from first principles. Application of these methods is still limited, and bottlenecks other than diagonalization of a matrix have prohibited efficient $O(N)$ solutions to these problems. Nonetheless, its establishment is one step towards the ultimate dream of computational condensed-matter physicist: to be able to calculate any property of any given system to the desired accuracy within a computer.

Acknowledgements

The author's most sincere gratitude belongs to Professor F. Yonezawa for her patient supervision and stimulating discussions. Dr. T. Yamaguchi and K. Nishio are acknowledged for their contribution as co-worker of the present work. The author is also grateful to Dr. K. Omata, who showed the author preliminary results for the study of silicon nanostructures. The author acknowledges Professor K. Tsuji, Professor Y. Saito, Professor S. Yabushita, and Professor H. Mori for kindly accepting the role of co-examiner for the present thesis. All the members in the theoretical physics group and the Tsuji laboratory of Keio University are gratefully acknowledged for constant encouragement and fruitful discussions. Finally, the author would like to show his sincere gratitude to his parents, who gave constant support. Financial support has been provided by "Research for the Future Project" on "Physics of Nanocrystalline Semiconductors and Their Application to New Functional Devices" at Ritsumei University (JSPS-RFTF 96I00102), and by the COE program, "Progress in Mathematics motivated by natural and Social Phenomena", at Keio University.

List of publications

publications associated with chapters 4 and 5

1. J. Kōga, K. Nishio, H. Ohtani, T. Yamaguchi, and F. Yonezawa: "Electronic Properties of Low-Dimensional Si Nanostructures. I. Local Electronic Probabilities", Journal of the Physical Society of Japan, **69** pp. 2188-2191 (2000).

2. J. Kōga, K. Nishio, H. Ohtani, F. Yonezawa, and T. Yamaguchi: "Structural relaxation and its effects on photoluminescence properties in Si quantum wires", Journal of Non-Crystalline Solids, **293-295** pp. 630-634 (2001).

3. J. Kōga, K. Nishio, T. Yamaguchi, and F. Yonezawa: "Tight-Binding Electronic State Calculations of Silicon Nanostructures with Local Disorders: Origin of the 'F' Band Luminescence From Porous Silicon", Journal of the Physical Society of Japan, **70** pp. 2478-2484 (2001).

4. J. Kōga, K. Nishio, T. Yamaguchi, and F. Yonezawa: "The Effects of the Point-Group Symmetry in Silicon Nanostructures on Radiative Recombination Time", Journal of the Physical Society of Japan, **70** pp. 3143-3148 (2001).

5. J. Kōga, K. Nishio, F. Yonezawa, and T. Yamaguchi: "Theoretical study on the relation between structural and optical properties in Si nanostructures", Physica E **15** pp. 182-191 (2002).

6. F. Yonezawa, J. Kōga, K. Nishio, and T. Yamaguchi: "Theoretical study on light emission properties of silicon nanostructures", Recent Research Developments in Physics, **3** pp. 237-256 (2002).

publications associated with chapters 3, 6, and 7

1. J. Kōga, H. Okumura, K. Nishio, T. Yamaguchi, and F. Yonezawa: "Simulational analysis of the local structure in liquid germanium under pressure", Physical Review B **66** 064211, pp. 1-10 (2002).

2. J. Kōga, H. Okumura, K. Nishio, T. Yamaguchi, and F. Yonezawa: "Simulational study of liquid germanium under pressure", Journal of Non-Crystalline Solids, **312-314** pp. 95-98 (2002).

3. J. Kōga, K. Nishio, T. Yamaguchi, and F. Yonezawa : "Order-N tight-binding molecular dynamics and its application to the study of glass transition in germanium", Journal of the Physical Society of Japan, **73** pp. 136-144 (2004).

4. J. Kōga, K. Nishio, T. Yamaguchi, and F. Yonezawa: "Tight-binding molecular dynamics study of Amorphous Germanium with the Increase of Density", Journal of the Physical Society of Japan, **73** (2004).

5. J. Kōga, F. Yonezawa, K. Nishio, and T. Yamaguchi: "Computer analysis on the structure of low-density and high-density amorphous germanium", Journal of Non-Crystalline Solids, in print

other publications

1. K. Nishio, J. Kōga, H. Ohtani, T. Yamaguchi, and F. Yonezawa: "Positional dependence of optical absorption in silicon nanostructure", Journal of Non-Crystalline Solids, **293-295** pp. 705-708 (2001).

2. F. Yonezawa, K. Nishio, J. Kōga, and T. Yamaguchi: "Theoretical prediction for realization of spectra-controllable high-efficient photoluminescent devices by means of silicon nanostructures", Journal of Optoelectronics and Advanced Materials, **4** pp. 569-574 (2002).

3. K. Nishio, J. Kōga, T. Yamaguchi, and F. Yonezawa:“Light emission properties of amorphous silicon quantum dots”, Journal of Non-Crystalline Solids, **312-314** pp. 323-326 (2002).

4. K. Nishio, J. Kōga, T. Yamaguchi, and F. Yonezawa:“Theoretical study of light-emission properties of amorphous silicon quantum dots”, Physical Review B **67** 195304, pp. 1-5 (2003).

5. F. Yonezawa, K. Nishio, J. Kōga, and T. Yamaguchi:“Theoretical study of electronic states and visible photoluminescence from silicon nanostructures”, Journal of Electroanalytical Chemistry, **559** 13-18 (2003).

6. Y. Sano, K. Nishio, J. Kōga, T. Yamguchi and F. Yonezawa: “Simulational study of glass transition in argon”, Journal of Non-Crystalline Solids, in print.

7. K. Nishio, J. Kōga, T. Yamaguchi, and F. Yonezawa: “Molecular Dynamics Simulation on Freezing of Lennard-Jones Argon in an Open-ended Cylindrical nanopore” Journal of Non-crystalline Solids, in print.

8. K. Nishio, J. Kōga, T. Yamaguchi, and F. Yonezawa:“Capillary Condensation and Freezing of Lennard-Jones Argon in Open-ended and Finite Length Nanopore”, submitted to Physical Review B on August 22, 2003.

9. K. Nishio, J. Kōga, T. Yamaguchi, and F. Yonezawa; “Confinement-Induced Amorphous solids of Lennard-Jones Argon”, submitted to Journal of the Physical Society of Japan on September 29, 2003.

Bibliography

[1] P. A. M. Dirac, *Proc. Roy. Soc. A* **123**, 714 (1929).

[2] M. C. Payne, M. P. Teter, D. C. Allan, T. A. Arias, J. D. Joannopoulios, *Rev. Mod. Phys.* **64**, 1045 (1992).

[3] E. Wimer, *Mater. Sci. Eng. B* **37**, 72 (1996).

[4] P. Hohenberg, W. Kohn, *Phys. Rev.* **136**, 864B (1964).

[5] W. Kohn, L. J. Sham, *Phys. Rev.* **140**, 1133A (1965).

[6] C. M. Goringe, D. R. Bowler, E. Hernández, *Rep. Prog. Phys.* **60**, 1447 (1997).

[7] M. P. Allen, D. J. Tildesley, *Computer Simulation of Liquids* (Clarendon Press, Oxford, 1987).

[8] R. Car, M. Parrinello, *Phys. Rev. Lett.* **55**, 2471 (1985).

[9] S. Goedecker, L. Colombo, *Phys. Rev. Lett.* **73**, 122 (1994).

[10] S. Goedecker, M. Teter, *Phys. Rev. B* **51**, 9455 (1995).

[11] S. Goedecker, *Rev. Mod. Phys.* **71**, 1085 (1999).

[12] C. Z. Wang, C. T. Chan, K. M. Ho, *Phys. Rev. B* **39**, 8586 (1989).

[13] S. Goedecker, *Phys. Rev. B* **58**, 3501 (1998).

[14] S. Ismail-Beigi, T. A. Arias, *Phys. Rev. Lett.* **82**, 2127 (1999).

[15] W. A. Harrison, *Electronic Structure and Properties of Solids* (Freeman, San Francisco, 1980).

[16] P. C. Slater, G. F. Koster, *Phys. Rev.* **94**, 1498 (1954).

[17] L. T. Canham, *Appl. Phys. Lett.* **57**, 1046 (1990).

[18] H. Takagi, H. Ogawa, Y. Yamazaki, A. Ishizaki, T. Nakagiri, *Appl. Phys. Lett.* **56**, 2379 (1990).

[19] A. G. Cullis, L. T. Canham, P. D. J. Calcott, *J. Appl. Phys.* **82**, 909 (1997).

[20] L. T. Canham, *Phys. Stat. Sol.* **190**, 9 (1995).

[21] Y. Waseda, *The structure of non-crystalline materials* (McGraw-Hill, New York, 1980).

[22] C. Z. Wang, K. M. Ho, *Advances in Chemical Physics* **XCIII**, 651 (1996).

[23] P. Løwdin, *J. Chem. Phys.* **18**, 365 (1950).

[24] J. Kanamori, F. Yonezawa, K. Kawamura, K. Terakura, *Solid State Physics (in Japanese)* (Iwanami, Tokyo, 1997).

[25] P. Y. Yu, M. Cardona, *Fundamentals of Semiconductors* (Springer-Verlag, 1998).

[26] Y. M. Niquet, C. Delerue, G. Allan, M. Lanoo, *Phys. Rev. B* **62**, 5109 (2000).

[27] W. H. Press, S. A. Teukolsky, W. T. Vetterling, B. P. Flannery, *NUMERICAL RECIPES in Fortran 77* (Cambridge University Press, 1992).

[28] C. H. Henry, K. Nassau, *Phys. Rev. B* **1**, 1628 (1970).

[29] A. J. Read, *et al.*, *Phys. Rev. Lett.* **69**, 1232 (1992).

[30] C. Delerue, G. Allan, M. Lanoo, *Phys. Rev. B* **48**, 11024 (1993).

[31] P. K. Basu, *Theory of Optical Processes in Semiconductors, Bulk and Microstructures* (Clarendon Press, Oxford, 1997).

[32] L. C. L. YanVoon, L. R. Ram-Mohan, *Phys. Rev. B* **47**, 15500 (1993).

[33] M. Cruz, M. R. Beltrán, C. Wang, J. T. Martínez, Y. G. Rubo, *Phys. Rev. B.* **59**, 15381 (1999).

[34] H. Goldstein, *Classical Mechanics* (Addison-Wesley, Reading, 1980).

[35] S. Nosé, *Prog. Theor. Phys. Supp.* **103**, 1 (1991).

[36] S. Nosé, *Mol. Phys.* **52**, 255 (1984).

[37] H. C. Andersen, *J. Chem. Phys.* **72**, 2384 (1980).

[38] C. Delerue, M. Lanoo, G. Allan, *Phys. Rev. Lett.* **76**, 3038 (1996).

[39] J. M. Jancu, R. Scholz, F. Beltram, F. Bassani, *Phys. Rev. B* **57**, 6493 (1998).

[40] P. Pulay, *Mol. Phys.* **17**, 197 (1969).

[41] W. M. C. Foulkes, R. Haydock, *Phys. Rev. B* **39**, 12520 (1989).

[42] J. R. Morris, C. Z. Wang, K. M. Ho, *Phys. Rev. B* **52**, 4138 (1995).

[43] T. Oda, Y. Hiwatari, *J. Phys.: Condens. Matter* **12**, 1627 (2000).

[44] G. Kresse, J. Hafner, *Phys. Rev. B* **49**, 14251 (1994).

[45] X. P. Li, R. W. Nunes, D. Vanderbilt, *Phys. Rev. B* **47**, 10891 (1993).

[46] B. W. Roberts, W. Luo, K. A. Johnson, P. Clancy, *Chemical Engineering Journal* **74**, 67 (1999).

[47] K. R. Bates, A. D. Daniels, G. E. Scuseria, *J. Chem. Phys.* **109**, 3308 (1998).

[48] U. Stephan, D. A. Drabold, *Phys. Rev. B* **57**, 6391 (1998).

[49] J. Kōga, H. Okumura, K. Nishio, T. Yamaguchi, F. Yonezawa, *Phys. Rev. B* **66**, 064211 (2002).

[50] T. Frauenheim, *et al.*, *Phys. Rev. B* **52**, 11492 (1995).

[51] J. J. Mortensen, M. Parinello, *J. Phys.: Condens. Matter* **13**, 5731 (2001).

[52] T. Ozaki, *Phys. Rev. B* **64**, 195110 (2001).

[53] A. Gibson, R. Haydock, J. P. LaFemina, *Phys. Rev. B* **47**, 9229 (1992).

[54] D. J. Lockwood, *Light Emission in Silicon: From Physics to Device* (Academic Press, New York, 1998).

[55] R. P. Vasquez, R. W. Fathauer, T. George, A. Ksendzev, T. L. Lin, *Appl. Phys. Lett.* **60**, 2359 (1992).

[56] C. Tsai, *et al.*, *Appl. Phys. Lett.* **59**, 2814 (1991).

[57] M. S. Brandt, H. D. Fuchs, M. Stuzmann, J. Weber, M. Cardona, *Solid State Commun.* **81**, 307 (1992).

[58] Y. Kanemitsu, *et al.*, *Phys. Rev. B.* **48**, 2827 (1993).

[59] P. M. Fauchet, *J. Lummin.* **70**, 294 (1996).

[60] P. D. J. Calcott, K. J. Nash, L. T. Canham, M. J. Kane, D. Brumhead, *J. Phys.: Condens. Matter* **5**, L91 (1993).

[61] T. Suemoto, K. Tanaka, A. Nakajima, *Phys. Rev. B.* **49**, 11005 (1994).

[62] Y. Kanemitsu, S. Okamoto, M. Otobe, S. Oda, *Phys. Rev. B.* **55**, R7375 (1997).

[63] M. Rosenbauer, S. Finkbeiner, E. Bustarret, J. Weber, M. Stutzmann, *Phys. Rev. B.* **51**, 10539 (1995).

[64] S. Y. Ren, J. D. Dow, *Phys. Rev. B.* **45**, 6492 (1992).

[65] B. Delley, E. F. Steigmeier, *Phys. Rev. B.* **47**, 1397 (1993).

[66] J. P. Proot, C. Delerue, G. Allan, *Appl. Phys. Lett.* **61**, 1948 (1992).

[67] G. D. Sanders, Y. C. Chang, *Phys. Rev. B.* **45**, 9202 (1992).

[68] T. Ohno, K. Shiraishi, T. Ogawa, *Phys. Rev. Lett.* **69**, 2400 (1992).

[69] M. S. Hybertsen, M. Needels, *Phys. Rev. B* **48**, 4608 (1993).

[70] S. G. Lee, B. H. Cheong, K. H. Lee, K. J. Chang, *Phys. Rev. B.* **51**, 1762 (1995).

[71] H. Kageshima, *Surf. Sci.* **357-358**, 312 (1996).

[72] A. G. Cullis, L. T. Canham, *Nature* **353**, 335 (1991).

[73] Y. H. Xie, *et al.*, *J. Appl. Phys* **71**, 2403 (1992).

[74] M. S. Hybertsen, *Light Emission from Silicon, MRS Proceedings No. 256* (Material Research Society, Pittsburgh, 1992).

[75] N. Koshida, *et al.*, *Appl. Phys. Lett.* **63**, 2774 (1993).

[76] D. I. Kovalev, I. D. Yaroshetzkii, T. Muschik, V. Petrova-Koch, *Appl. Phys. Lett.* **64**, 214 (1994).

[77] A. M. Saitta, F. Buda, A. G. Fiumara, P. V. Giaquinta, *Phys. Rev. B* **51**, 1446 (1996).

[78] J. P. Hansen, I. R. McDonald, *Theory of simple liquids* (Academic press, London, 1986).

[79] Y. Waseda, K. Suzuki, *Z. Physik B* **20**, 339 (1975).

[80] M. C. Bellissent-Funel, R. Bellissent, *J. Non-Cryst. Solids* **65**, 383 (1984).

[81] V. Petkov, S. Takeda, Y. Waseda, K. Sugiyama, *J. Non-Cryst. Solids* **168**, 97 (1994).

[82] A. Filipponi, A. D. Cicco, *Phys. Rev. B* **51**, 12322 (1995).

[83] W. Yu, Z. Q. Wang, D. Stroud, *Phys. Rev. B* **54**, 13946 (1996).

[84] R. V. Kulkarni, W. G. Aulbur, D. Stroud, *Phys. Rev. B* **55**, 6896 (1997).

[85] N. Takeuchi, I. L. Garzón, *Phys. Rev. B* **50**, 8342 (1994).

[86] V. Petkov, G. Yunchov, *J. Phys.: Condens. Matter* **6**, 10885 (1994).

[87] N. W. Ashcroft, *Nuovo Cim. D* **12**, 597 (1990).

[88] T. Mori. Private communications.

[89] M. Menon, *J. Phys.: Condens. Matter* **10**, 10991 (1998).

[90] J. Kōga, H. Okumura, K. Nishio, T. Yamaguchi, F. Yonezawa, *J. Non-Cryst. Solids* **312-314**, 95 (2002).

[91] M. van Schilfgaarde, W. A. Harrison, *J. Phys. Chem. Solids* **46**, 1093 (1985).

[92] R. Hoffmann, *J. of Chem. Phys.* **39**, 1397 (1963).

[93] P. Vogl, H. P. Hjalmarson, J. D. Dow, *J. Phys. Chem. Solids* **44**, 365 (1983).

[94] M. T. Yin, M. L. Cohen, *Phys. Rev. B* **26**, 5668 (1982).

[95] F. H. Stillinger, T. A. Weber, *Phys. Rev. B* **31**, 5262 (1985).

[96] J. Hafner, G. Kahl, *J. Phys. F: Met. Phys.* **14**, 2259 (1984).

[97] H. Okumura, F. Yonezawa, *J. Chem. Phys.* **113**, 9162 (2000).

[98] H. Okumura, F. Yonezawa, *J. Phys. Soc. Japan* **70**, 1990 (2001).

[99] H. Okumura, F. Yonezawa, *Physica B* **296**, 180 (2001).

[100] K. Ding, H. C. Andersen, *Phys. Rev. B* **34**, 6987 (1986).

[101] S. Minomura, O. Shimomura, K. Asaumi, H. Oyanagi, K. Takemura, *HIGH-PRESSURE MODIFICATIONS OF AMORPHOUS Si, Ge AND SOME III-V COMPOUNDS* (University of Edinburgh, Edinburgh, 1977).

[102] K. Tanaka, *Phys. Rev. B* **43**, 4302 (1991).

[103] J. Freund, R. Ingalls, E. D. Crozier, *J. Phys. Chem.* **94**, 1087 (1990).

[104] J. C. Jamieson, *Science* **139**, 762 (1963).

[105] M. Durandurdu, D. A. Drabold, *Phys. Rev. B* **66**, 041201 (2002).

[106] G. T. Barkema, N. Mousseau, *Phys. Rev. B* **62**, 4985 (2000).

[107] G. Etherington, *et al.*, *J. Non-Cryst. Solids* **48**, 265 (1982).

[108] F. Yonezawa, *Solid State Physics* **45**, 179 (1991).

[109] P. V. Pavlov, E. V. Dobrokhotov, *Sov. Phys. Solid State* **12**, 225 (1970).

[110] S. T. Pantelides, *Phys. Rev. Lett.* **57**, 2979 (1986).

[111] J. Kōga, K. Nishio, T. Yamaguchi, F. Yonezawa, *J. Phys. Soc. Jpn.* **73**, 136 (2004).

[112] N. Maley, J. S. Lannin, D. L. Price, *Phys. Rev. Lett.* **56**, 1720 (1986).

[113] A. P. Horsfield, A. M. Bratkovsky, *J. Phys.: Condens. Matter* **12**, R1 (2000).